FINAL REPORT

to

National Aeronautics and Space Administration
Washington, D.C.

Mechanisms of Monsoon Rainfall in the Indo-Pacific Region

Grant NAGW-3641

1 June 1993-30 November 1995

David W. Martin
Principal Investigator

Barry B. Hinton
Co-Investigator

Kenneth W. Bywaters

Space Science and Engineering Center
at the
University of Wisconsin-Madison

1225 West Dayton Street
Madison, WI 53706

(608) 262-0544

February 1996

SUMMARY

This study presents a new climatology of monsoon rainfall over the Indian and West Pacific Oceans. It uses a generalized version of the Wisconsin scheme to retrieve rain rate from the Pathfinder set of Nimbus-7 Scanning Multichannel Microwave Radiometer (SMMR) brightness temperatures. The scheme yielded monthly rain rate for open-ocean boxes one-degree wide and one-degree high from 1979 through 1986. These rain rates were analyzed for structure, behavior and change. They also were compared with rain rates measured by gauges within India.

Except for gale-force winds, which occurred in a corner of the Arabian Sea through two months of each year, the scheme adequately represented ambient conditions over the Indian and West Pacific Oceans. Two main elements-bands and waves-appeared in the maritime component of monsoon rain. Rain tended to fall in two bands paired across the equator. Across the Indian Ocean, in persistence and strength the southern member consistently dominated the northern member. Across the West Pacific Ocean, the southern member occasionally dominated the northern member. Close to the East Indies northern and southern members merged. Across the embayments of southern Asia a third band paralleled the northern member of the equatorial pair.

Waves followed the sun. Northbound, a wave crossed the equator in the boreal spring; southbound, in the boreal autumn. Following each crossing, it amplified-strongly in the northern hemisphere and weakly in the southern hemisphere. Toward the peak of its excursion into each hemisphere, the wave damped-weakly in the northern hemisphere and strongly in the northern hemisphere.

Waves modulated bands. As a wave approached, a band tended to join it and amplify; as the wave passed, the band tended to follow it and weaken. The interaction of waves and bands yielded zones dominated by an annual cycle, zones dominated by a semi-annual cycle and zones absent either. The annual cycle prevailed along the third band and on the poleward flanks of the members of the equatorial pair of bands. The semi-annual cycle prevailed along the equatorward flanks of members of the equatorial pair.

The records reveal an El Niño/Southern Oscillation (ENSO) event. The event began in 1982, involved both oceans and occurred in two stages, wet and dry. Over the Indian Ocean dry preceded wet; over the West Pacific Ocean, wet preceded dry. In the first stage anomalously light rain fell over the Indian Ocean; anomalously heavy rain over the West Pacific Ocean. In the second stage this dipole pattern reversed sign. Across the West Pacific Ocean the second stage began abruptly. It initiated a second dipole pattern, extreme deficiency in the north member of the equatorial pair of rain bands and little or no deficiency in the south member.

Rain over India conformed to the band-wave model of monsoon ocean rainfall. Dovetailing in phases and amplitudes of Indian Ocean rain and India rain suggests a correspondence between the northbound, amplifying Indian Ocean wave and the onset of the

southwest monsoon. Averaged over a month as well as a year, Arabian Sea and Bay of Bengal rain rate varied with rather than against rain rate over India.

We recommend that the Wisconsin scheme be validated against gauge measurements of rain rate. A validated record would support tests of hypotheses linking Madden-Julian waves to the onset of the southwest monsoon and postulating a biennial cycle in ocean rainfall. It also could be used to investigate the significance of the semi-annual cycle and the band-scale behavior of West Pacific and Indian Ocean rain in the 1982-1984 ENSO. In conjunction with gauge measurements from Asia, Australia, Madagascar, Melanesia and the East Indies it could yield the first comprehensive view of rain in the greater Austral-Asian-Mascarene monsoon system. Spliced to records retrieved from other satellites the Nimbus-7 SMMR record could address issues involving multiple ENSOs and trends in tropical rainfall.

ACKNOWLEDGMENTS

TABLE OF CONTENTS

Mechanisms of Monsoon Rainfall in the Indo-Pacific Region

1. INTRODUCTION

Several years ago NASA funded the Space Science and Engineering Center to study rainfall over the Indian Ocean. SSEC first constructed an algorithm which extracts rainrate from brightness temperatures observed by the Scanning Multichannel Microwave Radiometer (SMMR) on Nimbus-7 and then mapped rainfall over the Indian Ocean. Hinton et al. (1992; hereafter, HOMA) described the algorithm; Martin et al. (1993; hereafter, MHA) described the mapping.

The SSEC SMMR algorithm accepted climatological values for environmental conditions-including surface wind, temperature and humidity-rather than requiring retrieved values. Like that of Prabhakara et al. (1986), the SSEC algorithm employed observations at more than one of SMMR's five frequencies. Unlike any other SMMR algorithm it varied the weight given to each frequency. Rain-variable weighting compensated for the nonlinearity of microwave brightness temperature with increasing rain rate.

Applying this algorithm to three years of SMMR brightness temperatures, in the monsoon rains of the Indian Ocean we found evidence of structure nearly as rich as that of south and southeast Asia. One element of this structure appeared to be related to predictions of Lau and Peng's (1990) theory for 30-60 day oscillations (Madden and Julian 1972; also see Weickmann et al. 1985, Knutson et al. 1986 and Madden 1986); another, to the proposition of Lau and Peng (1990; also see Hartmann and Michelson 1989 and Yasunari 1991) that a Madden-Julian oscillation triggers the onset rains of the southwest monsoon. The implications of the structure underscored the need for a longer record of intra-seasonal rain. A consideration of previous studies (e.g., Meehl 1987 and Lau and Sheu 1988) suggested that the lengthened record should include the western Pacific Ocean.

In 1993 we received funding from NASA for a maritime monsoon rain study. The study aims, first, to map eight years (1979-1986) of monsoon rainfall over the Indian and West Pacific Oceans; second, to test a stationary-band/mobile-wave concept of Indian Ocean rain structure; and, third, to analyze the effect of Madden-Julian oscillations on the onset of monsoon rains. To estimate rainfall it generalizes the SSEC SMMR algorithm.

Here we report on the 1993/1995 monsoon rain project. In turn, the report treats the data base, the rain algorithm, data processing and analysis of rainfall. As preamble to these sections, it summarizes the literature of rainfall over the Indian and West Pacific Oceans.

2. LITERATURE OF RAINFALL OVER THE MONSOON OCEAN

We define *Ocean* as the Indian and Pacific Oceans-including their larger bays and seas-between 30.5°S, 30.5°N, 29.5°E and 159.5°W. Boundaries on the south and east are somewhat arbitrary. Except on the east, land intrudes on every boundary. More seriously, between Asia and Australia islands effectively sever the region. Nevertheless, by most measures (e.g., see Ramage 1971, Meehl 1987 or MHA) Ocean encompasses the maritime part of the Asian-Australian-Mascarene monsoon system and therefore becomes the largest and most important of our analysis regions. Fig. 2.1a shows Ocean. Table 2.1 lists all the "elementary" regions, including those which compose Ocean. Table 2.2 lists all the "composite" regions, including Ocean.

Atlases of rain falling over and near Ocean differ more in detail than in substance. Following HOMA, we draw on the analysis of Jaeger (1976) for a frame of reference. By our interpretation of Jaeger's mapping, using our nomenclature, in the mean over many years rain falls mainly in a circumglobal band which meanders about the equator. From a rain center, or node, over the Congo Basin this *Near-Equatorial Rain Band* (NERB) drops southeastward to the Indian Ocean near the northeast coast of Madagascar (Fig. 2.2). It arches northeastward across the Indian Ocean from Mascarene waters to within a degree or two of the equator near Sumatra. Across Borneo the NERB jumps into the northern hemisphere. It spans the Pacific a few degrees north of the equator and eventually connects again with the Congo node.

Between the Congo and the central Pacific the NERB links three nodes of rain, one weak and two strong. The weak node lies over and northeast of Madagascar. The strong nodes straddle the East Indies, one just west of Sumatra and one just east of Mindanao. We call these the *Mascarene, Indonesian and Philippine Nodes*, respectively.

Across south Asia a second band roughly parallels the NERB. This *South Asian Rain Band* runs east-southeast from the Hindu Kush (in Afghanistan). It crosses northern Pakistan, northern India and southern China. In the far western Pacific Ocean it meets the Asian end of a band which spans the Pacific Ocean in middle latitudes. (The more northerly parts of both bands reflect snow as well as rain.) The South Asian Rain Band harbors a single node, which lies over Bhutan and northeast India.

Three rain ridges extend northward off the NERB. The *Arabian Sea Rain Ridge* runs between the Laccadive Islands and west coast of India. It disappears in the northern reaches of the Arabian Sea. The *Philippine Rain Ridge* runs northward from the Philippine node along and east of the Philippine Islands. It connects with the South Asian Rain Band at the Asia band's Pacific end. The *Bay of Bengal Rain Ridge* runs from the Indonesian node along the eastern flank of the Bay of Bengal and across Bangladesh. It connects with the South Asian Rain Band at the South Asian node. Of the three rain ridges, only the Bay of Bengal ridge holds a node. This *Bay of Bengal Rain Node* lies between the Andaman Islands and Isthmus of Kra.

TABLE 2.1. Elementary regions.

Number	Name	Boundaries	Area[a] boxes	Area[a] km²
1	Arabian Sea	49.5°-79.5°E; 5.5°N-25.5°N	251	3024140
2	Bay of Bengal	79.5°-98.5°E; 5.5°N-22.5°N	114	1378045
3	Philippine Sea	5.5°N-23.5°N, from New Indian Ocean[b] (NIO) east to dateline	1066	12705019
4	Gan	39.5°-100.5°E; 5.5°S-5.5°N	513	6335608
5	Nauru	5.5°S-5.5°N, from NIO east to dateline	432	5334922
6	Madagascar	32.5°-79.5°E; 23.5°S-5.5°S	512	6110602
7	Cocos	79.5°-130.5°E; 23.5°S-5.5°S	615	7323975
8	Coral Sea	5.5°S-23.5°S, from NIO east to dateline	352	4216489
10[c]	Outer Ocean	Ocean minus Inner Ocean[b]	2203	25169350
11	Ocean, except the Old Indian Ocean[b] (OIO)	see Fig. 1b	4014	49645152
12	OIO less Old Arabian Sea, Old Bay of Bengal & Equatorial Strip	see Fig. 1b	1246	15410528
13	Old Arabian Sea	52.5°-75.5°E; 7.5°-24.5°N	209	2584912
14	Old Bay of Bengal	80.5°-96.5°E; 9.5°-20.5°N	6384	5639808
15	Equatorial Strip	39.5°-109.5°E; 5.5°S-4.5°N	43092	38068704

[a]Open ocean only.
[b]See Table 2.2.
[c]There is no region 9.

2-2

TABLE 2.2. Composite regions.

| Composite Region | | Area* | | Elementary Regions |
Number	Name	boxes	km²	
16	Old Indian Ocean (OIO)	2044	25280192	12+13+14+15
17	New Indian Ocean (NIO)	2005	24172370	1+2+4+6+7
18	Arabian Sea/Bay of Bengal	365	4402185	1+2
19	Madagascar/Cocos	1127	13434577	6+7
20	West Pacific Ocean	1850	22256430	3+5+8
21	Inner Ocean	3855	46428800	1+2+3+4+5+6+7+8
22	Ocean	6058	71598150	11+12+13+14+15; equivalently, 1+2+3+4+5+6+7+8+10

*Open ocean only.

The NERB also sends ridges southward. From the Mascarene Node a minor ridge runs south along the eastern shore of Madagascar. From the Philippine node a major ridge runs south- and southeast-ward. The axis of this *South Pacific Rain Band* (SPRB) runs along the north coast of New Guinea and across the Solomon and Santa Cruz Islands. It harbors multiple nodes of rainfall, including the strongest node in Ocean. The SPRB leaves Ocean near the Cook Islands.

Rain minima, or troughs, bound the Near-Equatorial Rain Band. To the south the *South Subtropical Rain Trough* (hereafter, South Trough) splits Australia between the 20th and 30th parallels. As a weak feature it extends east-southeast into the South Pacific. As a strong feature the South Trough extends west from Australia across most of the Indian Ocean.

To the north of the NERB the *North Subtropical Rain Trough* (hereafter, North Trough) connects Arabia, India, Indochina and the Philippine Islands with the subtropical North Pacific. It constitutes a southern boundary for the South Asian Rain Band. The North Trough skirts the north end of the Arabian Sea Rain Ridge. It drops into a dry pocket in southern India east of the Western Ghats. Adapting a term in Spencer (1993), we call this pocket the *West Bay/Andhra Pradesh Rain Shadow*. From the West Bay/Andhra Pradesh Rain Shadow the North Trough jumps northeastward to a second dry pocket, the *East Myanmar Rain Shadow*, on the Pacific side of the Bay of Bengal Rain Ridge. After crossing the Philippine Rain Ridge just north of the Philippine Node, the North Trough extends northeastward and eastward into the North Pacific Ocean.

The North Trough sends a secondary rain trough south and southwest from the Gulf of Oman along the Indian Ocean coasts of Arabia and Africa. Near Cape Delgado (at the north end of the Mozambique Channel) this *West Arabian Sea Rain Trough* crosses the NERB. The North Trough also spawns a loop which drops southward from the dry pocket in India, runs eastward around the foot of the Bay of Bengal, crosses the Bay Rain Ridge between the Indonesian and Bay of Bengal Rain Nodes and reconnects with the North Trough over the South China Sea. Finally, the *Equatorial Pacific Rain Trough* separates the South Pacific rain band from the Pacific part of the NERB.

Drawing in part on Jaeger's analysis, Legates and Willmott (1990) also mapped rainfall over the monsoon-ocean region. Their map of average annual rainfall differs from Jaeger's mainly in its northern-hemisphere features, which tend to be stronger than those of Jaeger. Dorman's (1982) map (for the Indian Ocean only) weights the South Trough at the expense of the Near-Equatorial Rain Band. It shows no rain node near Madagascar, but does indicate a ridge impinging on the West Arabian Sea Rain Trough just north of the equator.

As records for certain spaceborne instruments lengthened beyond a biennium, scientists began to publish rain climatologies based on satellite rather than gauge or surface marine observations. The first (Rao et al. 1976) contains analogs to each of the features found in Jaeger's average annual map. It differs from Jaeger in building rain nodes distant from the NERB along the Philippine and Arabian Sea Rain Ridges and in sharpening the NERB across the North Pacific.

More recent mappings (Chang et al. 1993; Spencer 1993) also boost the NERB across the North Pacific. One (Chang et al. 1993) tends to fuse secondary and primary features. The other (Spencer 1993) weakens the NERB across the East Indies and strengthens the NERB both eastward from the East Indies into the central Pacific and westward from the East Indies into the central Indian Ocean. Spencer's mapping pushes the NERB away from the equator in the eastern and central Indian Ocean, draws it closer to the equator in the western Indian Ocean and squashes the Mascarene Node. The Arabian Sea ridge acquires a rain node, which enhances the dry pocket in south India.

MHA found that rain over the Indian Ocean defined bands. In addition to a dominant trans-oceanic, south-equatorial band (from Sumatra to Madagascar), they identified a Bay of Bengal/Arabian Sea ("India") band, a trans-oceanic north-equatorial band and two quasi-meridional bands. The south-equatorial band corresponds with the NERB in Jaeger's 1976 map; the quasi-meridional bands, with the Arabian Sea and Bay of Bengal Rain Ridges. Neither the trans-oceanic north-equatorial band nor the India band matches features in Jaeger.

Differences between satellite maps of annual rainfall result from differences in orbits, instruments and periods; also, differences in algorithms and map resolutions. Using radiances measured at 19.35 GHz by the Electrically Scanning Microwave Radiometer on Nimbus-5, Rao et al. (1976) mapped annual rain rates at $5° \cdot 5°$ resolution for two years, 1973 and 1974. Using vertically-polarized 19.35 and 22.235 GHz radiances measured by the Special Sensor Microwave Imager (SSM/I) on spacecraft F8 of the Defense Meteorological Satellite Program, Chang et al. (1993) mapped annual average rain rate for the 4 1/2 years beginning in July 1987. Spencer (1993) drew on radiances measured at 50.3, 53.74 and 54.96 GHz by Microwave Sounding Units (MSUs) on the last of the Television and Infrared Observation Satellites (TIROSs) and the first six of the National Oceanic and Atmospheric Agency (NOAA) satellites. He mapped annual average rain rate on a $2.5° \cdot 2.5°$ grid for the 13 years beginning in 1979. Finally, focusing on the Indian Ocean, MHA mapped average annual rainfall from SMMR observations for the three years beginning in 1979 at roughly $1° \cdot 1°$ resolution.
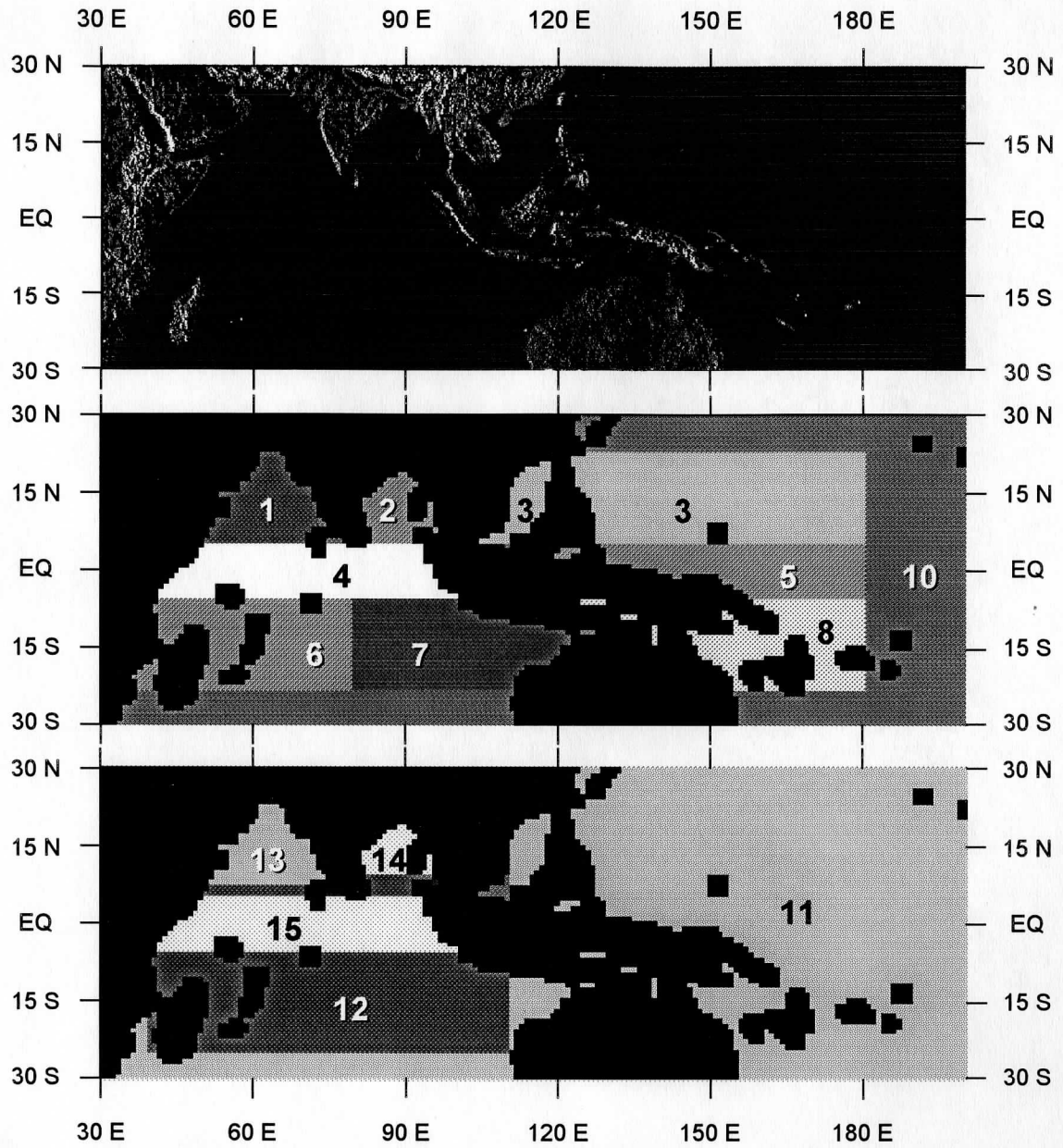
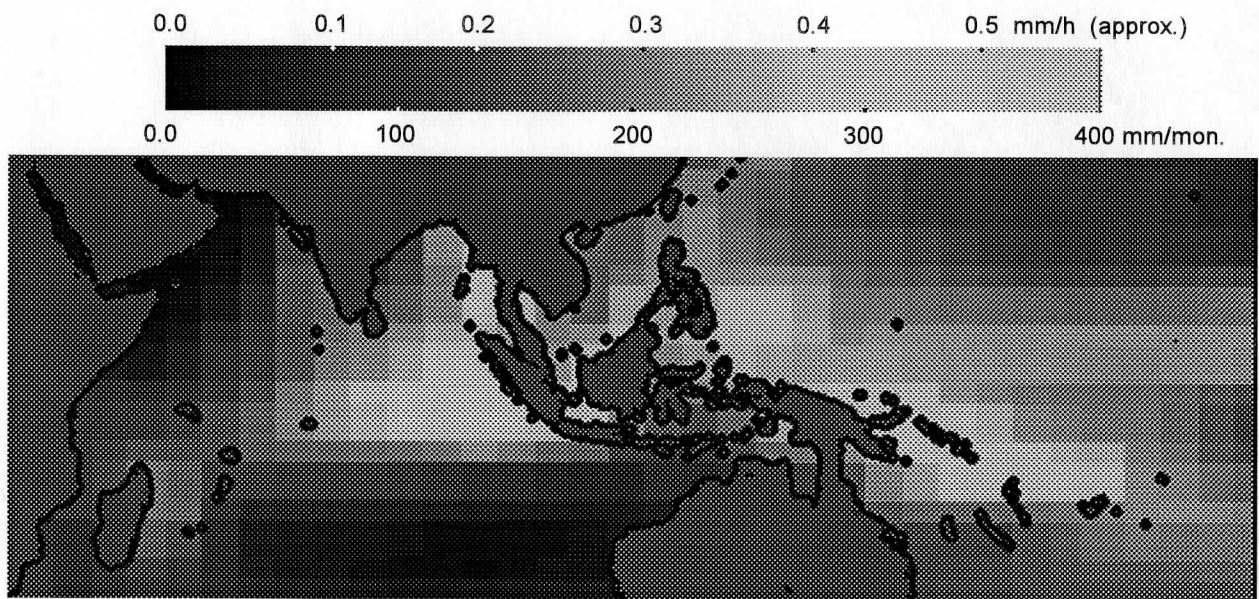Fig. 2.1. The study domain and regions described in Tables 2.1 and 2.2 .

Fig. 2.2. Annual mean rain according to Jaeger.

Fig. 2.3. Indian Ocean and West Pacific with rain features discussed in text.
See Table 2.3 for feature identification.

TABLE 2.3. Ridge, trough, node, and shadow names

A —⑧— A	South Asia Rain Band
B —❶—❷— B	North Subtropical Rain Trough
C —①—②—③— C	Near Equatorial Rain Band
③—④—⑤—⑥— D	South Pacific Rain Ridge
E — E	Equatorial Pacific Rain Trough
F — F	South Subtropical Rain Trough
G — G	West Arabian Sea Trough
H — H	Arabian Sea Ridge
J — J	Bay of Bengal Ridge
K —③	Philippine Ridge

Rain Nodes	Rain Shadows
① Mascarene	❶ West Bay/Andhra Pradesh
② Indonesian	❷ East Myanmar
③ Philippine	
④ New Guinean	
⑤ Solomon	
⑥ Santa Cruz	
⑦ Bay of Bengal	
⑧ South Asian	

3. DATA

3.1 The JPL Pathfinder Set of SMMR Brightness Temperatures

On 24 October 1978 NASA launched Nimbus-7 into a near-polar, sun-synchronous orbit 955 km above the surface of the earth.[1] Southbound, Nimbus-7 crossed the equator near local midnight; northbound, it crossed the equator near local noon. NASA acquired swath observations from SMMR from 25 October 1978 through 20 August 1987. To conserve spacecraft power it operated the instrument on a 50% duty cycle, one day off and one day on.

SMMR measured vertically- and horizontally-polarized radiation at each of five frequencies (6.6, 10.7, 19, 21 and 37 GHz). Its radiometers received energy through a single antenna. Oscillation of an offset reflector enabled this antenna to scan the earth across the suborbital track at a beam-to-surface incidence angle of about 50°. The radiometric footprints (for a 3-dB beamwidth) varied from 148 km by 95 km at 6.6 GHz to 27 km by 18 km at 37 GHz. With scan, at altitude they defined a swath 780 km wide.

The instrument sampled the radiation stream at three rates, which could vary only from frequency to frequency. At the end of each half of a scan cycle it switched from one polarization to the other. Either of these two modes would have insured that the centers of footprints did not necessarily coincide.

As a Pathfinder project, NASA's Jet Propulsion Laboratory recently reprocessed the entire record of SMMR observations. In part JPL undertook the reprocessing to "remove (or reduce) known calibration anomalies that existed in earlier versions of the data..." (Njoku et al. 1995). As part of this reprocessing, it reworked the data into swath format.[2] JPL organized the remapped, recalibrated data by orbit. Using the UNIX tar utility it wrote the data to 8 mm magnetic tapes in compressed Heirarchical Data Format (HDF). Each tape contains four files. The first file gives general information about the tape. The remaining files contain one month of data each with up to 14 SMMR orbits per day. Except for April, May and June of 1986, the JPL record contains more than 95% of possible (i.e., scheduled) data. It contains no data for these three months.

Ordinarily, copies of the SMMR Pathfinder data set would be acquired from the Distributed Active Archive Center of NASA's Marshall Space Flight Center (Njoku et al., 1995)[3]. Through JPL, from January into August 1995 SSEC acquired one of the first copies of the Pathfinder SMMR data set. All analyses of rainfall presented here originate in that data set.

---

[1] For a description of SMMR see Gloersen and Hardis 1978, Njoku et al. 1980; for descriptions of SMMR and its operation on Nimbus-7 see Gloersen et al. 1992, Njoku and Rague 1995.

[2] Channel by channel, JPL interpolated brightness temperature to the location of the footprint of a reference channel. For the reference channel JPL chose 37 GHz (vertical polarization).

[3] Accessible via World Wide Web at the following address: http://wwwdaac.msfc.gov/ims/datasets/smmrtb.html

3.2 Subdivision Rainfall of India

For the period of the SMMR record, we also acquired India Meteorological Department gauge estimates of rain falling each month over each of the 35 meteorological subdivisions of India. After excluding both hilly subdivisions (numbers 2, 12, 15 and 16; Parthasarathy et al. 1992) and island subdivisions (numbers 1 and 35) and reordering the remaining data, we held a table containing 29 columns (one for each subdivision) and 96 rows (one for each month of eight consecutive years).

Monthly subdivision rainfall was converted to monthly India rain rate in four steps. First, to get a table of monthly subdivision rain rate, column by column we multiplied each value of monthly rainfall by either 1/28, 1/29, 1/30 or 1/31. Second, from Parthasarathy et al. (1992; pp. 176-177) we estimated the area of each of the 29 sub-Himalayan, continental-India subdivisions. Third, using these areas monthly rain rate for each subdivision was converted to an area-weighted monthly rain rate. Finally, month by month area-weighted rain rates were summed over all sub-divisions. Hereafter, this is the India series.

Averaged over the series, India rain came to 1053 mm a^{-1}. For the same area of India, but a longer period (1871-1984) and somewhat different set of rain gauges, Mooley and Shukla (1986, Table 2.1) imply a rain rate of 1090 mm a^{-1}. Fig. 3.1 shows monthly rain rate. An annual cycle dominates the series. Rain peaked in July or August; it bottomed out in December, January, February or March. We conclude that the series adequately represents rainfall over sub-Himalayan, continental India.

4. RAIN RETRIEVAL ALGORITHM

At wavelengths (λ) the order of 1 to 10 cm, liquid water bodies having dimensions much larger than λ are "lossy" dielectrics of high refractive index ($n \geq 10$). The emissivity (ε) for thermal radiation at these wavelengths is ~ 0.5. Consequently, even for water temperatures (T_A) of 300 K, a lake or sea has cold brightness temperatures $T_B(\lambda, T_A) = \varepsilon \cdot T_A \approx 0.5 \cdot 300 \text{ K} = 150 \text{ K}$. Emissivity varies with angle and polarization in accordance with Fresnel's formulas, which are a consequence of Maxwell's equations solved for appropriate boundary conditions. Rain drops and cloud droplets having dimensions $\sim\lambda$ or smaller behave quite differently (Ulaby et al., 1986). If ℓ is the drop diameter, then for $\ell \leq \lambda$, liquid water drops emit more strongly than a lake or sea. In fact, raindrops emit more strongly than cloud droplets. Because of their small size and large number in volumes $\approx\lambda^3$, air containing cloud droplets behaves more like a homogeneous medium. This means that raining clouds preferentially appear warm over a cold ocean background in brightness temperature images obtained from a down-looking microwave radiometer.

For ice particles, as for raindrops, the index of refraction is still large (~ 3), but the losses and emissivity are much less. This results in considerable scattering in relation to emission when the particles have sizes the order of λ. Ice particles invariably comprise part of the hydrometeor population within cumulonimbus clouds. Thus intensely raining clouds may appear colder radiatively than the ocean background for smaller values of λ.

Additional processes affecting radiation must be considered to formulate a practical rain retrieval algorithm. Among these are variable emissivity (ε) of the ocean due to changes in the thermometric temperature of the water. Wind-driven waves change the effective value of ε, although this is actually a change in the surface roughness. Emission by the dry air, emission by water vapor; and uncertainty in the structures of real clouds (which will generally contain mixtures of liquid and ice particles having unknown and spatially variable distributions of sizes) must be considered. Finally, the spatial resolution or field of view of the radiometer requires special consideration. Typically, the field of view is the same order, or larger than a raining cloud; often it is appreciably larger than a convective cell. In any case account must be taken of the heterogeneous contents of a field of view.

Algorithms exist for determining surface wind speed, sea surface temperature, and atmospheric water vapor from microwave measurements, but these determinations of the environment using the microwave radiometric data are generally not possible in rainy, or almost-rainy conditions. For the most part a knowledge of the expected environment from climatology is sufficient for microwave rain retrievals. We use a simplified forward radiative transfer model in which key environmental parameters are allowed to vary over modest ranges consistent with climatology in the tropical zone. We then construct from this an inverse model which is completely determined when the environment is specified. The forward model used was developed by Olson (1987) and was also the basis of our previous algorithm (HOMA).

4.1 Theory

Rain rate (R_i) implied by an individual SMMR channel (i), is a function of the channel's brightness temperature (T_{Bi}). It also depends on sea surface temperature (*SST*), relative humidity (*RH*), wind speed (*W*) and freezing level (Z_{fr}). Air temperature at the surface (which is relatively unimportant) is set equal to *SST* and decreases upward at a climatological lapse rate.

A fraction, f_R, of the area of each field of view of SMMR is covered by rain, the balance is not. For a model of the rain no-rain partition we have used results of Graves (1993) fitted to curves of the form $f_R = [a - b \cdot exp(-R/c)]$. The partial ambiguity between precipitating liquid water and non-precipitating liquid water (q_{cloud}) in microwave observations necessitates an explicit model of the relation between precipitating and non-precipitating liquid. This was taken unchanged from our previous work (HOMA). However, now assume that scenes at very low rain rates contain not only precipitating and non-precipitating cloud, but a non-cloudy fraction, f_{clear}, as well (Grassotti and Garand, 1994). Fig. 4.1 illustrates our synthesis of Graves' data (for two pixel sizes) with the Grassotti and Garand results also to $f_{clear} = [A - B \cdot exp(-R/C)]$.
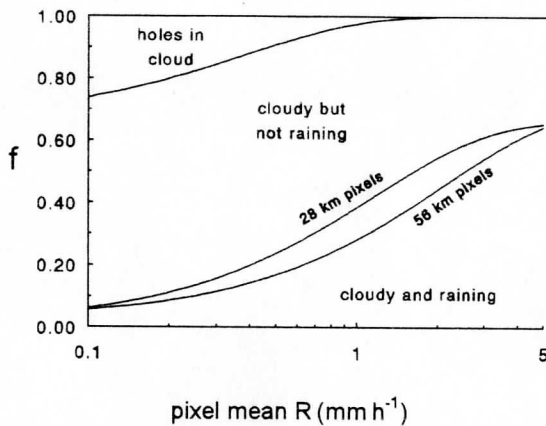

Fig. 4.1. Relation of f_{clear}, f_{cloud} and f_R, at various pixel mean rain rates. Note that the curves are "stacked" to clearly show that they add to unity, i.e.,

$$f_{clear} + f_{cloud} + f_R = 1.$$

Thus, for example, the fraction cloudy but not raining in a 28 km pixel which has a mean rain rate of 0.3 mm h^{-1} is about 0.80 - 0.18 = 0.62. The fraction which is non-cloudy is 1.00 - 0.80 = 0.20.

In the raining fraction, the probability distribution $p(R)$ is described by a gamma distribution as in our previous work (HOMA). Fig. 4.2 illustrates the nature of this distribution for various values of the mean rain rate. At extremely low mean rates the limiting shape is exponential, while at very high mean rain rates it becomes increasingly peaked, resembling a log-normal distribution. At relevant values, up to a few mm h^{-1}, of the mean rain rates the distributions are still very skewed.

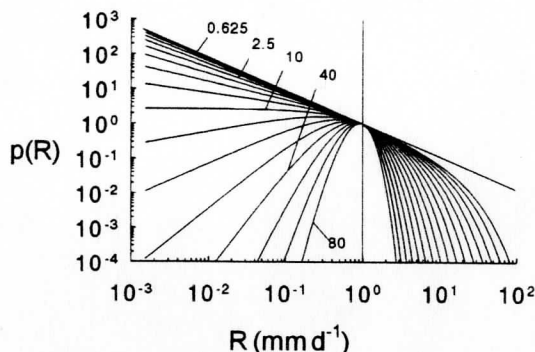Fig. 4.2. The probability density, p(R), of observing a rain rate, R, modelled by a Γ-distribution for various values of the mean rate (indicated by the labels). Note than in this figure and elsewhere in this section we are interested in the rain rates for a single realization of the data rather than monthly mean rain rates. Consequently rain rates are given in mm h^{-1}, rather than mm d^{-1} or mm mon^{-1}.

The main variation of R_i is with T_B. Environmental effects are treated as perturbations. Consequently, $R_i(T_B, SST, RH, W, Z_{fr})$ is well approximated by an expression of the form,

$$R_i = \left\{ \begin{array}{l} R_{0i} + \dfrac{\partial R_i}{\partial(RH)}(RH - 80) + \dfrac{\partial R_i}{\partial(SST)}(SST - 27.5) + \dfrac{\partial R_i}{\partial(W)}(W - 7) \\[3mm] + \dfrac{1}{2}\dfrac{\partial^2 R_i}{\partial(W)^2}(W - 7)^2 + \dfrac{\partial R_i}{\partial(Z_{fr})}(Z_{fr} - 4.5) \end{array} \right\} \qquad (4.1)$$

The subscript "i" designates the channel, and the subscript "0" designates the rain rate as a function of the ith channel brightness temperature, T_{Bi}, for a fixed set of nominal environmental conditions. These nominal conditions are: 80% relative humidity at $p \approx 1000$ mb, 27.5 °C sea surface temperature, 7 m s^{-1} wind speed at 19.5 m, and a freezing level at 4.5 km. The form of (4.1) is suggested by the Taylor series expansion of an arbitrary continuous function. Note, however, that two terms have been retained for the wind variation because its nonlinearity is important over the relevant range of wind speed values. The partial derivatives in (4.1) are all approximated by finite differences using a radiative transfer model for this set of reference conditions and departures from them of the expected magnitudes.

Our previous model (HOMA) neglected the partial derivatives and corresponded to the R_{0i} term of (4.1). Both R_{0i} and the old model R depend *only* on T_{Bi}, with similar functional relationships. The inclusion of the partial derivatives in (4.1) is the principal improvement of our current model.

4.2 Resulting Model

We have elected to replace channel 10 by an 11th synthetic channel (($T_{B\,V37} - T_{B\,H37}$) = ($T_{B\,10} - T_{B\,9}$)). This does not change the information content of the total set of channels. We do not use the two lowest frequency channels (6.6 GHz) because of their poor spatial resolution. In tests 21 GHz results consistently varied from those at other frequencies. This is not surprising, since the two 21 GHz channels are primarily intended for observing water vapor. Thus, we used six of 11 indexed channels ($i = 1, ..., 11$) to form a multichannel rain estimate. For generality, some of the unused channels still appear in tables, equations or sums, but are assigned zero weight when the algorithm is applied.

Fig. 4.3 (see the following page) illustrates $R_{0i}(T_{Bi})$ for each channel used. In the figure the $R_{0i}(T_{Bi})$ for 37 GHz are pairs of curves crossing at a common point to represent these double valued functions. At this common point scattering by precipitating ice particles (which tends to decrease T_{Bi}) begins to dominate over emission by precipitating liquid drops (which tends to increase T_{Bi}). Because of the distribution of rain rates in nature, area mean-rain rates will almost always lie on the lower of the two branches of these curves. The ambiguity in 37 GHz channels can be resolved with the help of the 18 GHz channels, if we assume these are never far beyond their crossing points.
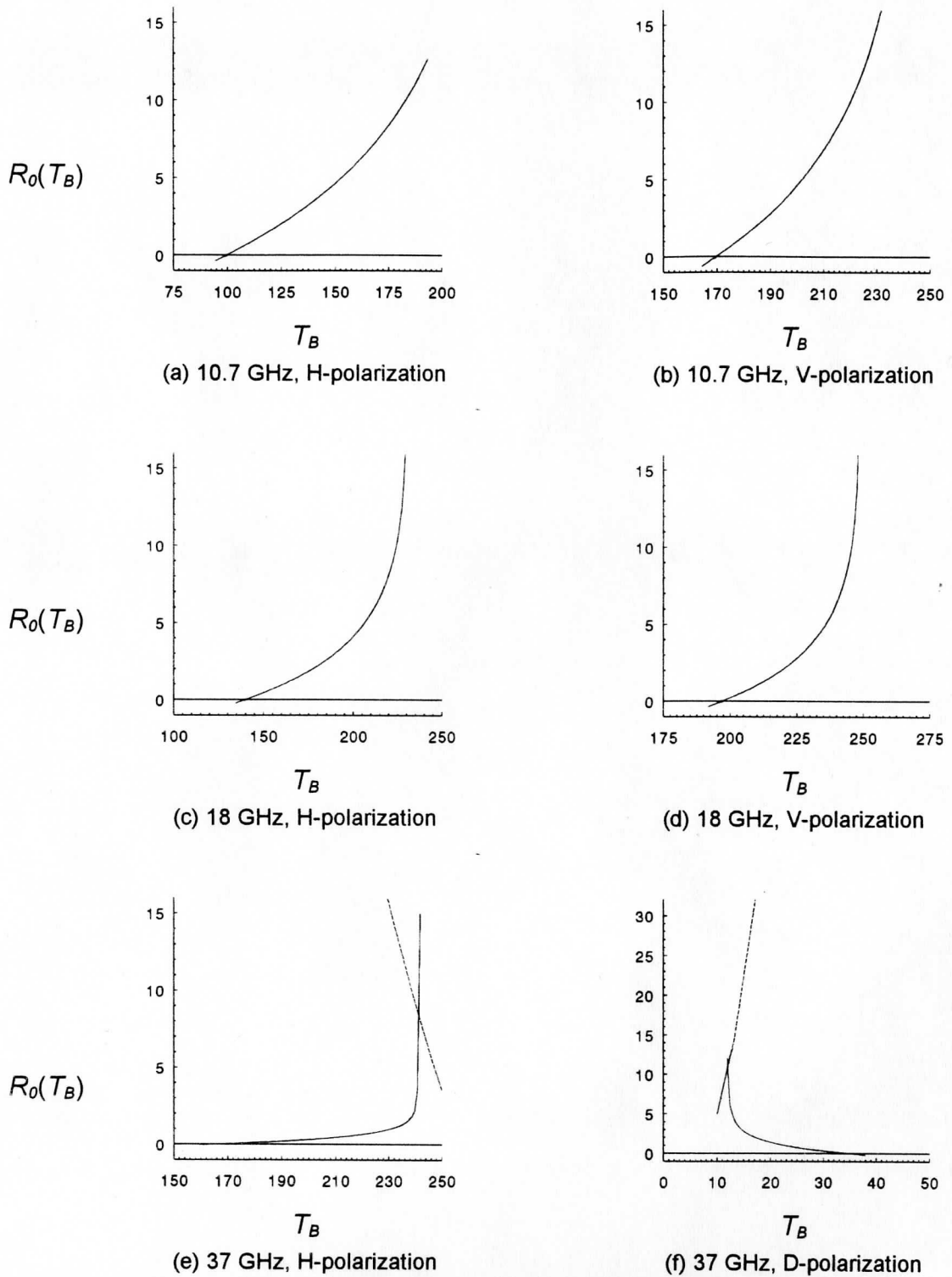
Fig. 4.3. Rain rate, in mm h^{-1}, as a function of the microwave brightness temperatures (K) used in our algorithm for standard environmental conditions.

Partial derivatives in (4.1) are illustrated in Fig. 4.4 (p. 4.6). Like $R_{0i}(T_{Bi})$ these curves are double valued for 37 GHz. When viewed as functions of T_{Bi}, the curves turn back at the T_{Bi} value corresponding to the R_0 crossover point.

Once the individual channel rain estimates are obtained, they are combined using a set of weights chosen to minimize the expected multi-channel error. In the least square sense, optimization is achieved when the error variance[1] contributed by each channel is equal to the error variance contributed by any other channel. Assuming our estimates of the environmental parameters are unbiased, and that our radiative transfer model is unbiased, the error of an individual channel, R_i, is given by (4.2).

$$\left(\delta R_i\right)_{environmental} = \left\{ \begin{array}{c} \left(\dfrac{\partial R_i}{\partial(RH)}\delta_{RH}\right)^2 + \left(\dfrac{\partial R_i}{\partial(SST)}\delta_{SST}\right)^2 \\[4mm] + \left(\dfrac{\partial R_i}{\partial(W)}\delta_W + \dfrac{1}{2}\dfrac{\partial^2 R_i}{\partial(W)^2}2(W-7)\delta_W\right)^2 + \left(\dfrac{\partial R_i}{\partial(Z_{fr})}\delta_{Z_{fr}}\right)^2 \end{array} \right\}^{1/2} \quad (4.2)$$

The δ quantities are the root mean square errors of the environmental parameters. We estimate them as follows: 3°C for SST, 5% for RH, 0.5 km for the freezing level and $3\,\mathrm{m\,s^{-1}}$ for wind. Note that the parameter Z_{fr}, which is correlated with SST, modulates the retrieved rain rates rather strongly.

In addition to errors arising from errors in environmental parameters, there is an error in each R_i due to measurement errors in T_{Bi}, that is, "noise." We take δT_{Bi} to be about 2K for all SMMR channels except the original 37 GHz channels ($i = 9, 10$) for which we take the noise to be $2\sqrt{2}$K (Gloersen and Barath, 1977). It follows that δT_{Bi} for channel 11, the synthetic $V37$-$H37$ channel, would be

$$\delta T_{B11} = \sqrt{\left(\delta T_{B9}\right)^2 + \left(\delta T_{B10}\right)^2} = 2\cdot\delta T_{Bi} \quad \text{for } i = 1,\cdots,8 \quad (4.3)$$

The expression for the rain error due to channel noise of brightness temperature is given in (4.4).

$$\delta R_{i\,noise} = \left|\dfrac{\partial R}{\partial T_{Bi}}\right|\cdot\delta T_{Bi} \quad (4.4)$$

It follows that the total error variance is given by (4.5).

---

[1] "Error variance" refers to the squared difference of the true and model-calculated values.

2/26/96 8:47 D:\SMMR_MOD\SEC__4.DOC
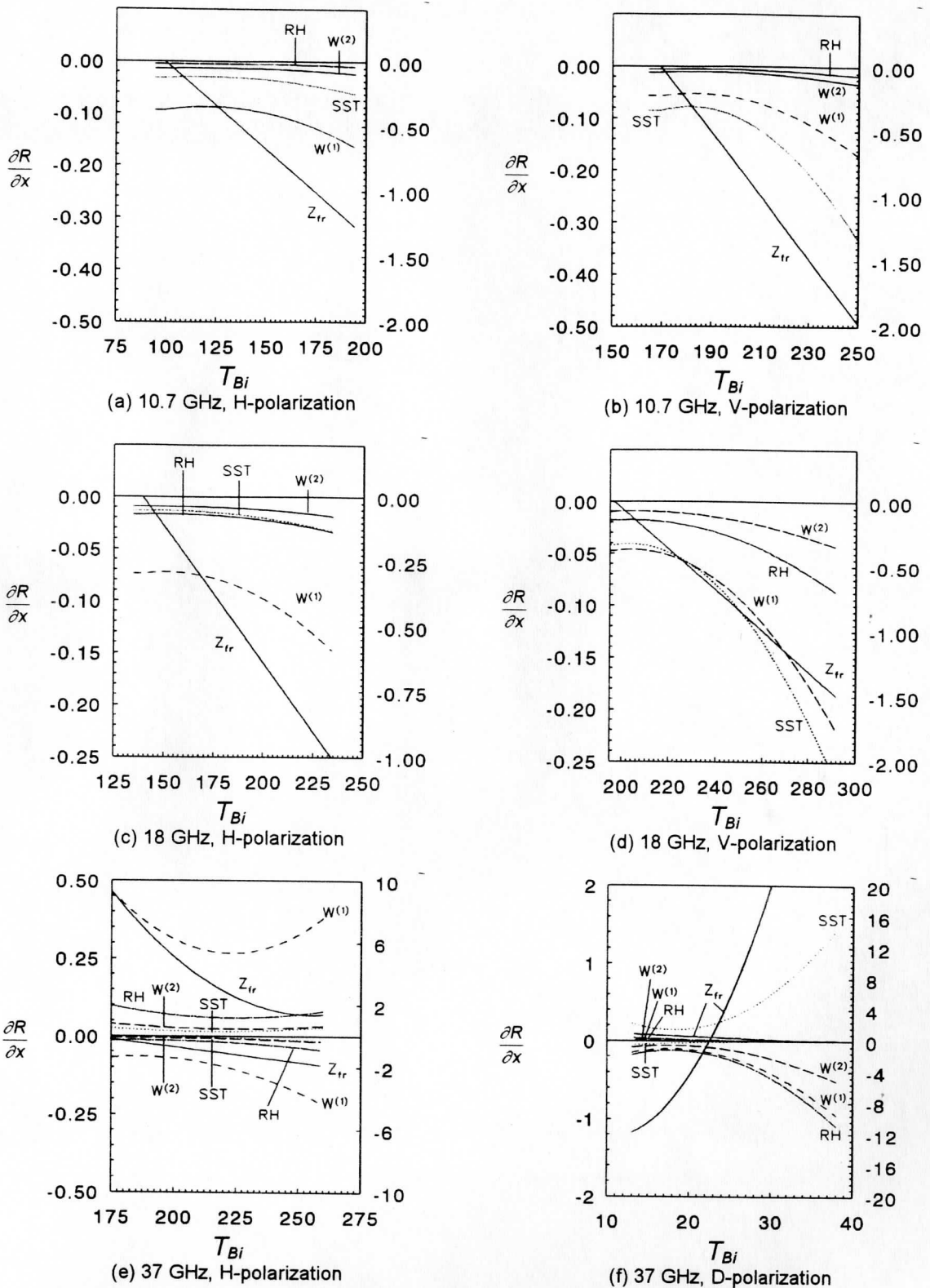
FIG. 4.5. Changes in R with environmental parameters as functions of T_{Bi}. Units are: $(mm \cdot h^{-1})/(°C)$ for SST, $(mm \cdot h^{-1})/(\%)$, for RH, $(mm \cdot h^{-1})/(km)$ for Z_{fr}, and $(mm \cdot h^{-1})/(m \cdot s^{-1})$ for both wind speed derivatives. Z_{fr} uses the right scale, other variables the left –except $\partial R/\partial W$ (i.e. $W^{(1)}$) for 37 GHz D-polarization only.

$$
(\delta R_i)^2_{total} = \left\{ \begin{array}{l} \left(\dfrac{\partial R_i}{\partial (RH)}\delta_{RH}\right)^2 + \left(\dfrac{\partial R_i}{\partial (SST)}\delta_{SST}\right)^2 + \left(\dfrac{\partial R_i}{\partial T_{Bi}}\delta T_{Bi}\right)^2 \\[3mm] + \left(\dfrac{\partial R_i}{\partial (W)}\delta_W + \dfrac{1}{2}\dfrac{\partial^2 R_i}{\partial (W)^2}2(W-7)\delta_W\right)^2 + \left(\dfrac{\partial R_i}{\partial (Z_{fr})}\delta_{Z_{fr}}\right)^2 \end{array} \right\} \tag{4.5}
$$

The weights, w_i needed for the composite rain estimate are

$$
w_i = \left\{ \begin{array}{ll} \dfrac{(\delta R_i)^2_{total}}{\displaystyle\sum_{i=1}^{11}(\delta R_i)^2_{total}} & \text{over oceans far from land} \\[10mm] \\ 0 & \text{channels 1, 2, 7, 8, and 10 or over land} \end{array} \right. \tag{4.6}
$$

Our optimized estimate of rain rate is thus given by (4.7).

$$
R = \sum_{i=1}^{11}\left(w_i \cdot R_i\right) \tag{4.7}
$$

As discussed above, $w_i \equiv 0$ for $i = 1, 2, 7, 8,$ and 10. The non-zero w_is could be independently calculated for each field of view processed if there were variations in the δ values of environmental parameters with time and location. Closer inspection of (4.5) and (4.6) shows, however, that for w_i the absolute magnitude of a δ is not as important as its size *relative to other* δs. Testing with variable environmental conditions suggested that, while some adjustments were evident, these were small enough that a formulation in which the weights are made functions of the rain rate only (by assigning constant standard values to the environmental δs) could be used for the sake of computational simplicity.

We have used the *U.S. Navy Marine Atlas*[2] as our source of monthly mean wind speed, sea surface temperature, air temperature and relative humidity data at one degree latitude-longitude resolution. We inferred our own freezing level (Z_{fr}) from surface temperatures and climato-

---

[2] CD-ROM Ver. 1.1 available from NOAA's National Climatic Data Center, Asheville, NC.

logical temperature lapse rates ($\partial T_{air}/\partial Z$) averaged over 0 to 6 km altitude.[3] We represent the information in the tables by the function below,

$$\frac{\partial T_{air}}{\partial Z} = [1 + 8.715 \cdot 10^{-7} \cdot \cos(\psi) \cdot \theta^3 \cdot (0.006094 - 4.935 \cdot 10^{-7} \cdot \theta^2)]$$

The angles θ and ψ represent latitude and days from winter solstice in radians, *i.e.*,

$$\psi = 2\pi \cdot [(\text{day of the year}) + 9] / 365.25$$

If the air temperature at the surface *in Celsius* is T_0 then the freezing level Z_{fr} is estimated as,

$$Z_{fr} = T_0 \cdot \left(\frac{\partial T_{air}}{\partial Z}\right)^{-1}$$

The calculation of relative humidity from standard formulas requires air temperatures (T_{air}), dew point temperatures (T_d), and surface pressure values (p_0) from the climatological data.

4.3 Rain Rates for Standard Conditions

When scattering is not important, and environmental conditions are constant, the SMMR rain rate and brightness temperature relations are well approximated by equations of the form:

$$T_{Bi} = T_{B0i} + A_{0i} \cdot (1 - \exp(-R_{0i} / D_{0i})) \tag{4.8a}$$

or

$$R_{0i} = -D_{0i} \cdot \ln\left(1 - \frac{|T_{Bi} - T_{B0i}|}{A_{0i}}\right) \qquad \text{if } T_{Bi} \geq T_{B0i} \tag{4.8b}$$

$$R_{0i} = +D_{0i} \cdot \ln\left(1 - \frac{|T_{Bi} - T_{B0i}|}{A_{0i}}\right) \qquad \text{if } T_{Bi} < T_{B0i} \tag{4.8c}$$

T_{B0i} is the threshold temperature for rain, A_{0i} is the "amplitude" of the temperature variation $[T_{Bi}(R = 0) - T_{Bi}(R = \infty)]$ and D_{0i} is the rain rate for unit optical depth—neglecting scattering. The last expression in this group yields *negative rain* rate by "reflection" about the threshold value of the brightness temperature, T_{B0i}. Negative rates are necessary only as an intermediate step to effectively allow the partial derivatives of rain rate as a function of brightness temperature and the other variables to adjust the threshold at which rain occurs. Negative rain rates are eliminated when we obtain the adjusted rain rate.

To simplify the above relations as well as subsequent ones, we can introduce a set of scaled brightness temperatures, $\{\tau_i\}$, defined by (4.8), allowing the above three expressions to be rewritten as (4.9a)-(4.9c).

---

[3] This is based on supplemental atmospheres (Table VI p. 31) in Rex (1969).

$$\tau_i = \frac{T_{Bi} - T_{B0i}}{A_{0i}} \tag{4.9a}$$

$$\tau_i = [1 - \exp(-R/D_{0i}] \tag{4.9b}$$

$$R_{0i} = - D_{0i} \ln(1 - \tau_i) \quad \text{if } \tau_i \geq 0 \tag{4.9c}$$

$$R_{0i} = + D_{0i} \ln(1 + \tau_i) \quad \text{if } \tau_i < 0 \tag{4.9d}$$

The index $i = 1,...,11$ refers to the individual SMMR channels plus the synthetic channel. In particular, for the values of the constants given in Table A.1 of Appendix A, equations of this form represent the basic state very well (as shown by the square of the correlation coefficient for a least squares fit in the final column of the table). The final column of the table is the maximum value of rain rate from the model runs included in the regression. Notice that all the regressions seem to be guaranteed "good" at least up to $R = 2 \cdot D_{0i}$. Since all channels have the same relation (9) between the non-dimensional temperature, τ_i, and dimensionless rain rate, R_{0i}/D_{0i}, up to $R_{0i}/D_{0i} = 2$, they can be represented by a "universal" curve as illustrated in Fig. 4.5.
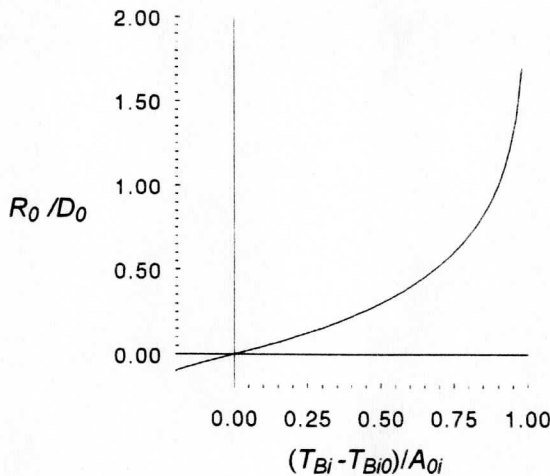

Fig. 4.5. Relation of dimensionless rain rate to dimensionless temperature, valid for all channels.

The partial derivatives in (1) are approximated from the model calculations by finite differences. If ξ is any one of the environmental parameters,

$$\left(\frac{\partial R_i}{\partial \xi}\right)_{T_B = const.} \approx \left(\frac{\Delta R_i}{\Delta \xi}\right)_{T_{Bi} = const.} = \left(\frac{\partial R_i}{\partial T_{Bi}}\right)_{\xi = const.} \cdot \left(\frac{\Delta T_{Bi}}{\Delta \xi}\right)_{R_i = const.} \tag{4.10}$$

The $\partial R_i/\partial T_{Bi}$ derivatives can be obtained from (4.8). Because, for 37 GHz, $\partial R_{0i}(T_{Bi})/\partial T_{Bi} \to \pm\infty$, where the two branches of the $R_{0i}(T_{Bi})$ function join, there are associated divergences ($\to \pm\infty$) in the other partial derivatives.

Since $\partial R_i/\partial T_{Bi}$ appears squared in every term of (4.5) it has a strong influence on the shapes of the weights calculated from (4.5) and (4.6). For frequencies below 37 GHz the

weights, w_i, will rapidly approach zero for T_{Bi} values warmer than those corresponding to $R = 2D_0$. Essentially, the weights are zero at and beyond about $R = 3D_0$. See Table A.2.

$$T_{Bi}^{(2)} = T_{B0i} + A_{0i} \cdot [1 - \exp(-2)]$$
$$T_{Bi}^{(3)} = T_{B0i} + A_{0i} \cdot [1 - \exp(-3)]$$

(4.11)

The universal curve illustrated in Fig. 4.5 is not completely adequate for understanding the use of the 37 GHz channels (*cf.* Fig. 4.4). As discussed above in connection with Fig. 4.3, once scattering becomes dominant—at rain rates around $3D_0$ and above—the 37 GHz channels may again be used to infer rain rates, but with a different relationship than used at low rain rates. This relationship is well described by a second order polynomial in τ_i (4.12). Thus, we need a reliable way to choose between *two* quite different relationships of T_{Bi} to R. Because the higher rain rates are relatively rare, the low rain rate branch is chosen by our algorithm unless the 18 GHz channels indicate a sufficiently large rain rate. Similarly, the weights calculated for the 37 GHz channels will depend on which branch of the $R(T_{Bi})$ is used.

If (R_5 and $R_6 \geq 3D_{0i}$ and $i \geq 9$) then,

$$R_{0i} = b_{0i} + b_{1i} \tau_i + b_{2i} \tau_i^2$$

(4.12)

Note carefully that the above statement is only intended apply to the 37 GHz channels at rain rates exceeding the $3D_{0i}$ values. The values of the coefficients b_{ji} in (4.12) are given in Table A.3 of Appendix A, where there is specific information on the partial derivatives and weights.

4.4 Validation

We have validated the present SMMR rain estimates using the climatic analysis of Jaeger (1976) and the highly reflective cloud (HRC) data set discussed by Garcia (1985). The latter takes the form of an index, η, of bright visible-band clouds extending 200 km or more. Once each day in a month these cloud masses are outlined on a mercator polar orbiting satellite composite image. The value of η in a one degree latitude/longitude box between $\pm 25.5°$ is incremented by one if the box is covered by highly reflective cloud. Thus the final η is the number of days in a month such cloud is present at each latitude-longitude grid point.

Jaeger's basic observational material over the oceans was frequency of rain. This was interpolated to a 5° by 5° latitude grid from isolines of monthly percentage frequency reported in the U.S. Navy Marine Climatic Atlas. A frequency was converted to rain amount, using Geiger's (1965) map and matching frequencies to rain accumulations. Finally Jaeger multiplied the amounts by 1.39 to normalize his global rain amounts to an evaporation calculation by Kessler (1968).

Jaeger's rain estimates and the HRC-index are both available in digital form for downloading via ftp from the National Center for Atmospheric Research's web-site. The data set index address is

http://www.ucar.edu/dss/index.html.

The Jaeger climatology is the data set designated DS865.0, the HRC data is designated DS740.0.

The HRC data was "calibrated" for rainfall against 820 station-months of rain gauge data from coral atolls with 30 m, or less, maximum altitude above sea level. The relation to rainfall was found by minimizing the sum of the squares of the deviations of rainfall about a linear function

$$R = a + b \cdot \eta$$

Kilonsky and Ramage (1976) reported $a = 55.3$, $b = 39.2$, whereas Garcia (1981) reports slightly different values for the same data set, $a = 62.6$, $b = 37.4$. Note that these coefficients yield monthly accumulations (or mean rates as $mm\,mon^{-1}$). It is evident from Fig. 4.5 that there is no practical difference between the two HRC regressions.

We suggest that two different relations between rain and HRC might be considered based on the same data set used by Garcia and Kilonsky and Ramage: a principal component regression and one constrained to pass through the origin. Fig. 4.6a contains an alternate (better fitting) relationship between the Jaeger analysis and SMMR rain, which passes exactly through (0,0)

$$R_{Jaeger} = \alpha \cdot R_{SMMR}^{\beta} \tag{4.13}$$

The parameters for this relation are indicated at the bottom of Table 4.1.
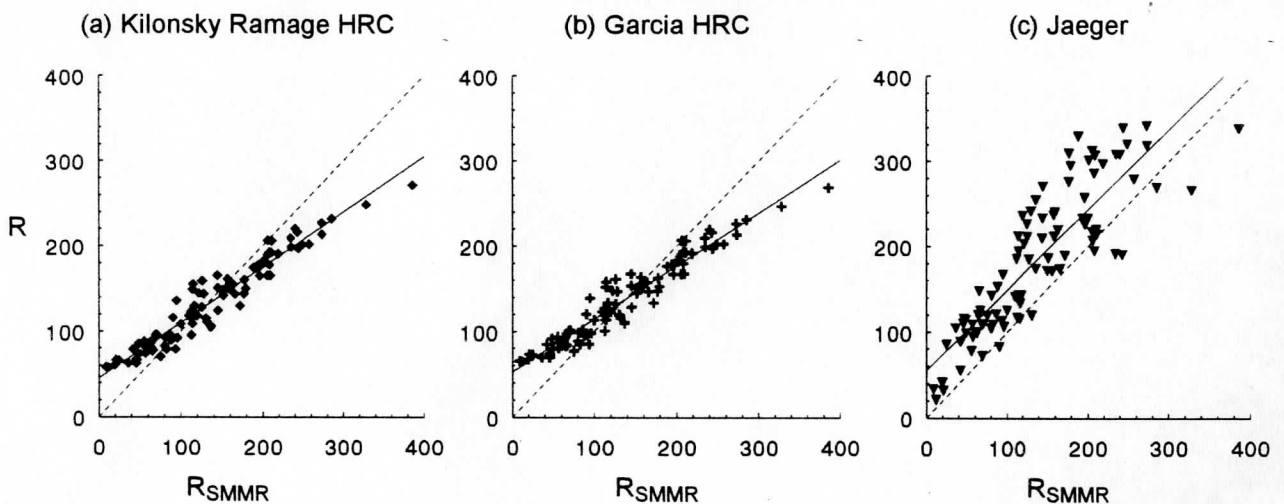
Fig. 4.6. Comparisons of SMMR monthly rain (x-axis, $mm\,mon^{-1}$) for regions 1 through 8 with that obtained from the Kilonsky and Ramage relation (a), from the Garcia relation (b), and from Jaeger's analysis (c). For convenience in comparing one panel with another as well as the relation of SMMR rain to the others, a 45° or 1:1 line (dashed) is shown in each panel as well as a regression line (solid). Coefficients and goodness of fit parameters are shown in Table 4.1.
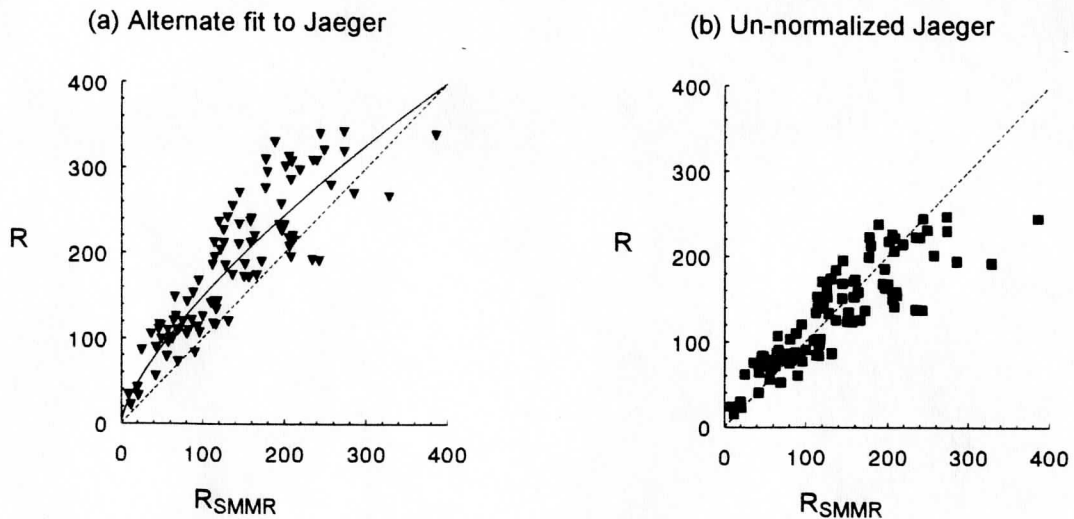
Fig. 4.6. Comparisons of SMMR monthly rain (x-axis, mm mon^{-1}) for regions 1 through 8 with Jaeger's analysis with an alternate curvefit to the SMMR data (a) and Jeager's data divided by 1.39 to remove the normalization. For convenience 1:1 line (dashed) is shown in each panel as well as a regression line (solid) in (a). Coefficients and goodness of fit parameters for (a) are shown in Table 4.1.

TABLE 4.1. Relation of SMMR monthly rain in regions 1-8 to four estimates from HRC and from Jeager's analysis within the ±25.5° latitude zone.

Relation	Figure	Constant		Coeff. of R_{SMMR}		r^2
Jaeger	4.5(c)	54.88	±8.68	0.941	±0.056	0.750
Kilonsky & Ramage HRC	4.5(a)	45.00	±2.91	0.649	±0.019	0.927
Garcia HRC	4.5(b)	52.77	±2.77	0.619	±0.018	0.927
		$\ln(\alpha)$		$\ln(\beta)$		
Alternate Jaeger relation	4.6(a)	1.724	±.155	0.7124	±0.0324	0.835

Next, consider the mean values of the 96 region-month cases shown in Table 4.2. Except for the shaded row, which contains the normalized Jaeger result, the estimates deviate from our SMMR result by less than 4%. (See Fig. 4.7.)

TABLE 4.2. Mean rain from SMMR, Jaeger, and HRC
for regions 1-8 within the ±25.5° latitude zone.

Source of rain estimate	Mean monthly rain (mm) for regions 1-8, 12 months $n = 96$
SMMR	136.6
Jaeger	183.4
Jaeger without normalization	131.9
Kilonsky & Ramage HRC	133.7
Garcia HRC	137.4

4.5 COMPARISON

By including a multiplier of 1.34, the 1992 algorithm normalized estimates of rain rate to those of Jaeger (1976). In the present version we choose not to normalize our estimates to Jaeger's estimates or to those of any other scientist. Consequently, for an identical period and similar areas, estimates made by the 1992 algorithm (hereafter, old) exceed estimates made by the present algorithm (hereafter, new). For example, over the Indian Ocean, as MHA defined it, through the years 1979, 1980 and 1981, new rainfall is 34% less than old rainfall (Table 4.3). Over the Arabian Sea the difference increases to nearly 50%.

For the Indian Ocean through the same three years, monthly mean rain rate estimated by the new scheme consistently falls short of that estimated by the old scheme (Figure 4.7). New estimates vary more than old; however, old and new curves track well. Thus, apart from the normalization, nothing in the comparisons of three-year average rainfalls (Table 4.3) or three-year average rain rates (Fig. 4.8) indicates any incompatibility between the old and new algorithms.

TABLE 4.3. Three-year means of old and new rainfall.
(1979-1981)

Region	Old (mm)	New (mm)	Difference [(old - new)/old] (%)
Indian Ocean[a]	1339	883	-34
Arabian Sea[b]	1171	592	-49
Bay of Bengal[c]	3152	1733	-45
Equatorial Strip[d]	2093	1197	-43

[a] Waters between 24.5°N and 25.5°S and 39.5°E and 109.5°E except the South China Sea, Java Sea, Gulf of Aden and Persian Gulf.

[b] The Indian Ocean north of 7.5°N and west of 75.5°E.

[c] The Indian Ocean between 80.5°E and 96.5°E and north of 9.5°N.

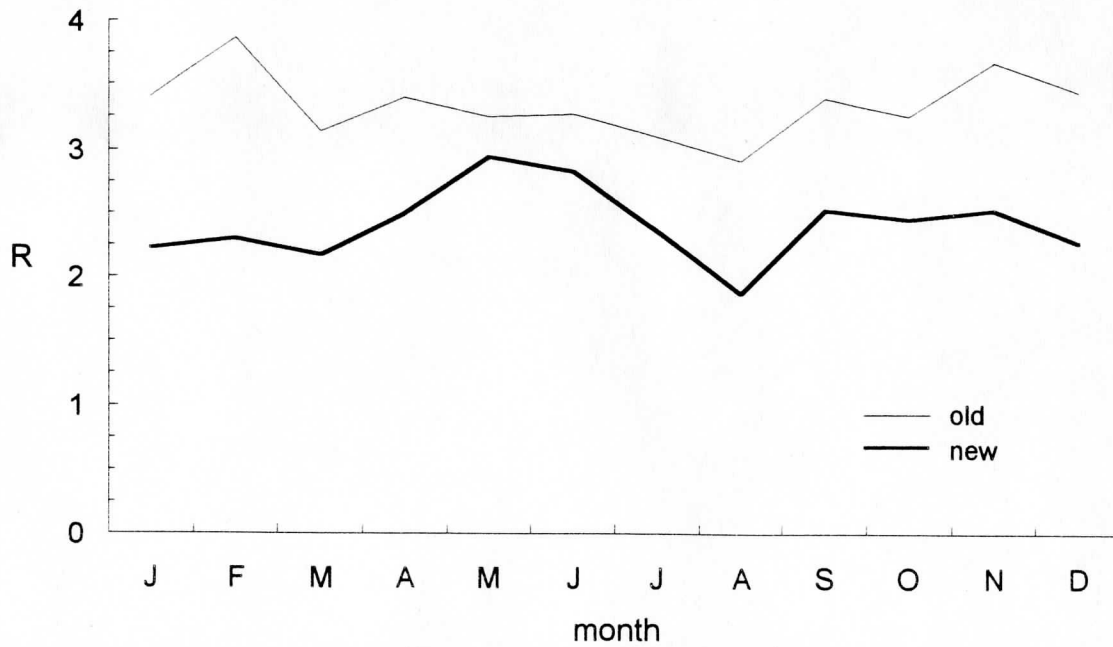[d] The Indian Ocean between 4.5°N and 5.5°S.

Fig. 4.8. Monthly mean rain rate for the Old Indian Ocean by the HOMA algorithm (old) and the present algorithm (new). Rain rate is averaged from 1979 through 1981. Units are mm d^{-1}.

5. PROCESSING

A unit of data consists of all retrievals contained within a box of one-degree latitude and one-degree longitude and a period of one day. Boxes center on whole-degree intersections of latitude and longitude. Periods begin at 00:00 UTC.

We used UNIX shell programs to preprocess the JPL tapes and C programs to convert brightness temperatures to rain rate. Preprocessing consisted of five steps (Fig. 5.1). After reading a month of data from a tape to a workstation, the shell programs identified days for which data existed. Next, day-by-day they decompressed the data and flagged each day's orbits. After writing the data and orbit information to a temperature file, the shell programs read the next month of data.

The conversion programs called HDF routines to read brightness temperature, latitude and longitude from the temperature file. They tested a location for position within the region defined by Ocean's boundaries. If the location passed the test, using the Wisconsin algorithm the program converted brightness temperatures to rain rate. Day-by-day, rates were binned by boxes, summed for all orbits and counted. For each box in the region the conversion programs wrote the rain-rate sum and count to a daily-rain file. From sets of daily-rain files, the conversion programs calculated rain rate for each of the 107 months of the SMMR record. Finally, for each month the conversion programs wrote this value and the count to separate monthly mean rain and count files. The 107 pairs of files in this set constitute the University of Wisconsin-Madison Nimbus-7 archive of SMMR rain for the monsoon oceans. Total size is about 14 Mbytes.
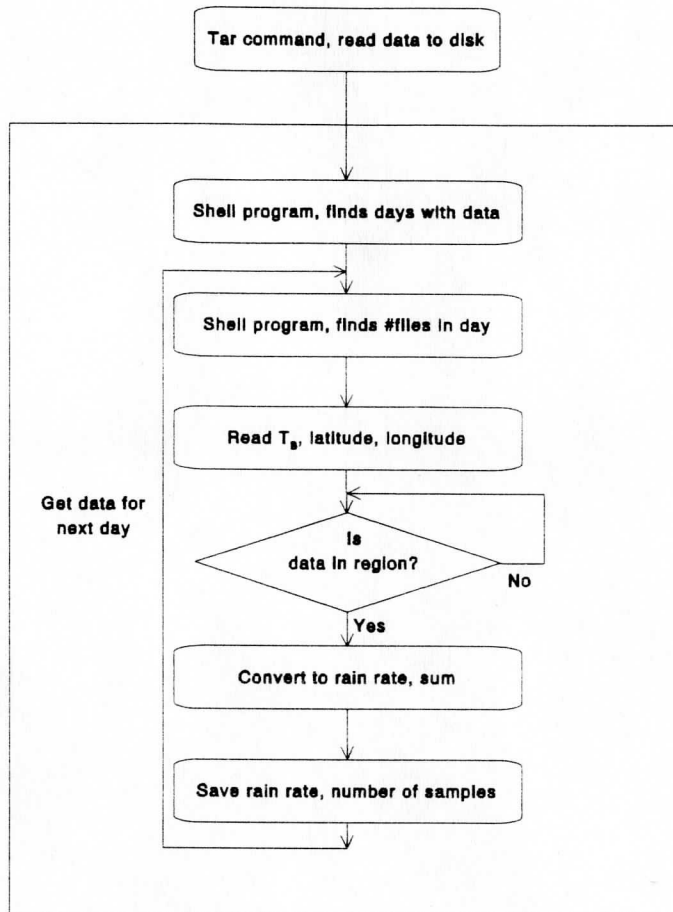
FIG. 5.1. SMMR data processing.

6. ANALYSIS

To clarify terms, we note that the NERB across the North Pacific corresponds to a persistent cloud band, the North Pacific Inter-tropical Convergence Zone (Meehl 1987; Waliser et al. 1993; Waliser and Gautier 1993) or (east of the date line) the Near-equatorial Trade Wind Convergence (Ramage 1995). The SPRB corresponds to a second persistent cloud band, the South Pacific Convergence Zone (Meehl 1987; Waliser and Gautier 1993). Commonly—and misleadingly (e.g., see Ramage 1995, pp 5-6)—meteorologists call any near-equatorial, persistent and extensive cloud band an inter-tropical convergence zone, or ITCZ. Here, we call such a feature a *Tropical Cloud Band*, or TCB.

6.1 SMMR

This section presents analyses of rain rate (in millimeters per day) calculated from SMMR. Except as noted the analyses draw on data from the "short record," the eight calendar years beginning with January of 1979. They focus on the four largest regions (Ocean, Inner Ocean, Indian Ocean and West Pacific Ocean) and conclude with an El Niño/Southern Oscillation (ENSO) event. Each of the regional analyses begins with a statistical overview. It continues with time series of rain rates and concludes with profiles of monthly average rain rates. The Ocean analysis alone covers maps and space-time sections of rain rate.

6.1.1 Ocean

Over Ocean, an area of $72 \cdot 10^6$ km^2 (about 14% of the Earth's surface; 20% of the ocean's surface), rain fell at an average rate of 2.7 mm d^{-1} (Table 6.1). From month to month, on average, it varied by 10% (Tables 6.1 and 6.2), a small amount.

Changes from year to year proved to be small also (Table 6.1; also, Fig. 6.1). On average, from year to year, rain rate varied by 7% of the mean. Later years tended to be drier than earlier years.

Monthly rain rate for Ocean, plotted in Fig. 6.2 for the period October 1978 through August 1987 (hereafter, the long record), reflects this drying trend. Linear regression suggests an average decrease of 3.9 mm a^{-1} (0.4%). Fig. 6.2 (and Table 6.1) also hints at an annual cycle, with a boreal summer-autumn maximum. This cycle peaked in the ENSO years 1982, 1983 and 1984. On average over the short record its amplitude amounts to only one-fifth of the mean. Nevertheless, the annual cycle dominates the profile of monthly mean rain rate for Ocean (Fig. 6.3).

TABLE 6.1. Ocean monthly, annual, mean monthly and mean annual rain rates.
(mm d^{-1})

Year	Month												
	J	F	M	A	M	J	J	A	S	O	N	D	all
1978	---	---	---	---	---	---	---	---	---	3.3	2.7	2.5	2.84
1979	2.2	2.7	2.5	2.5	2.7	2.8	2.6	2.7	2.8	3	3.1	2.8	2.71
1980	2.8	2.7	3.1	2.9	3	3.1	3	2.9	3.3	3	2.8	2.8	2.94
1981	2.7	2.7	2.5	2.9	2.9	2.8	2.9	3.1	2.9	3	2.8	3.2	2.88
1982	2.9	2.6	2.8	2.5	2.8	3.2	3.3	3.6	2.9	2.7	3.1	2.8	2.92
1983	3	2.5	2.2	2.4	2.5	2.7	3	3.2	2.6	3	3	2.8	2.74
1984	2.4	2.5	2	2.3	2.5	2.5	2.4	2.8	2.1	2.8	2.8	2.8	2.5
1985	2.7	2.8	2.4	2.4	2.6	2.6	2.2	2.5	2.3	2.1	2.4	2.4	2.45
1986	2.8	2.2	2.7	---	---	---	2.5	3	2.6	2.5	2.5	2.9	2.62
1987	2.5	2.8	2.1	2.8	2.4	2.9	2.5	2.1	---	---	---	---	2.51
1979-86	2.66	2.59	2.53	2.55	2.72	2.82	2.74	2.99	2.67	2.77	2.81	2.82	2.72
all	2.65	2.61	2.48	2.58	2.68	2.84	2.71	2.89	2.67	2.83	2.79	2.78	2.71

6.1.1.1 Maps

Fig. 6.4a presents the short-record map of annual mean rain rate for Ocean. As in MHA, we apply a land screen to the map: here, by flagging boxes with centers over land or within 200 km of a coastline. Despite this screen the map contains implausible features. One class of these implausible features, or artifacts, consists of limning along coastlines. Probably most of this limning results from deficient widths in the land screening rather than local enhancement of near-shore rainfall.

TABLE 6.2. Variance of monthly rain rate.
$[(\text{mm d}^{-1})^2]$

Region		Record	
name	number	short*	long**
Ocean	22	0.09	0.10
Inner Ocean	21	0.21	0.24
New Indian Ocean	17	0.26	0.26
West Pacific Ocean	20	0.85	0.87
Arabian Sea	1	1.70	1.77
Bay of Bengal	2	9.57	9.56
Arabian Sea/Bay of Bengal	18	2.99	3.06
Gan	4	1.24	1.32
Madagascar	6	1.33	1.35
Cocos	7	0.86	0.84
Madagascar/Cocos	19	0.81	0.80
Philippine Sea	3	2.85	2.95
Nauru	5	2.26	2.16
Coral Sea	8	2.76	2.86
India	---	8.55	8.29

*January 1979 through December 1986.
**October 1978 through August 1987.

Another class of artifacts consists of star-like spots. Most (if not all) of the spots correspond to small islands or clusters of small islands (Fig. 6.4b). Examples include the Comoro Islands (12°S, 44°E; at the north end of the Mozambique Channel), Niihau Island (21.9°N, 160.2°W; on the eastern edge of Ocean close to the north boundary) and Guam (13.4°N, 144.9°E; east of the Philippine Islands and north-northeast of New Guinea). This association suggests two causes, local enhancement of rain by the island (or island cluster) and land contamination of the brightness temperatures. For all but the flattest islands, probably both processes apply.

Apart from these artifacts, along parallels over Ocean the SMMR map (Fig. 6.4) is smoother than Jaeger's counterpart (Fig. 6.1). Along meridians over the West Pacific Ocean the SMMR map tends also to be smoother than Jaeger. There it suppresses the Santa Cruz Rain Node, dampens the Solomon and Philippine Island Rain Nodes and smears the New Guinean node southward into the Gulf of Carpentaria, the Arafura Sea and along the northwest coast of Australia. The SMMR map sharpens the NERB. Finally, it both weakens the SPRB and rotates the eastern part of this ridge equatorward.

In the Indian Ocean the SMMR map suppresses the Mascarene Rain Node. It shifts the Bay of Bengal Rain Node from the East Bay to the North Bay. The SMMR map holds the axis of the NERB north of Madagascar. As in MHA, it shows a weak band north of the equator; hereafter, the *North Indian Ocean Rain Band.*

Like Jaeger, SMMR shows an offset in the NERB across the East Indies (from the Southern Hemisphere over the Indian Ocean to the Northern Hemisphere over the Pacific Ocean). Nevertheless, in aggregate across Ocean the near-equatorial differences between SMMR and Jaeger emphasize the equatorial trough in rainfall and a tendency toward cross-equatorial symmetry. Distant from the equator, the differences emphasize the attraction Ocean rainfall exhibits for the south- and southeast-facing shores of south Asia and the north- and northeast-facing shores of Australia.

Coastal artifacts and a few of the island artifacts appear also in annual maps of rain rate (Fig. 6.5a-h). Otherwise, with one exception, the series suggests consistency in large-scale features in spite of variability in local features. The exception occurs in the middle of the series. Fig. 5d shows a diffuse Equatorial Pacific Rain Trough in 1982 and a weak NERB across the Indian Ocean. From 1982 to 1983 (Figs. 6.5d and 6.5e) west of the East Indies the NERB recovered; east of the Indies, it weakened. Simultaneously, the Pacific branch of the North Subtropical Rain Trough deepened and, east of New Guinea, the SPRB strengthened and lifted northward.

Drawing on Jaeger's analyses, OLR, cloud cover and station records, Meehl (1987) described the annual cycle of deep convection and rainfall in terms of three elements—the North Pacific Tropical Cloud Band (NPTCB; our term), the South Pacific Tropical Cloud Band (SPTCB; our term) and a "regional convective maximum" (hereafter, convective maximum). The NPTCB (Meehl's Intertropical Convergence Zone) lies just north of the equator. It spans the Pacific Ocean. The SPTCB (Meehl's South Pacific Convergence Zone) lies south of the equator. It extends from New Guinea southeastward into the central Pacific Ocean.

Meehl began the annual cycle in May. In OLR the NPTCB strengthens until about July, weakens until about January and then strengthens again. The SPTCB peaks in January. In strength and position the convective maximum oscillates along the axis connecting Asia, Indonesia and Australia. Approaching the ends of this axis, the convective maximum strengthens; approaching the middle, it weakens. But Meehl also found that the strength of the convective maximum over southeast Asia in July exceeds its strength over south Indonesia and north Australia in January; that the weakness of the convective maximum near the equator in April exceeds its weakness near the equator in October; and that following the January peak a part of the convective maximum trails off eastward into the central Pacific Ocean.

Fig. 6.6 presents the sequence of maps of monthly mean rain rate. Panels g and h of Fig. 6.6, corresponding to July and August, show a smear or blush of rain across the northwest corner of the Arabian Sea. This blush lacks the lumpy or granular texture of rain elsewhere in Ocean. It occurs in a corner of the Indian Ocean which ship analyses (e.g., Hastenrath and Lamb 1979;

Petty 1995) show to be dry. The shape and location of the blush coincide with the core of the Somali jet, which can generate sustained wind speeds at the surface of 15 m s^{-1} or more (Findlater, 1969; Hastenrath and Lamb 1979). Like the limning and spots in the annual mean map, probably the northwest Arabian Sea rain blush is an artifact.

Apart from the blush, the series indicates the presence of both annual and semi-annual cycles. An annual cycle prevails over bays and seas near South Asia (including the Philippine Sea); over bays and seas of southern Indonesia, northern Australia and Melanesia; and over the seas north and east of Madagascar. South of the equator, it peaks in the boreal cold season; north of the equator; in the boreal warm season. In general the semi-annual cycle prevails close to the equator.

In several respects the sequence supports Meehl's 1987 model for the South Asian/northern-Australian monsoon (also see Appendix C). Evidently, a convective maximum oscillates between South Asia in the boreal summer and northern Australia and Melanesia in the boreal winter. It waxes approaching the poleward extremes of the cycle, more strongly in the north than in the south. The convective maximum wanes approaching the equator, at least as strongly from the south as from the north. At its western end the Pacific branch of the NERB waxes and wanes through the course of the year. Especially east of the Solomon Islands, the SPRB also waxes and wanes through the course of the year, in opposition to the Pacific branch of the NERB.

The sequence qualifies Meehl's model in three main respects. First, it indicates a semi-annual cycle (peaking in February/March and August/September) in the SPRB. Second, for both the Pacific branch of the NERB and the SPRB it highlights differences in the phases of cycles of intensity and position. Third, the sequence offers little evidence for eastward propagation of rain toward the end of the boreal winter.

6.1.1.2 Time Sections

Time sections in latitude and longitude clarify the behavior of features and the interplay of the annual and semi-annual cycles. We constructed a time-latitude section by stripping the column of rain rates for a given longitude from each of the 96 grids which comprise the short record. Assembled in sequence from left to right in a new grid, the columns create a history along the longitude. Substituting rows for columns yields a time-longitude section. Time-latitude sections span the angle from 30.5°S to 30.5°N; time-longitude sections, the angle from 39.5°E to 159.5°W.

Time-latitude sections were made for every ten degrees of longitude beginning at 40°E. Of the seventeen sections, we present five, one for each 30-degree interval of longitude beginning with 60°W (Figs. 6.7a–e). The first two overlap the time-latitude sections presented by MHA.

At 60°W, a slice through the western half of the Indian Ocean, MHA found an oscillating, time-modulated band. Northbound, the band crossed the equator in April or May; southbound, in October or November. Following each crossing, the band tended to intensify. Northbound from

the equator, the band moved swiftly; southbound toward the equator, slowly. With weakening of the band at the cusp, this deceleration gave the northern part of the band a saw-tooth character. Southbound from the northern cusp, the band tended to stall on either side of the equator. Stalling imprinted stripes on the oscillating band. Intensification as the band advanced into the southern hemisphere gave the southern stripe preeminance over the northern stripe.

The present eight-year record (Fig. 6.7a) reflects the blush at the head of the Arabian Sea which we noted above. Otherwise, it underscores two asymmetries about the equator. First, the axis of the oscillating band lies south of the equator. Second, whereas excursions to the north resemble saw teeth; excursions to the south resemble spikes or snaggle teeth. In addition, Fig. 6.7a suggests that within eight to ten degrees of the equator the annual cycle yields to a semi-annual cycle (also see Appendix C). Finally, toward the middle of 1982, especially along and south of the equator, the oscillating band intensified. It remained strong into the last months of 1983.

At 90°E, a slice through the eastern half of the Indian Ocean, MHA found a stronger southern-hemisphere stripe (their "permanent band") and weaker northern-hemisphere stripe. With its center at 20°N, they also found a "seasonal band." The seasonal band reflected northbound amplification and southbound decay of the oscillating band on each northern excursion.

Except, perhaps, for the northern-hemisphere stripe, Fig. 6.7b reflects these features. Compared with the 60°E section, it also emphasizes contrasting trends in the north-side and south-side teeth (growth to the north, decay to the south). Zebra stripes close to the equator suggest meridional coherence on the time scale of a month. The oscillating band weakened early in 1982. By the middle of the following year it had regained normal strength.

At 120°E, a slice through the East Indies, Fig. 6.7c reveals much land and an artifact: at 5.5°N the island of Tawitawi. Otherwise, with one exception, it indicates equatorial symmetry. The oscillating band appears to be roughly centered on the equator, which lies just below the Tawitawi strip. Northern and southern strips suggest a strong annual cycle; the Tawitawi strip, a semi-annual cycle. The exception to this symmetry lies in the north-side teeth. Tips (in the northern strip, which corresponds with the South China Sea between China and the Philippine Islands), tend to lead roots (in the Tawitawi strip). Fig. 6.7c shows little evidence of zebra stripes. However, like Fig. 6.7b, it indicates a disturbance in 1982 and 1983. Along the Tawitawi strip the oscillating band weakened, strengthened and then relaxed.

At 150°E (Fig. 6.7d), a slice through the far western Pacific Ocean, the axis of the rain band lies north of the equator. Snaggle-teeth rather than saw-teeth define the edges of the band. Especially on the north side, teeth are ragged rather than crisp. The band breaks early in 1983.

On the dateline (Fig. 6.7e) a pair of bands straddles the equator. The band to the north pulses and oscillates. Pulses intensify the northern band just before it sends a ragged tooth far northward. Oscillations displace the axis of the band a degree or two in latitude. Oscillations phase with pulses such that the axis of the band tends to lie furthest north during tooth interludes.

The band to the south of the equator displays less of the tooth-pulse structure. As with teeth in sections further west, pulse-oscillation pairs in the southern band oppose those in the northern band. The pattern of zebra stripes re-emerges.

In the northern branch the oscillation of 1982 produced a singularity. Instead of turning northward toward the middle of that year the northern branch dropped across the equator. There it merged with the southern branch, which intensified into early 1983. Four to five months into 1983, and shortly after the southern branch began to weaken, the northern branch jumped the equator again. Though weak until the last half of 1984, it remained in the northern hemisphere through the rest of the record.

We constructed time-longitude sections for every five degrees of latitude beginning at 30°S. Fig. 6.8 presents sections for 15°S, 15°N and the equator. At the equator, for the Indian Ocean only, MHA found a large gradient in rain rate from east to west. In the east rain peaked broadly, in September or October. In the west rain peaked sharply, in May. In the middle of the Indian Ocean overlap of opposing annual cycles produced a semi-annual cycle.

At the equator over the Indian Ocean Fig. 6.8a confirms the MHA gradient, opposing annual cycles and a mid-ocean semi-annual cycle. In the west the annual cycle peaks as much as a month on either side of May; in the east, from September through November. Across the Indian Ocean rain runs to granularity rather than lumpiness. Finally, Fig. 6.8a indicates a disturbance. Anomalously high rain rates appeared in the west early in 1982, advanced eastward across the Indian Ocean and ended in the east at the beginning of 1984.

On the Pacific side, as on the Indian side, rain reflects a gradient, texture and an annual cycle. However, on the Pacific side the gradient lies off-shore and it runs from west to east; lumpiness prevails over granularity; and a single annual cycle modulates rain. On the Pacific side the annual cycle propagates eastward. Close to New Guinea, it peaks late in the calendar year; at 160°W, four to six months later. This progressive annual cycle acting on a west-to-east gradient produces tongues of rain poking east.

On the Pacific side rain also indicates a disturbance. After pushing eastward to at least 160°W, the 1982 tongue apparently returned to New Guinean waters. Arriving there a year after leaving, it merged with the 1983 tongue. This merger ended a period of reversed gradient in rainfall—dry west, wet east—across the Pacific part of the section. It led to an extended dry period, in which the 1983 tongue aborted.

Over the Indian Ocean at 15°S (Fig. 6.8b), as at the equator, rain cycled annually on each side and semi-annually in the middle; also, the first half of 1983 brought unusually heavy rains. But in several respects rain at 15°S differed from rain at the equator. First, on average it fell uniformly across the Indian Ocean. Second, the annual cycle peaked in February and March. Third, by about a half month the peak in the middle lagged the peaks on the sides. Finally, the mid-ocean semi-annual cycle resulted from the conjunction of basin-wide and local bands, each varying annually.

At 15°S in the West Pacific, as at the equator, rain cycled annually. It also reflected a disturbance which began in 1982 and cycled from a wet phase into a dry phase. But in several respects Pacific rain at 15°S differed from Pacific rain on the equator. First, as for the Indian Ocean, on average it fell uniformly across the Pacific section. Second, the annual cycle was both strong and pervasive. Third, the annual cycle progressed from east to west rather than from west to east. Finally, 1984 was not dry.

At 15°N (Fig. 6.8c) in the Pacific east of the Philippine Islands, we find an artifact, the island of Guam. Otherwise, rain tended to be lumpy rather than granular. Over the Indian Ocean, as at the equator, at 15°N rain decreased from east to west and cycled annually. In several respects rain at 15°N differed from rain over the equator. First, the amplitude of the annual cycle was greater. Second, the annual cycle peaked in July or August. Third, this peak occurred first in the west. Fourth, especially in the west, the change from dry to wet occurred abruptly. Over the Bay of Bengal, May brought the dry-to-wet change, or onset. Over the Arabian Sea, on average, June brought onset; however, by about half a month, there onset in the west led onset in the east.

In the West Pacific at 15°N, as at the equator, rain formed tongues poking eastward and upward. 1982 brought a strong tongue; 1983 and 1984, weak tongues. Compared with the equatorial section, in the Pacific at 15°N the gradient of rain was weak. Tongues were strong. From west to east, rain in the tongues peaked in September or October and in October or November.

From the Bay of Bengal across the South China Sea to the Pacific Ocean east of the Philippine Islands, the phase of the annual cycle lagged and its amplitude diminished. Despite the shorter distance, phase and amplitude changed more across the Philippine Islands than across Indochina.

6.1.1.3 Harmonic Maps

Harmonic analyses offer concise views of both annual and semi-annual cycles. Figs. 6.9 and 6.11 show amplitude as tones of gray and phase as arrows centered on every second grid point within Ocean. For the annual cycle (Fig. 6.9), one month corresponds to an hour-arc on the harmonic dial. The year starts at a clock time of 00:00.

In Fig. 6.9 we find a belt of small amplitudes roughly centered on the equator. Belts of large amplitudes flank the low-amplitude belt. Over water, if not over land, the large-amplitude belts extend poleward roughly to the axes of the Subtropical Rain Troughs.

The small-amplitude belt weakens approaching the East Indies from either side. Within it a finger of locally small amplitude traces the axis of the NERB eastward from the Caroline Islands into North Pacific Ocean; another finger traces the axis of the SPRB east-southeastward along and beyond the Solomon Islands. Overall, the northern large-amplitude belt dominates the southern large-amplitude belt. It peaks over the Bay of Bengal. Opposite the Bay of Bengal peak the southern large-amplitude band breaks. A broad peak lies along the band to the west, between

Diego Garcia and the Mascarene Islands. A stronger peak lies along the band to the east, between Australia and the East Indies.

In the small-amplitude belt on the Indian Ocean side of the East Indies the annual cycle peaks in the boreal autumn (September or October). On the Pacific side it peaks in the boreal spring (March, April or May). In the large-amplitude belt north of the equator the annual cycle tends to peak in the boreal summer. Along south Asian shores it peaks early (July or August); over the West Pacific Ocean, late (August or September). But in the Pacific along the equatorial side of the NERB small-amplitude finger the annual cycle peaks in the boreal spring. Except for the eastern Indian Ocean, in the large-amplitude belt south of the equator the annual cycle tends to peak in the boreal winter (January and February). In the eastern Indian Ocean, on the south flank of the south large-amplitude belt, it peaks as late as May.

Wang's (1994) harmonic maps for the annual cycle in global OLR contain most of these elements. They differ in lacking fingers and in equivocating on the phasing of the annual cycle over the Pacific Ocean near the East Indies and over the Indian Ocean west of Australia. The finger difference, if not the phase equivocations, could result from the coarser resolution of Wang's analysis.

We define a propagation path as the locus of points which connects successive phases spanning at least one-third of a wave cycle ($2\pi/3$ radians). A propagation path begins where a local maximum in amplitude coincides with a singularity in phase. It is not allowed where amplitude falls either to an absolute minimum or to small values or where phase requires strong curvature.[1] The wave propagates swiftly where the phase slope is flat; slowly, where steep. In Fig. 6.10 propagation paths for the annual cycle tend to parallel meridians and break down close to the equator. Southbound paths start at or near the heads of the three main south Asian embayments. The Bay of Bengal path ends short of the equator. Both the Arabian Sea and South China Sea paths can be traced across the equator, the former to the vicinity of Mauritious and the latter to the Timor Sea.

Northbound paths tend to be weaker than southbound paths. One runs from the Mozambique Channel across the Arabian Sea. Together with the Arabian-Sea-to-Mauritius path (and an aborted path down the west flank of the Bay of Bengal), this path suggests a clockwise loop in the annual cycle of rain over the northwest half of the Indian Ocean. A second northbound path runs from the Arafura Sea across the equator and into the West Pacific east of the Philippine Islands. Together with paths in the Bay of Bengal and the South China Sea, this path suggests a counterclockwise loop in the annual cycle of rain between the Indian Ocean and the West Pacific Ocean.

Only the Mozambique-Channel-to-Arabian-Sea propagation path matches any identified by Wang (1994) for the annual cycle in OLR. Part of the difference stems from the broader scope of Wang's analysis; another part may be due to differences in the definitions of propagation paths. In any case, to the extent that it exists, the counterclockwise loop implies that Meehl's (1987)

---

[1] To help identify these regions we referred to maps of amplitude-to-mean ratios, one map for each cycle. Appendix C contains these maps.

convective maximum would favor the Indian Ocean side of the East Indies on its southbound leg (though not the equatorial waters of the Indian Ocean); on its northbound leg, the Pacific side. However, the northern part of this propagation path and its neighbors in the Arabian Sea and South China Sea might seem to contradict the concept of onset of the Asian southwest monsoon, as described, for example, by Mooley and Shukla (1987).

For the semi-annual cycle (Fig. 6.11) one month corresponds to two hour-arcs. Both the year and the half-year begin at 00:00 on the harmonic dial. For the sake of simplicity this discussion refers only to the month of the first peak of the semi-annual cycle. In every case the second peak occurs exactly six months later.

North Indian Ocean amplitude dominates South Indian Ocean amplitude. Narrow belts of large amplitude lie along the NERB in the West Pacific Ocean and along the axis of the SPRB; a broad belt lies across the East Indies between South Asia and North Australia. Amplitude peaks over the Bay of Bengal. In most boxes semi-annual amplitude falls short of annual amplitude. In most areas patterns in semi-annual amplitude lack the smoothness of patterns in annual amplitude.

Fig. 6.12 maps a ratio of amplitudes, that of the semi-annual cycle (C_2) to that of the annual cycle (C_1). To assure stable values, C_1 was offset by 5 mm d^{-1}. Compared with annual amplitude, semiannual amplitude dominates the regions between the axes of the NERB and companion bands—the North Indian Ocean Rain Band and the SPRB. We do not find the meridional band of large values Wang (1994) maps along the western flank of the Indian Ocean.

Although variable, phase suggests symmetry about the equator (Fig. 6.11). Along the equator the semi-annual cycle tends to peak in spring and autumn. Away from the equator, it tends to peak in summer and winter. Rain bands and the East Indies disturb this symmetry. Along the core of the Pacific branch of the NERB the semi-annual cycle peaks in May; along the core of the SPRB (east of the Solomon Islands), in February; and along the equator just east of the Indies, in June.

For the semi-annual cycle the main propagation paths originate on or near the equator (Fig. 6.13). In the Indian Ocean most lead northward. Near Sumatra the paths start in April; in the west-central Indian Ocean, up to a month later. Whether they enter the Bay of Bengal or the Arabian Sea, paths from these sources arrive at the head of the embayment half a cycle—about three months—after starting. In April a more diffuse source region just south of the equator in the far western Indian Ocean sends a path north-northeastward into the Arabian Sea. This path covers half the length of the Arabian Sea in the first month. From the equatorial source near Sumatra one path appears to lead northeastward to waters of the South China Sea just west of the Philippine Islands. Another leads southeastward as far as the south coast of Java.

In May and June the Sulu and Celebes Seas appear to spawn two paths. One drops southward into the Arafura Sea, arriving in August. The second leads northeastward, arriving in waters north of the Caroline Islands in September.

The Indian Ocean paths conform with an onset for the south Asian monsoon which originates in April along the equator near Sumatra and south of the equator near Africa. The onset impulse originates nearly simultaneously from Sumatra westward along the equator into the central Indian Ocean. From near-equatorial source regions in the central and eastern Indian Ocean and the near-African source region in the far western Indian Ocean the onset pulse moves northward into the Arabian Sea and Bay of Bengal. It may also move northeastward across the South China Sea. Along the coast of Africa and (apparently) across the South China Sea it moves swiftly; along the eastern flanks of the Arabian Sea and Bay of Bengal, slowly. Apparently, too, the pulse amplifies as it advances.

The Sumatra-to-Java path and the Sulu/Celebes-to-Arafura path conform to a similar— albeit weaker—onset pattern for the north Australian monsoon. In this pattern the onset impulse appears in October on the eastern flank of the Indian Ocean and one to two months later in the far West Pacific Ocean.

Analyzing OLR, Wang (1994) also shows onset sources along the equator and propagation both northwestward and southeastward from an East Indian Ocean source. He does not find an off-shore African source, but does identify a South Pacific source. The African source may be too subtle to register well in OLR. Our phase diagram merely hints at a South Pacific source. In any case, across the East Indies holes complicate the interpretation of our phase map.

With certain qualifications the Ocean analyses confirm the following elements of Meehl's 1987 model. First, they show two rain bands and a convective maximum. Second, whereas the rain bands flank the equator in the West Pacific, the convective maximum oscillates across the equator between Australia/Indonesia/Melanesia and south Asia. Third, with a lag of one to two months, the convective maximum follows the declination of the sun. Fourth, it peaks a month or two after the solstices. Last, the rain bands tend to wax as the convective maximum approaches and wane as it recedes.

The Ocean analyses support an equatorially asymmetric amplitude of the convective maximum, with an absolute nadir on the northbound crossing and an absolute apex on the northern cusp. They do not support the notion of a split in the West Pacific Ocean. Rather, they suggest that the convective maximum oscillates in a counterclockwise loop centered roughly on the East Indies. Further, they suggest the presence of a second loop connecting the Bay of Bengal and the Indian sector of South Asia with Madagascar and the southwest Indian Ocean. In this loop convection moves clockwise.

6.1.2 Inner Ocean

Over Inner Ocean,[2] an area of $46 \cdot 10^6$ km^2 (about 65% of Ocean), rain fell at an average rate of 3.2 mm d^{-1} (Table 6.3), 17% greater than the average rate over Ocean. From month to month, on average, it varied by about 14% (Tables 6.2 and 6.3); from year to year, by only 6%. As expected, from year to year Inner Ocean rain rate tracked rain rate over Ocean (Fig. 6.1).

---

[2] See Table 2.1 and Fig. 2.1a for the definition of this region.

Monthly rain rate for Inner Ocean (Fig. 6.14) replicates the drying trend observed in monthly rain rate for Ocean. For Inner Ocean rain decreased by 5.8 mm a^{-1} (0.5%). The Inner Ocean time series contains a stronger annual cycle, which emerges most clearly in 1982 and 1983. It also contains fragments of a semi-annual cycle.

The profile of monthly mean rain rate for Inner Ocean (Fig. 6.3) confirms the stronger annual cycle at Inner Ocean and indicates a phase difference of about half a season, Inner Ocean leading Ocean. Fig. 6.3 also confirms the presence of a semi-annual cycle in the record at Inner Ocean, with peaks occurring roughly in May and October.

TABLE 6.3. Inner Ocean monthly, annual, mean monthly
and mean annual rain rates.
(mm d^{-1})

Year	Month												all
	J	F	M	A	M	J	J	A	S	O	N	D	
1978	---	---	---	---	---	---	---	---	---	4.2	3.3	2.7	3.36
1979	2.3	2.9	2.9	3.0	3.2	3.4	3.2	3.3	3.5	3.4	3.6	3.4	3.17
1980	3.2	3.3	3.3	3.1	3.6	3.8	3.6	3.6	4.0	3.6	3.2	3.3	3.46
1981	3.1	2.9	2.6	3.4	3.5	3.3	3.6	3.8	3.6	3.8	3.3	3.9	3.38
1982	3.2	2.8	3.1	2.6	3.4	3.9	4.3	4.3	3.2	2.9	3.1	3.2	3.34
1983	3.2	2.7	2.4	2.8	2.8	3.2	3.7	3.9	3.3	3.7	3.5	3.3	3.20
1984	3.0	2.7	2.1	2.7	3.1	3.2	2.8	3.4	2.4	3.4	3.4	3.2	2.95
1985	3.1	3.4	2.7	2.7	3.1	3.3	2.5	3.2	3.0	2.5	2.8	2.9	2.92
1986	3.4	2.5	3.2	---	---	---	3.0	3.7	3.2	2.8	3.0	3.1	3.09
1987	2.4	2.9	2.2	2.9	2.5	3.5	3.0	2.5	---	---	---	---	2.75
1979-86	3.06	2.88	2.78	2.89	3.24	3.44	3.34	3.62	3.25	3.28	3.24	3.29	3.19
all	2.99	2.88	2.71	2.90	3.15	3.45	3.30	3.51	3.25	3.38	3.24	3.22	3.16

As expected, for equatorially-paired regions subject to ENSO, monthly rain rate for Indian Ocean correlated inversely with monthly rain rate for West Pacific Ocean and monthly rain rate for Gan correlated inversely with monthly rain rate for Nauru (Table 6.4). As expected, also, for cross-equatorially-paired regions subject to an annually-oscillating convective maximum (Meehl 1987), monthly rain rate for Bay of Bengal correlated inversely with that for Coral Sea. Unexpectedly, for regions paired along the equator, Gan and Nauru correlated less strongly than Indian Ocean and West Pacific Ocean. Unexpectedly, too, for regions flanking the axis of oscillation, Philippine Sea correlated at least as strongly with Cocos as did Bay of Bengal with Coral Sea (0.90 versus 0.85).

TABLE 6.4. Pairwise regression of 1979-1986 monthly rain rate for selected regions of Inner Ocean.

| Variable | | | | Statistic | |
| independent (x) | | dependent (y) | | explained variance | slope |
no.	name	no.	name	(%)	(mm d^{-1})
17	New Indian Ocean	20	West Pacific Ocean	38	-1.47
4	Gan	5	Nauru	7	-0.16
2	Bay of Bengal	8	Coral Sea	72	-0.37
3	Philippine Sea	7	Cocos	81	-0.37

6.1.3 Indian Ocean

Looking at the Indian Ocean MHA found that several features of the seasonal cycle of rain could be explained in terms of an interhemispheric "wave." This wave moved counterclockwise east and north in the boreal spring and clockwise south and southwest in the boreal fall and winter. It modulated the persistent bands of rain and activated the transient bands of rain. Thus, rain falling over the southwestern as well as northeastern reaches of the tropical Indian Ocean left the monsoon signature of an annual cycle with a summer peak.

Over Indian Ocean, an area of 24·106 km^2 (about 34% of Ocean), rain fell at an average rate of 2.4 mm d^{-1} (Table 6.5), 10% less than the average rate over Ocean. From month to month it varied by about 20% (Tables 6.2 and 6.5); from year to year, by 9%. Much of the annual variation resulted from a single year, 1983, which was anomalously wet (Table 6.5 and Fig. 6.15).

Monthly rain rate for Indian Ocean (Fig. 6.16) shows neither trend nor annual cycle. Rather, except for 1983, a semi-annual cycle dominates the series. The profile of monthly mean rain rate (Fig. 6.17) indicates May/June and November/December peaks for this cycle.

As expected, monthly rain rate over the Arabian Sea couples directly with monthly rain rate over the Bay of Bengal, at a ratio of 1:1.5 to 1:2 (Table 6.6). Madagascar couples inversely with Bay of Bengal, at a ratio of ~1:3. The northern part of the Indian Ocean (Arabian Sea/Bay of Bengal region) also couples inversely with the southern part of the Indian Ocean (Madagascar/Cocos region.

Unexpectedly, rain rate over Gan shows no dependence on rain rate over other regions of the Indian Ocean. Also, the variance of Bay of Bengal rain rate explained by its association with

TABLE 6.5. New Indian Ocean monthly, annual, mean monthly
and mean annual rain rates.
$(mm\ d^{-1})$

Year	Month												all
	J	F	M	A	M	J	J	A	S	O	N	D	
1978	---	---	---	---	---	---	---	---	---	3.0	2.2	2.2	2.47
1979	1.8	2.8	2.3	2.3	2.4	2.9	2.0	1.7	2.7	1.8	2.5	2.2	2.28
1980	2.9	2.3	1.9	2.4	3.0	3.0	2.4	1.9	2.1	2.7	2.6	2.3	2.46
1981	2.3	1.8	2.5	2.8	3.7	2.6	2.6	1.9	2.8	2.9	2.5	2.5	2.58
1982	2.6	2.1	1.9	2.1	3.1	3.0	2.5	2.0	1.8	2.1	3.0	3.5	2.47
1983	3.3	2.8	2.7	3.8	2.8	2.7	3.2	2.9	2.5	2.7	2.3	2.9	2.88
1984	2.9	2.5	1.8	2.9	3.0	2.3	2.6	1.8	1.9	1.5	2.6	2.3	2.35
1985	2.9	2.5	1.8	2.9	3.0	2.3	2.6	1.8	1.9	1.5	2.6	2.3	2.35
1986	3.1	2.0	3.0	---	---	---	1.9	1.8	1.7	2.2	1.6	2.4	2.19
1987	2.6	1.9	2.0	2.8	2.4	3.1	1.6	1.6	---	---	---	---	2.24
1979-87	2.73	2.34	2.24	2.73	3.00	2.69	2.48	1.98	2.17	2.17	2.48	2.54	2.45
all	2.71	2.30	2.22	2.74	2.93	2.73	2.38	1.93	2.17	2.27	2.45	2.50	2.44

Madagascar rain rate is as large as the variance explained by its association with Arabian Sea rain rate. In accord with 60°E and 90°E time-latitude sections (Figs. 6.7a and 6.7b) and the equatorial time-longitude section (Fig. 6.8a), Gan's independence of regions to the north and south suggests more variability at short periods and less at long periods. In accord with the 60°E and 90°E time-latitude sections (Figs. 6.7a and 6.7b) and the 15°N time-longitude section (Fig. 6.8c), the equivalence of explained variances suggests a phase difference between the Arabian Sea and Bay of Bengal.

TABLE 6.6. Selective pairwise regression of 1979-1986 monthly rain rate for regions of the New Indian Ocean. Values of slope (mm d^{-1}) lie above the (1,1; 19,19) diagonal; values of explained variance (per cent), below the diagonal.

Independent Variable		Dependent Variable						
no.	name	1	2	4	6	7	18	19
1	Arabian Sea	---	1.71	0.20	-0.50	-0.20	---	---
2	Bay of Bengal	52	---	0.04	-0.30	-0.10	---	---
4	Gan	5	1	---	-0.10	-0.10	---	---
6	Madagascar	26	52	0	---	0.42	---	---
7	Cocos	8	12	1	27	---	---	---
18	Arabian Sea/Bay of Bengal	---	---	---	---	---	---	-0.30
19	Madagascar/Cocos	---	---	---	---	---	34	---

6.1.4 West Pacific Ocean

Over West Pacific Ocean, an area of 22·106 km^2 (31% of Ocean), rain fell at an average rate of 4 mm d^{-1} (Table 6.7), nearly 50% greater than the average rate over Ocean. From month to month it varied by 23% (Tables 6.2 and 6.7); from year to year, by 9%. Like rain over Ocean, rain over West Pacific Ocean tended to decline over the period (Fig. 6.15).

Monthly rain rate for West Pacific Ocean (Fig. 6.16) shows an annual rather than a semi-annual cycle. As in the time series for Ocean, this annual cycle grew between 1981 and 1982 and shrank between 1983 and 1984. Over West Pacific Ocean rain rate plunged late in 1982. The

profile of monthly average rain rate (Fig. 6.17) reflects indications of a strong annual cycle. It also suggests that over West Pacific Ocean the annual cycle peaked late in the boreal summer.

West Pacific Ocean covers an area 8% smaller than that of Indian Ocean. Over West Pacific Ocean rain fell at a rate 64% greater than that of Indian Ocean and it declined over the record rather than remaining constant. In an absolute sense it varied more from year to year and tended to vary in opposition to rain over Indian Ocean. Thus, whereas it brought less rain to West Pacific Ocean, 1983 brought more to Indian Ocean. Finally, over West Pacific Ocean the annual cycle dominated the semi-annual cycle; furthermore, rain rate peaked there three months after peaking over Indian Ocean.

TABLE 6.7. West Pacific Ocean monthly, annual, mean monthly and mean annual rain rates.
(mm d^{-1})

| Year | Month | | | | | | | | | | | | |
	J	F	M	A	M	J	J	A	S	O	N	D	all
1978	---	---	---	---	---	---	---	---	---	5.4	4.4	3.2	4.33
1979	2.8	3	3.5	3.7	4.1	4	4.5	5	4.4	5.2	4.8	4.8	4.15
1980	3.5	4.3	4.8	3.8	4.3	4.7	4.9	5.4	5.9	4.6	3.9	4.5	4.55
1981	4	4.1	2.7	3.9	3.2	4.1	4.7	5.9	4.4	4.7	4.1	5.3	4.26
1982	3.9	3.5	4.4	3.2	3.8	4.9	6.2	6.7	4.7	3.9	3.3	3	4.29
1983	3	2.5	2.1	1.8	2.9	3.6	4.4	4.9	4.1	4.8	4.7	3.7	3.55
1984	3	3	2.4	2.6	3.2	4.1	3	5.1	3	5.5	4.3	4.2	3.61
1985	4.1	3.2	3.8	3.3	3.1	4.6	3.4	4.2	4.3	3.1	3.4	3.8	3.68
1986	3.7	3	3.4	---	---	---	4.1	5.6	4.8	3.6	4.5	3.9	4.06
1987	2.3	3.9	2.3	3.1	2.7	4	4.4	3.6	---	---	---	---	3.29
1979-86	3.51	3.32	3.39	3.17	3.5	4.3	4.4	5.35	4.44	4.42	4.13	4.16	4.02
all	3.37	3.39	3.27	3.16	3.39	4.27	4.4	5.16	4.44	4.53	4.16	4.05	3.97

6.1.5 1982-1984 Event

Time series of anomalous monthly rainrate (δR) present a clearer picture of the event which occurred in 1982, 1983 and 1984. Each δR time series refers to a particular region. It was constructed in two steps. First, we created a time series consisting of eight cycles of monthly mean rain rate. Then, month by month, this series was subtracted from the corresponding time series of monthly rain rates.

Over West Pacific Ocean (Fig. 6.18) beginning late in 1981 rain rate tended to ramp up. After falling precipitously from a July/August peak, it tended to remain low until the last half of 1984. Over West Pacific Ocean, therefore, the event occurred in two stages, wet and dry, with wet preceding dry. In amplitude, wet dominated dry; in duration, dry dominated wet.

Over Coral Sea (roughly, the southern fifth of West Pacific Ocean) 1982 and 1983 tend to be slightly wetter than others in the record (Fig. 6.19c). Over Nauru (roughly, the middle fifth of West Pacific Ocean), late 1982 marks a divide separating mostly high rain rates in the first half of the record from mostly low rain rates in the second half (Fig. 6.19b). Over Philippine Sea (roughly the northern three-fifths of West Pacific Ocean) late 1982 marks the onset of a year of low rain rates. Records for each region show a spike in July or August of 1982 (Fig. 6.19a).

Indian Ocean (Fig. 6.20) shows a weak event. As in West Pacific Ocean it involves 1982 and 1983 and occurs in two stages. However, over Indian Ocean the stage of low rain rates precedes rather than follows the stage of high rain rate. The stage of high rain rates dominates the stage of low rain rates and the event appears to end with 1983.

In summary, the anomaly plots reveal a two-stage event. This event began in 1982 and ended in 1983 or 1984. Over most of the Indian and West Pacific Oceans the first stage gave way to the second late in the boreal summer of 1982. The event was stronger in the West Pacific Ocean than in the Indian Ocean. In the West Pacific the wet stage came first, but the dry stage dominated. In the Indian Ocean the dry stage came first, but the wet stage dominated. In outline, such a pattern conforms with Lau and Chan's (1986) depiction of the 1982/1983 ENSO through time-longitude sections of OLR; it conforms as well with two views of rainfall in the 1982/1983 ENSO presented by Prabhakara et al. (1986).

6.2 SMMR and Gauge

MHA raised the question of how rain over India relates to rain over the Indian Ocean. Associating India rainfall with the position of the India band, Ramesh Kumar and Prasad (1995, p. 10) inferred an inverse relationship. However, for the years 1979 through 1986, Fig. 6.21 suggests a direct relationship. We find that India annual rain rate correlates with Indian Ocean annual rain rate as 0.84.

In fact, India annual rain rate correlates positively with annual rain rate for each of the three cross-basin regions of the Indian Ocean. It is smallest for Gan (0.44). It is highest—not for Arabian Sea/Bay of Bengal (0.59)—but for Madagascar/Cocos (0.94).

For monthly rain rates the correlations decrease and ranks change (Table 6.8, middle columns). India correlates most strongly with Bay of Bengal (0.74). It correlates as strongly with Arabian Sea (0.63) as with Madagascar (-0.65). Monthly rain rate for India correlates as strongly with monthly rain rate for Philippine Sea as with monthly rain rate for Arabian Sea.

For anomaly of monthly rain rates (δR), again the correlations decrease (Table 6.8, right-hand columns). However, with one exception, distance rather than cross-equatorial symmetry determines rank. Of the individual regions (1, 2, 3, 4, 5, 6, 7 and 8) India correlates most strongly with the two nearest regions (Arabian Sea and Bay of Bengal; ~0.35). It correlates less strongly (0.25) with Philippine Sea, the only other neighbor occupying the same belt of latitude. Correlations of India with other regions—including Madagascar—shrink into insignificance.

Meehl's (1987) model for the annual cycle of the monsoon system suggests that correlations of India monthly rain rate with regional rain rate might depend on differences in the

TABLE 6.8. Pairwise regression of 1979-1986 monthly rain rate for India on monthly rain rate for each region of Inner Ocean. Original and anomaly series.

| Region | | Series | | | |
| no. | name | original | | anomaly | |
		slope (mm d^{-1})	explained variance (%)	slope (mm d^{-1})	explained variance (%)
1	Arabian Sea	1.42	40	0.36	12
2	Bay of Bengal	0.71	55	0.19	14
3	Philippine Sea	1.12	41	-0.2	6
4	Gan	-0.24	1	0.11	2
5	Nauru	-0.11	0	0.02	0
6	Madagascar	-1.65	42	0.13	1
7	Cocos	-1.13	13	0.01	0
8	Coral Sea	-0.87	24	0.03	0
18	Arabian Sea/Bay of Bengal	1.26	55	0.52	24
19	Madagascar/Cocos	-1.89	33	0.09	0

phases of annual and semi-annual cycles. To test for such differences we correlated India rain rate on region rain rate for lags ranging from minus three months to plus three months. Correlation coefficients for monthly rain rate are shown for Indian Ocean and its regions in Table 6.9. As

expected, India rain lags Bay of Bengal and Arabian Sea rain. Confirming earlier indications, the lag for Arabian Sea (about one month) exceeds the lag for Bay of Bengal (less than one month).

Three surprises emerge. First, at neither one nor two nor three lags does Gan rain rate correlate more than weakly with India rain rate. Second, India lags Madagascar/Cocos by less than six months. Third, especially at lags of one two months, monthly rain rate for India tends to oppose monthly rain rate for Indian Ocean. The third surprise qualifies the relationship between India and Indian Ocean annual rain rates which we noted above. It indicates an intermittant see-saw in the rains of India and the Indian Ocean. As Ramesh Kumar and Prasad (1995) suggested, this see-saw could involve the India band.

If excursions of the India band modulate summer rainfall over India, we might expect δR of India to correlate negatively with δR of Arabian Sea/Bay of Bengal. In fact, India δR correlates positively with Arabian Sea/Bay of Bengal δR (Table 6.10). Indeed, the pattern of correlation coefficients indicates that anomalous rain over India lags anomalous rain over the Arabian Sea/Bay of Bengal. For the Arabian Sea the lag of anomalous India rain approaches a month. Excursions of the India band may influence India rain only on time scales smaller than a month.

TABLE 6.9. Correlation coefficients, in per cent, for 1979-1986 monthly rain rate: India series regressed on selected New Indian Ocean series at lags from minus three to plus three months.

Region		Lag *						
no.	name	-3	-2	-1	0	1	2	3
17	New Indian Ocean	26	32	8	-16	-34	-30	-14
18	Arabian Sea/Bay of Bengal	-3	51	79	74	46	22	2
4	Gan	6	11	-2	-9	3	19	27
19	Madagascar/Cocos	-31	-56	-65	-58	-40	-7	25
1	Arabian Sea	7	56	77	63	29	7	-8
2	Bay of Bengal	-12	40	70	74	55	34	11

*Negative lag value corresponds to India leading; positive lag value to India lagging.

TABLE 6.10. As for Table 6.9, except anomaly of 1979-1986 monthly rain rate.

Region		Lag *						
no.	name	-3	-2	-1	0	1	2	3
17	New Indian Ocean	-3	24	14	24	12	8	14
18	Arabian Sea/Bay of Bengal	-15	19	39	49	10	-1	14
4	Gan	-7	13	3	13	1	2	3
19	Madagascar/Cocos	7	19	2	6	14	11	13
1	Arabian Sea	-8	17	32	35	-4	-10	10
2	Bay of Bengal	-15	10	24	38	19	10	11

*Negative lag value corresponds to India leading; positive lag value to India lagging.
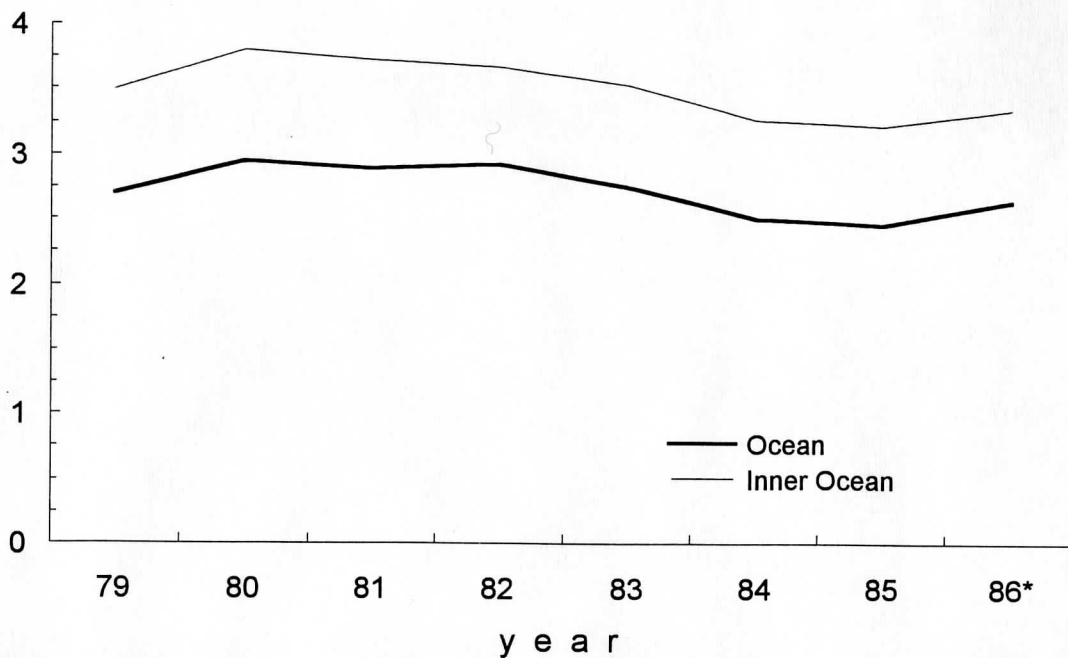
Fig. 6.1. Time series of annual rain rate for Ocean and Inner Ocean, in mm d^{-1}. For 1986, month by month 1979-1985 means were plugged into March, April and May slots.

$$y = -0.0039x + 2.917$$
$$r^2 = 0.1532$$
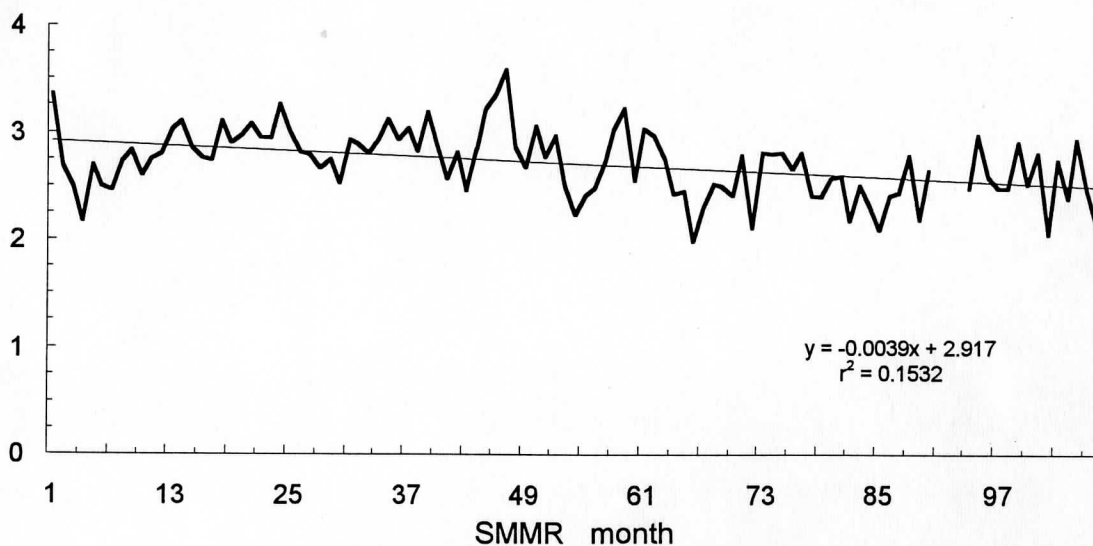
Fig. 6.2. Time series of monthly rain rate for Ocean; also, line of least-squares linear regression, Ocean rain rate on SMMR month. SMMR month begins with October 1978 and ends with August 1987. Rain rate in mm d^{-1}.
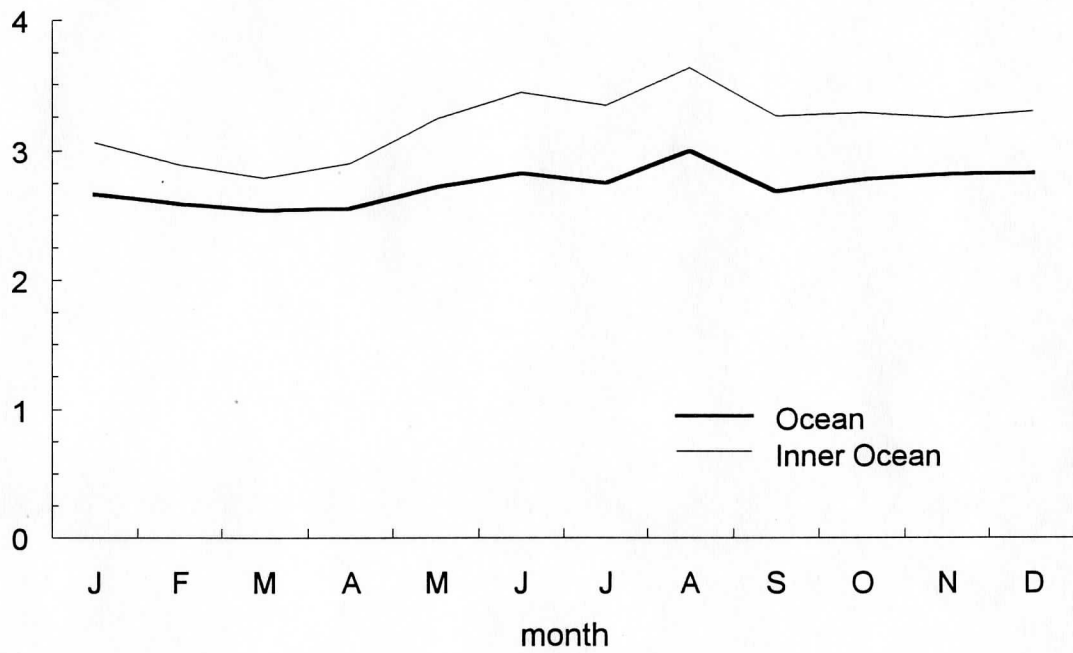
Fig. 6.3 Profiles of monthly mean rain rate for Ocean and Inner Ocean. Rain rate in mm d^{-1}.
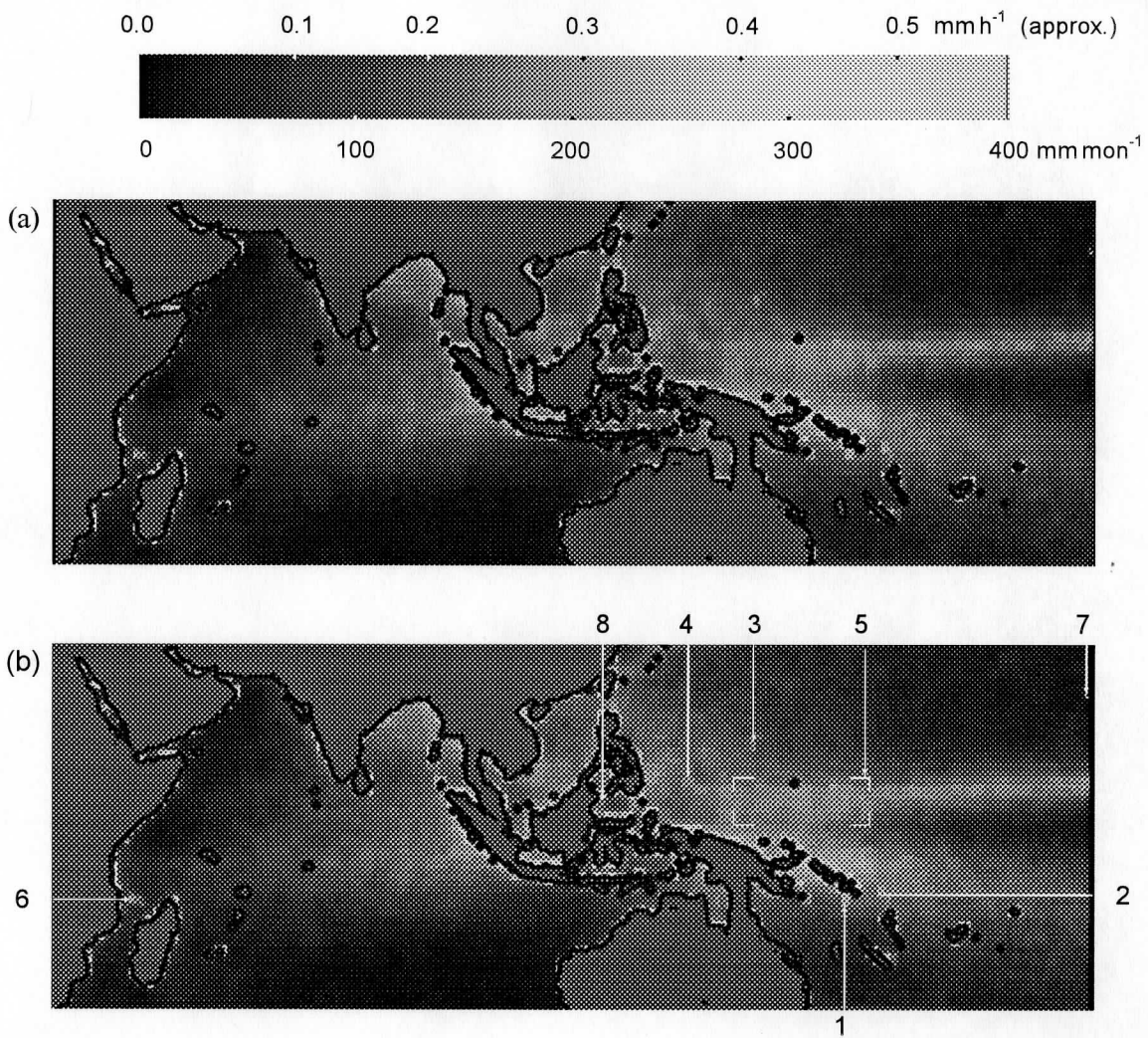
Fig. 6.4 (a) Grand average (1979–1986) rain rate from SMMR. (b) Island locations visible in SMMR data. Numerical designations are: (1) Rennel; (2) Santa Cruz Is.; (3) Guam; (4) Palau Is.; (5) Caroline Is.; (6) Comoro Is.; (7) Niihau; (8) Tawitawi.
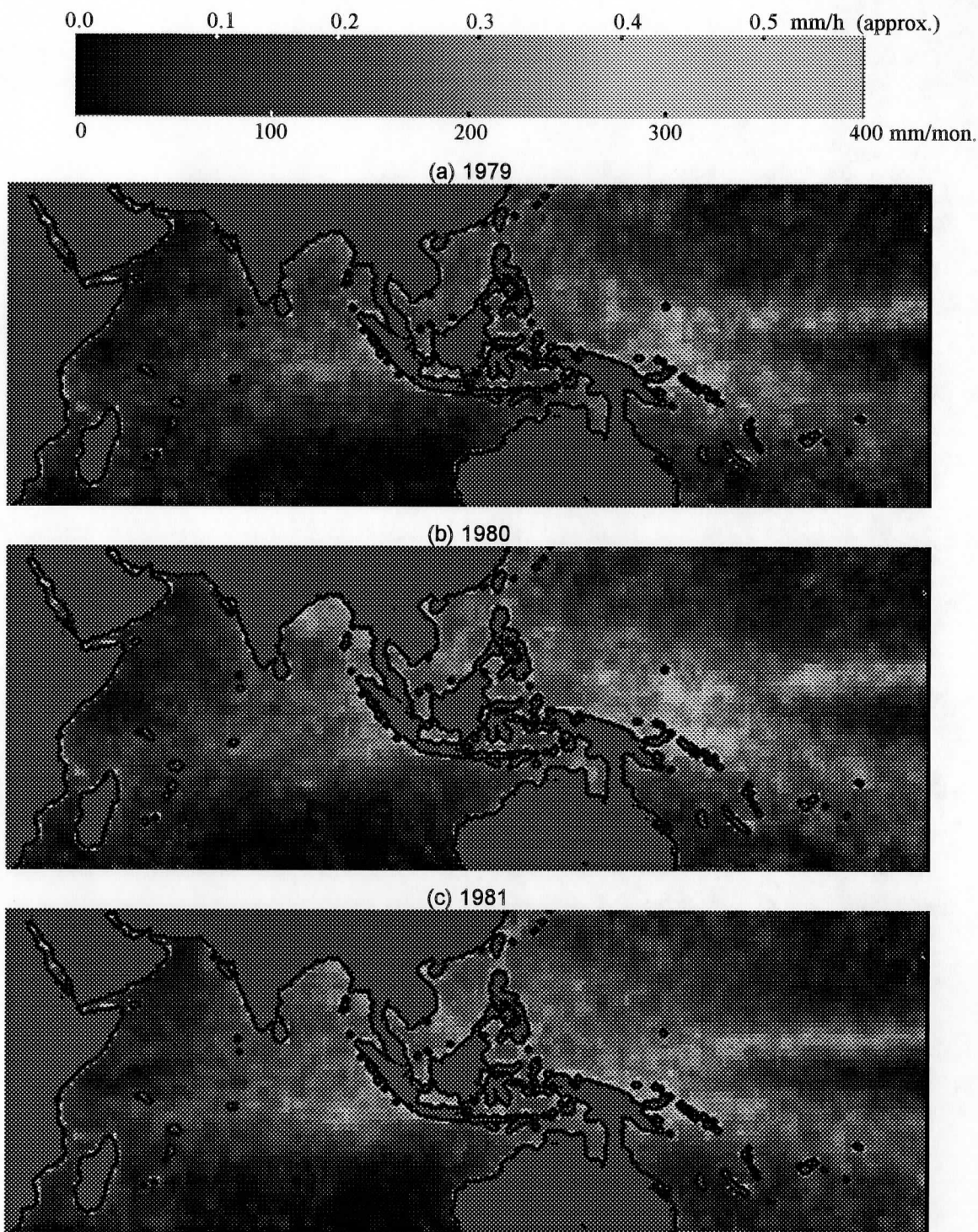
Fig. 6.5. Annual mean rain rate (mm d^{-1}). Since three months are missing for 1986, (h) estimates the annual mean by substituting mean monthly rainfall for the missing months, while (i) averages only the non-missing months.
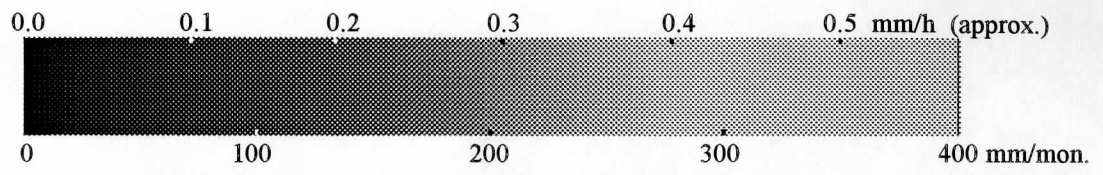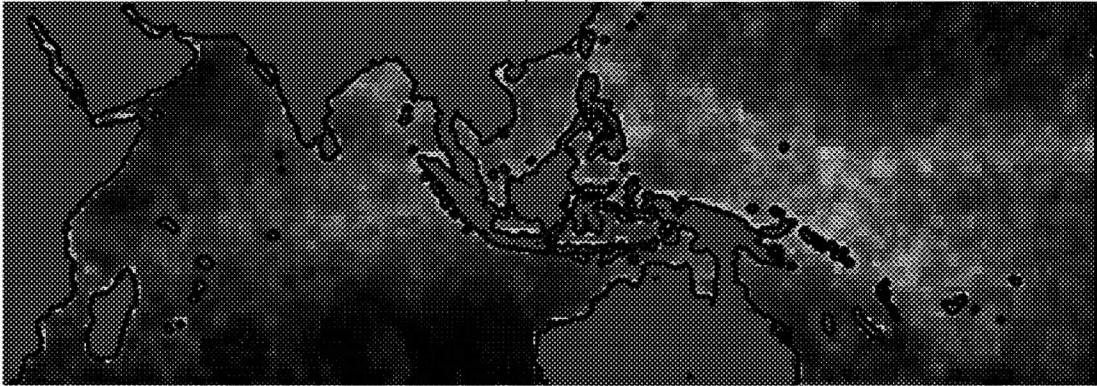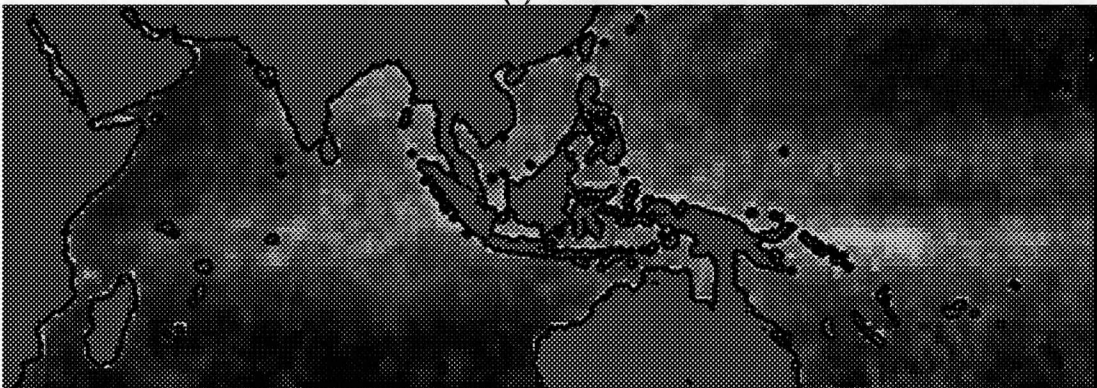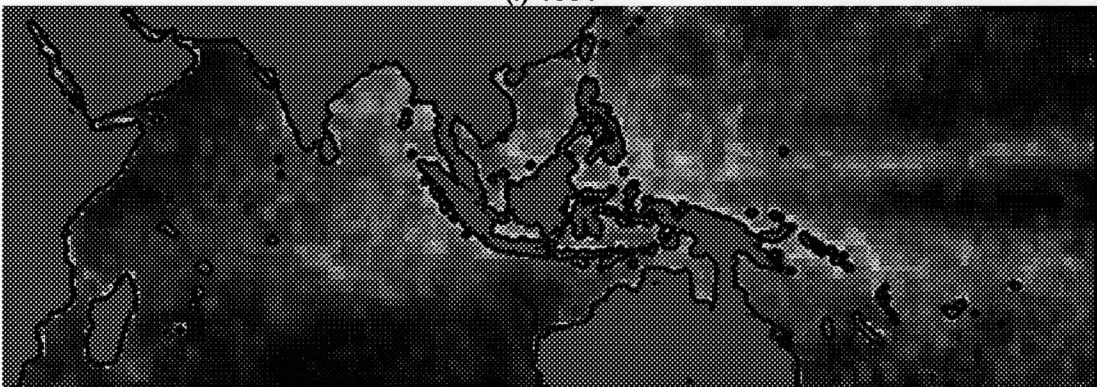
Fig. 6.5. (continued) Annual mean rain rate (mm d^{-1}).

0.0   0.1   0.2   0.3   0.4   0.5 mm/h (approx.)

0   100   200   300   400 mm/mon.
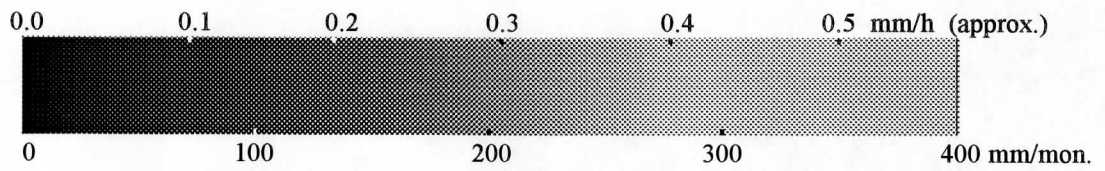
(g) 1985
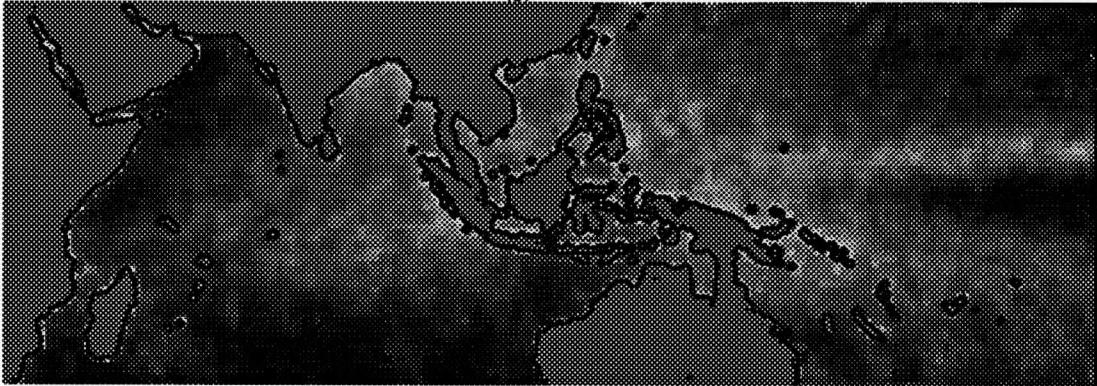
(h) 1986 (means substituted for missing months)
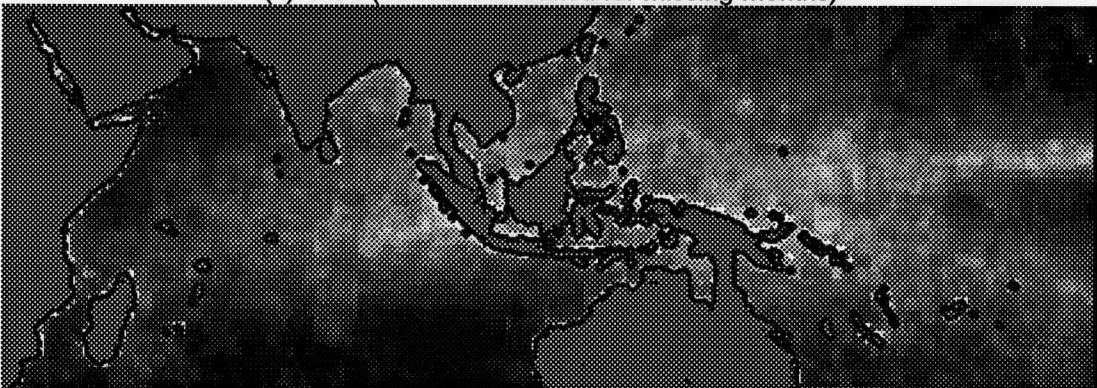
(i) 1986 (average of non-missing months only)
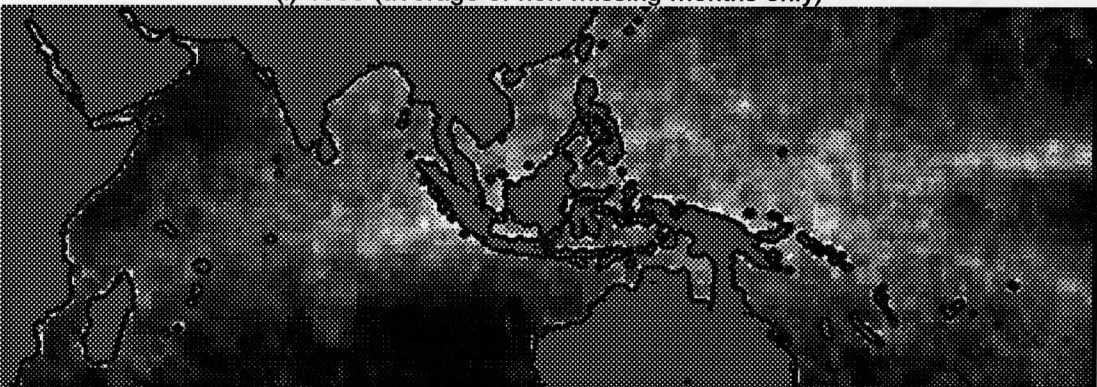
Fig. 6.5. (concluded) Annual mean rain rate (mm d^{-1}).
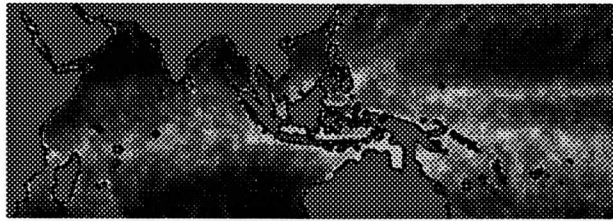
(a) January
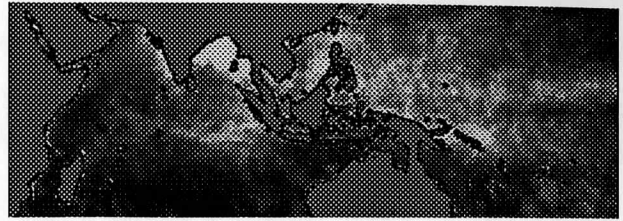
(g) July

(b) February
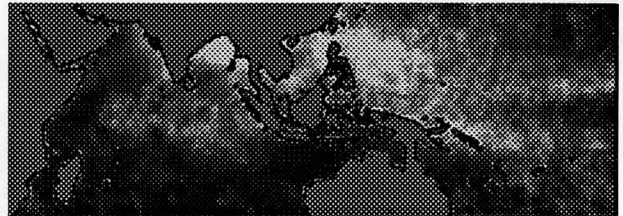
(h) August

(c) March
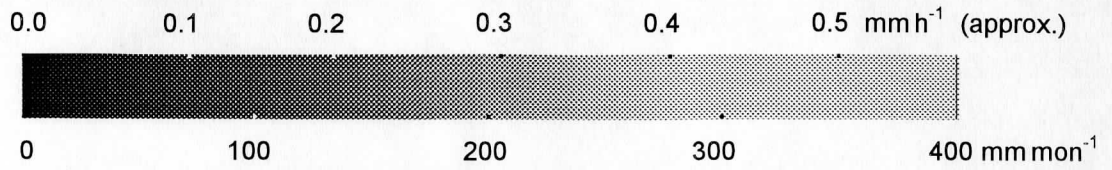
(i) September
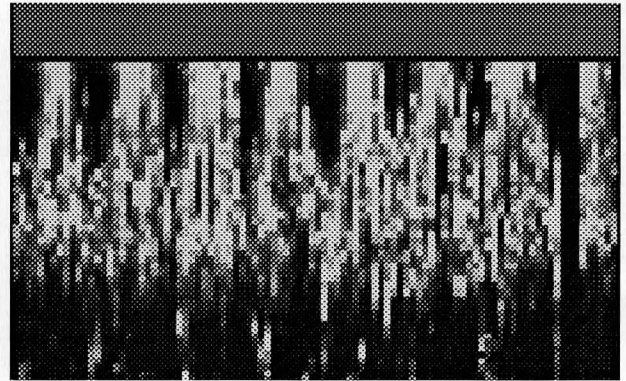
(d) April

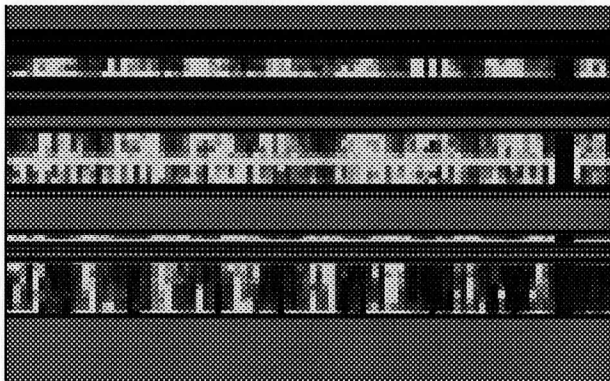(j) October

(e) May

(k) November

(f) June

(l) December

Fig. 6.6. Monthly mean rain.

0.0　　0.1　　0.2　　0.3　　0.4　　0.5　mm h^{-1} (approx.)
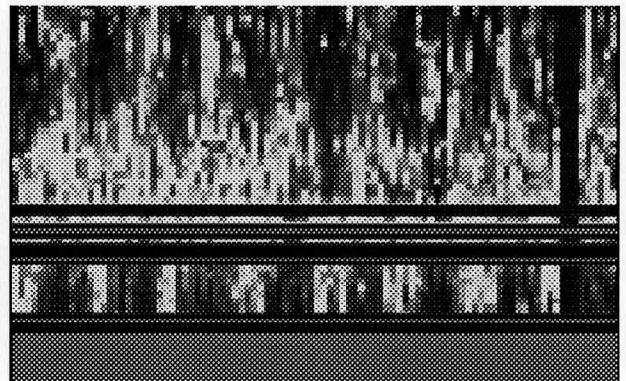
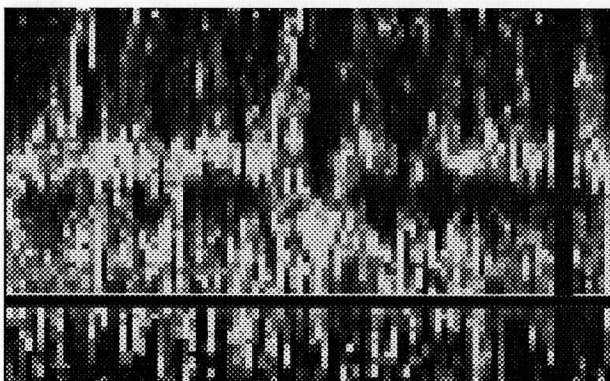0　　100　　200　　300　　400 mm mon^{-1}
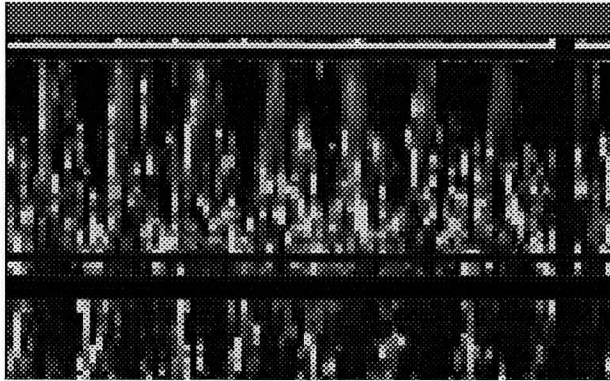
(a) 60°E Longitude

(b) 90°E Longitude

(c) 120°E Longitude
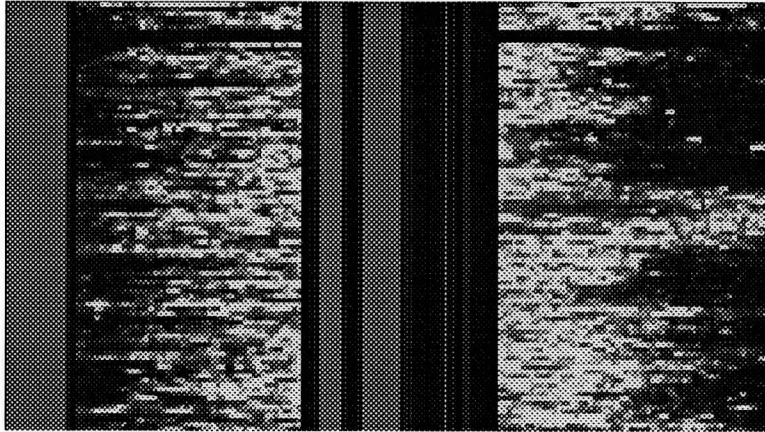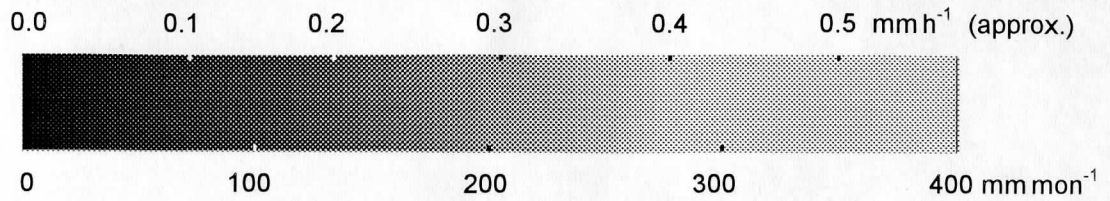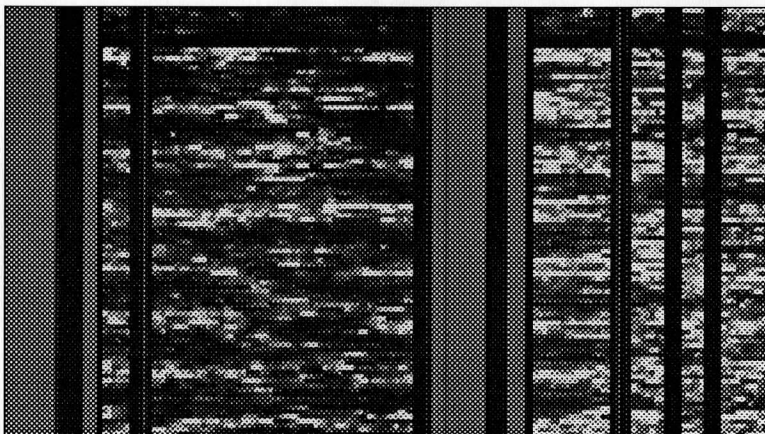
(d) 150°E Longitude

(e) 180°E Longitude

Fig. 6.7. Time latitude sections.

0.0   0.1   0.2   0.3   0.4   0.5 mm h⁻¹ (approx.)

0   100   200   300   400 mm mon⁻¹

(a) 0° Latitude

(b) 15° S Latitude
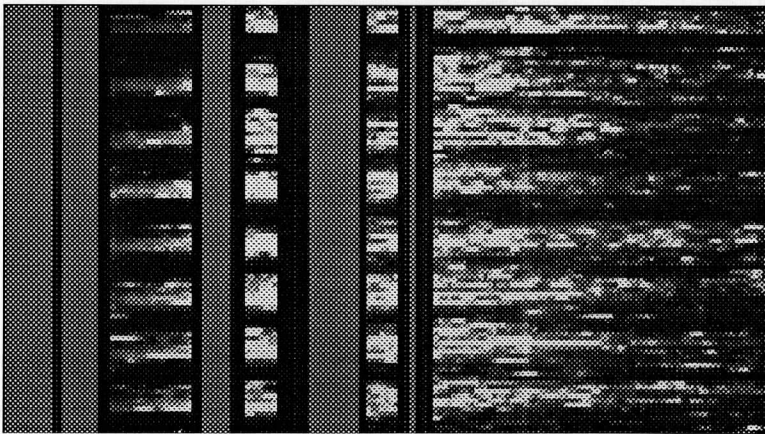
(c) 15° N Latitude

Fig. 6.8. Longitude sections.
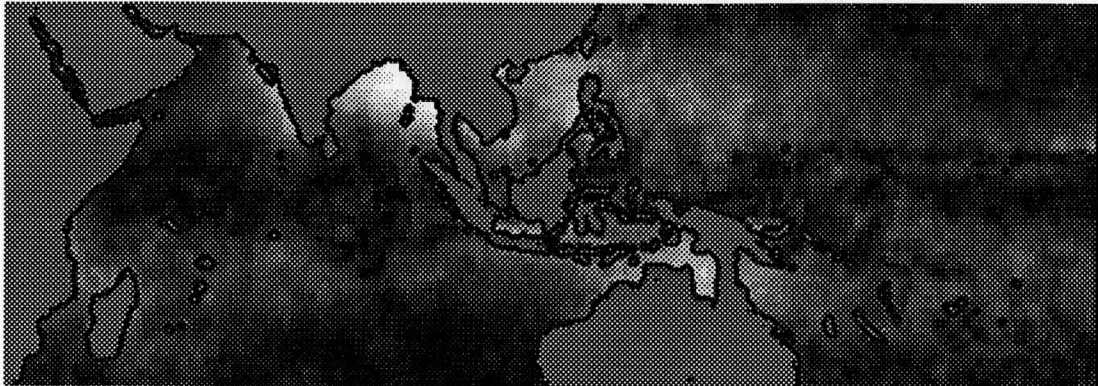
(a) Amplitude only
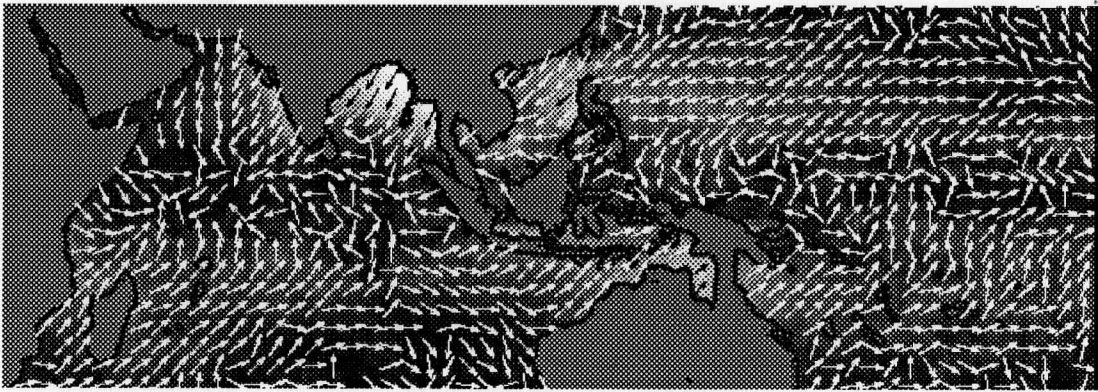
(b) Amplitude and phase

Fig. 6.9 Annual harmonic of the rainfall. In (b) arrows are shown for alternate rows and columns to prevent crowding. The gray scale is linear. Black to white covers the range 0 to 6.57 mm d^{-1} (0 to 200 mm mon^{-1}). No arrows are shown for amplitudes less than 0.164 mm d^{-1} (5.0 mm mon^{-1}).

Fig. 6.10 Schematic propagation paths of the annual harmonic.

(a) Amplitude only

(b) Amplitude and phase

Fig. 6.11. Semiannual harmonic of the rainfall. In (b) arrows are shown for every third row and column to prevent crowding. The gray scale is linear. Black to white covers the range 0 to 6.57 mm d^{-1} (0 to 200 mm mon^{-1}). No arrows are shown where amplitudes are less than 0.164 mm d^{-1} (5.0 mm mon^{-1}).
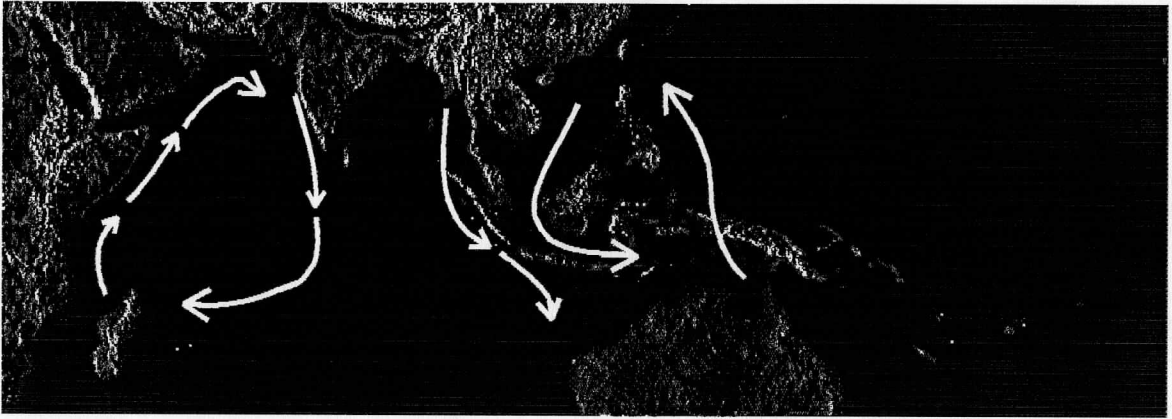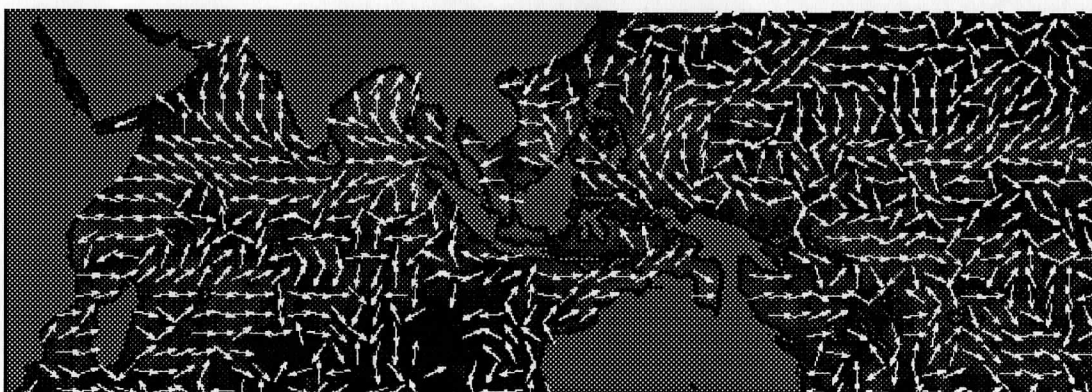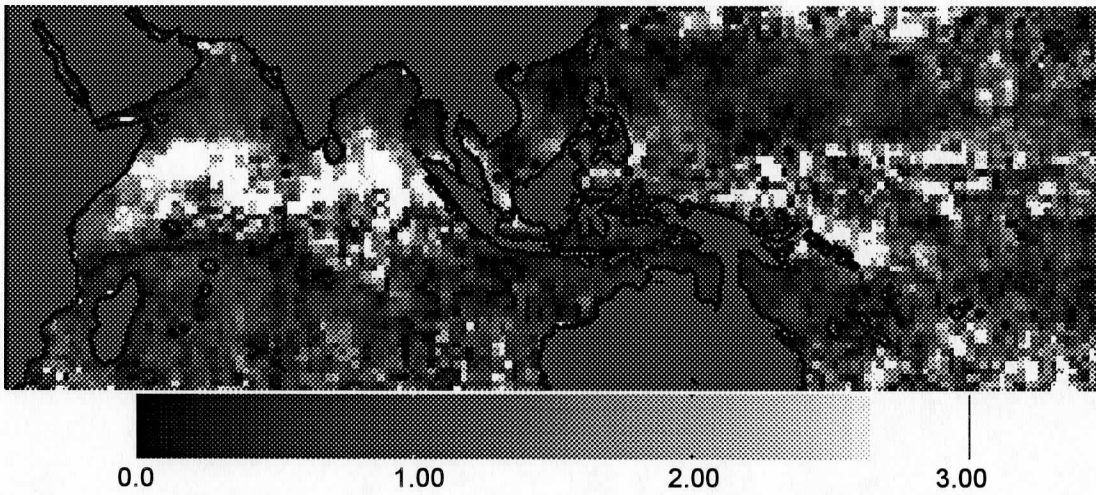
Fig. 6.12 Importance of the second harmonic relative to the first. The actual quantity displayed is $C_2/(5 + C_1)$ in order to stabilize against division by very small C_1.
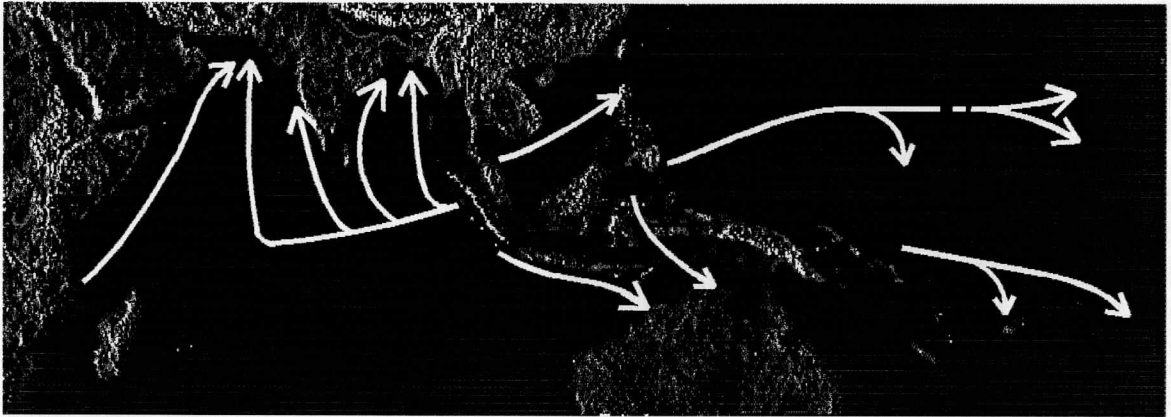
Fig. 6.13 Schematic propagation paths of the semiannual harmonic.

7. CONCLUSION

Applying a generalized version of the Wisconsin rain retrieval scheme to the set of Pathfinder Nimbus-7 SMMR brightness temperatures, we have generated an eight-year mapping of monthly, one-degree-by-one-degree rain rate over the Indian and West Pacific Oceans. Guided by a monsoon-oriented review of rain structure and behavior in the Indo-Pacific region, we analyzed large-scale features contained in this mapping. The analysis includes statistics, profiles and maps. In particular, it addresses annual and semi-annual cycles, interhemispheric oscillations and the 1982-1983 El Niño/Southern Oscillation. Using gauge rainfall from India, it also considers the link between ocean and continental components of the Asian monsoon.

Except for gale-force winds, the scheme adequately represents ambient conditions over the Indian and West Pacific Oceans. Its estimates of rain rate conform with some observations of Indian and Pacific Ocean rain rate. Evidently, little could be gained from the Nimbus-7 SMMR record at a space-time scale less than that of the present analysis.

Except for three months in 1986, at one-degree-by-one-degree spatial resolution and one-month temporal resolution nearly everywhere in the monsoon domain and nearly continuously from 1979 through 1986 the Pathfinder set of SMMR radiances provided adequate numbers of brightness temperatures. We found no evidence of poor calibration at any of the three frequencies the algorithm uses. Neither did we find evidence of drift in the calibrations of any of these channels. In both absolute and relative senses, the Pathfinder set consistently located brightness temperatures for the three channels to within the dimensions of the 37 GHz footpring. Swath format in the presentation of the data enabled us to bypass an expensive mapping step in the old process. Compared with the pre-Pathfinder 6250 round tapes, eight-millimeter format in the recording of the data saved space equal to two bookcases.

We found two main elements—bands and waves—in the maritime component of monsoon rain. Through the lifetime of the Nimbus-7 SMMR rain tended to fall in two bands paired across the equator. Across the Indian Ocean, in persistence and strength the southern member consistently dominated the northern member. Across the West Pacific Ocean, the southern member occasionally dominated the northern member. Close to the East Indies northern and southern members merged. Across the embayments of southern Asia a third band paralleled the northern member of the equatorial pair.

Waves followed the sun. Northbound, a wave crossed the equator in the boreal spring; southbound, in the boreal autumn. Following each crossing, it amplified—strongly in the northern hemisphere and weakly in the southern hemisphere. Toward the peak of its excursion into each hemisphere, a wave damped—weakly in the northern hemisphere and strongly in the northern hemisphere.

A major wave occupied waters within and near the East Indies. The East Indies wave tended to inscribe a counter-clockwise loop elongated from northwest to southeast. A minor wave occupied the Indian Ocean. Northbound, after crossing the equator, the Indian Ocean wave strengthened more than the East Indies wave; southbound, less. Through the course of a year the

Indian Ocean wave tended to inscribe a clockwise loop elongated from northeast to southwest. In the boreal summer and autumn it merged with the East Indies wave over the Indian Ocean west of Sumatra and near the Malay Peninsula.

Waves modulated bands. As a wave approached, a band tended to join it and amplify; as the wave receded, the band tended to follow it and weaken. Operating near the limit of this tendency, the Indian Ocean wave became the third band. The interaction of waves and bands yielded zones dominated by an annual cycle, zones dominated by a semi-annual cycle and zones absent either. The annual cycle prevailed along the third band and on the poleward flanks of the members of the equatorial pair of bands. The semi-annual cycle prevailed along the equatorward flanks of members of the equatorial pair. Both cycles disappeared close to the axes of members of the equatorial pair of bands in the eastern Indian Ocean, the southwestern Pacific Ocean and north-central Pacific Ocean.

The records reveal an event. This event occurred in two stages, involved the Indian Ocean as well as the West Pacific Ocean and reflected the westernmost part of the 1982-1984 El Niño/Southern Oscillation. In the first stage anomalously light rain fell over the Indian Ocean; anomalously heavy rain fell over the West Pacific Ocean. In the second stage this dipole pattern reversed sign. Across the West Pacific Ocean the second stage began abruptly. It initiated a second dipole pattern, extreme deficiency in the north member of the equatorial pair of rain bands and little or no deficiency in the south member.

Rain over India conforms to the band-wave model of monsoon ocean rainfall. The match in phase and amplitude between Indian Ocean rain and India rain suggests a correspondence between the northbound, amplifying Indian Ocean wave and the onset of the southwest monsoon. Averaged over a month as well as a year, Arabian Sea and Bay of Bengal rain rate varies with rather than against rain rate over India. For periods up to a month anomalous rain rate over the Arabian Sea may predict anomalous rain rate over India.

Although it overestimates rainfall over the Indian and West Pacific Oceans, Jaeger's 1976 atlas captures most of the major features and many of the secondary features of the present mapping. The zonal bands which MHA found in an analysis of three years of SMMR observations of the Indian Ocean appear also. The present climatology departs from previous climatologies (including that of MHA) in suggesting less gradient along parallels and more symmetry across the equator. In essential respects the present mapping conforms to the elements of Meehl's (1987) portrait of the annual cycle in monsoon rainfall from southeast Asia to north Australia and Micronesia. However, it indicates a looping rather than an oscillating path for the convective maximum. It also points to a second cross-equatorial monsoon dipole, which connects southeast Asia with Mascarene waters of the Indian Ocean.

We recommend that the Wisconsin scheme be validated against gauge measurements of rain rate. Validation could be accomplished as HOMA validated the old scheme or as Spencer (1993) or Morrissey et al. (1993) validated other schemes. To improve its performance over the Arabian Sea we recommend that the scheme be extended to accomodate gale-force winds; to generalize it to all tropical oceans through all phases of an ENSO cycle we also recommend that

the scheme be extended to accomodate cool sea surface temperatures under a shallow trade-wind inversion.

Our analyses scratch the surface of the 106-month Nimbus-7 SMMR rain record. By itself the record would support analyses of the following issues:

- significance of the semi-annual cycle;
- the existence of a biennial cycle (Meehl 1987; Rasmusson et al. 1990);
- the effect of Madden-Julian waves (Madden and Julian 1972; Hong and Lim 1994) on the onset of the southwest monsoon;
- band-scale behavior of the 1982-1984 ENSO; and
- a test of the degree to which the band-wave concept explains over-water structure and variation in the Asian-Mascarene-Australian monsoon.

Extended across the Pacific Ocean and into the Atlantic Ocean the Nimbus-7 SMMR record could yield a portrait of over-water rain in each of the earth's monsoon systems. Complemented by records of rain over Asia, Australia, Madagascar, Melanesia and the East Indies it could yield the first comprehensive view of rain in the greater Austral-Asian-Mascarene monsoon system. Spliced to the Microwave Sounding Unit record of Spencer (1993), to one of the Special Sensor Microwave/Imager records (e.g., Chang et al. 1993) or merged with to the rain record of the Global Precipitation Climatology Project (Arkin and Xie 1994), the SMMR record could address issues involving multiple ENSOs and singularities and trends in tropical rainfall.

REFERENCES

Arkin, P. A., and P. Xie, 1994: The Global Precipitation Climatology Project: First Algorithm Intercomparison Project. *Bull. Amer. Meteorol. Soc.*, **75**, 401-419.

Chang, A. T. C., L. S. Chiu and T. T. Wilheit, 1993: Oceanic monthly rainfall derived from SSM/I. *Eos*, **74 (No. 44)**, 505, 513.

Dorman, C. E., 1982: Indian Ocean Rainfall. *Trop. Ocean-Atmos. Newslett.*, **10**, 4.

Findlater, J., 1969: A major low-level air current near the Indian Ocean during the northern summer. *Quart. J. Roy. Meteor. Soc.*, **95**, 362-380.

Garcia, O., 1981: A comparison of two satellite rainfall estimates for GATE. *J. Appl. Meteorol.*, **20**, 430-438.

——-, 1985: *Atlas of Highly Reflective Clouds for the Global Tropics: 1971-1983*. U. S. Department of Commerce, Washington, D.C., xii, 365 pp.

Geiger, R. 1965: *The Earth's Atmosphere: Mean Annual Precipitation*. World Maps, Map 5, Scale 1:30 M. Justus Perthes.

Gloersen, P., and F. T. Barath, 1977: A scanning multichannel microwave radiometer for Nimbus-G and Seasat-A. *IEEE J. Oceanic Eng.*, **OE-2**, 172-178.

Gloersen, P., and L. Hardis, 1978: The Scanning Multichannel Microwave Radiometer (SMMR) experiment. In *The Nimbus 7 Users' Guide*, Madrid, C. R., Ed., NASA Goddard Space Flight Center, Greenbelt, MD, 213-245.

Gloersen, P., W. J. Campbell, D. J. Cavalieri, J. C. Comiso, C. L. Parkinson and H. J. Zwally, 1992: *Arctic and Antarctic Sea Ice, 1978-1987: Satellite Passive-Microwave Observations and Analysis*. Vol. NASA SP-511, Scientific and Technical Information Program, National Aeronautics and Space Administration, Washington, DC, 290 pp.

Grassotti, C., and L. Garand, 1994: Classification-based rainfall estimation using satellite data and numerical forecast model fields. *J. Appl. Meteorol.*, **33**, 159-179.

Graves, C. E., 1993: A model for the beam-filling effect associated with the microwave retrieval of rain. *J Atmos. Ocean. Technol.*, **10**, 5-14.

Hartmann, D. L., and M. L. Michelsen, 1989: Intraseasonal periodicities in Indian rainfall. *J. Atmos. Sci.*, **46**, 2838-2862.

Hastenrath, S., and P. J. Lamb, 1979: *Climatic Atlas of the Indian Ocean. Part I: Surface Climate and Atmospheric Circulation.* The University of Wisconsin Press, Madison, Wisconsin, xix pp plus 97 charts.

Hinton, B. B., W. S. Olson, D. W. Martin and B. Auvine, 1992: A passive microwave algorithm for tropical oceanic rainfall. *J. Appl. Meteorol.*, **31**, 1379-1395.

Hong, Y., and H.-S. Lim, 1994: Evidence for low-frequency waves of tropical rainfall inferred from microwave brightness temperature. *Mon. Wea. Rev.*, **122**, 1364-1370.

Jaeger, L., 1976: *Monatskarten des Niederschlags für die ganze Erde.* Im Selbstverlag des Deutschen Wetterdienstes, Offenbach, Germany.

Kessler, A., 1968: Globalbilanzen von Klimaelementen. *Ber. Inst. Meteorol. Klimatolg. Tech. Hochschule Hanover*, **3**, 1-141.

Kilonsky, B. J., and C. S. Ramage, 1976: A technique for estimating tropical open-ocean rainfall from satellite observations. *J. Appl. Meteorol.*, **15**, 972-975.

Knutson, T. R., K. M. Weickmann and J. E. Kutzbach, 1986: Global-scale intraseasonal oscillations of outgoing longwave radiation and 250 mb zonal wind during Northern Hemisphere summer. *Mon. Wea. Rev.*, **114**, 605-623.

Lau, K. M., and P. H. Chan, 1986: The 40-50 day oscillation and the El Niño/Southern Oscillation: A new perspective. *Bull. Amer. Meteorol. Soc.*, **67**, 533-534.

Lau, K. M., and L. Peng, 1990: Origin of low-frequency (intraseasonal) oscillations in the tropical atmosphere. Part III: Monsoon dynamics. *J. Atmos. Sci.*, **47**, 1443-1462.

Lau, K.-M., and P. J. Sheu, 1988: Annual cycle, quasi-biennial oscillation, and Southern Oscillation in global precipitation. *J. Geophys. Res.*, **93 (No. D9)**, 10,975-10,988.

Legates, D. R., and C. J. Willmott, 1990: Mean seasonal and spatial variability in gauge-corrected, global precipitation. *Int. J. Climatol.*, **10**, 111-127.

Madden, R. A., 1986: Seasonal variation of the 40-50 day oscillation in the tropics. *J. Atmos. Sci.*, **43**, 3138-3158.

Madden, R. A., and P. R. Julian, 1972: Description of global-scale circulation cells in the tropics with a 40-50 day period. *J. Atmos. Sci.*, **29**, 1109-1123.

Martin, D. W., B. B. Hinton and B. A. Auvine, 1993: Three years of rainfall over the Indian Ocean. *Bull. Amer. Meteorol. Soc.*, **74**, 581-590.

Meehl, G. A., 1987: The annual cycle and interannual variability in the tropical Pacific and Indian Ocean regions. *Mon. Wea. Rev.*, **115**, 27-50.

Mooley, D. A., and J. Shukla, 1987: Variability and forecasting of the summer monsoon rainfall over India. In *Monsoon Meteorology*, Chang, C. P. and T. N. Krishnamurti, Eds., Oxford University Press, New York, 26-59.

Morrissey, M. L., and W. F. Krajewski, 1993: A point process model for tropical rainfall. *J. Geophys. Res.*, **98**, 16639-16652.

Njoku, E. G., and B. Rague 1995: *NASA Pathfinder Nimbus-7 Scanning Multichannel Microwave Radiometer (SMMR) Brightness Temperature (Level 1B) Dataset*. Pathfinder Data Set Document published by Jet Propulsion Laboratory (Pasadena, CA) for use of the Marshall Space Flight Center Distributed Active Archive Center (Huntsville, AL).

Njoku, E. G., J. M. Stacey and F. T. Barath, 1980: The Seasat Scanning Multichannel Microwave Radiometer (SMMR): Instrument description and performance. *IEEE J. Oceanic Eng.*, **OE-5**, 100-115.

Njoku, E. G., B. Rague and K. Fleming, 1994: *Nimbus-7 Scanning Multichannel Microwave Radiometer (SMMR) Brightness Temperature Data*. Jet Propulsion Laboratory, Pasadena, California, 7 pp plus appendix.

Olson, W. S., 1987: *Estimation of rainfall rates in tropical cyclones by passive microwave radiometry*. Dissertation, University of Wisconsin-Madison (Madison), 282 pp.

Parthasarathy, B., K. Rupa Kumar and D. R. Kothawale, 1992: Indian summer monsoon rainfall indices: 1871-1990. *Meteor. Mag.*, **121**, 174-186.

Petty, G. W., 1995: Frequencies and characteristics of global oceanic precipitation from shipboard present-weather reports. *Bull. Amer. Meteorol. Soc.*, **76**, 1593-1616.

Prabhakara, C., D. A. Short, W. Wiscombe, R. S. Fraser and B. E. Vollmer, 1986: Rainfall over oceans inferred from Nimbus 7 SMMR: Application to 1982-83 El Nino. *J. Climate Appl. Meteor.*, **25**, 1464-1474.

Ramage, C. S., 1971: *Monsoon Meteorology*. Academic Press, New York, 296 pp.

——, 1995: *Forecasters Guide to Tropical Meteorology—AWS TR 240 Updated*. Air Weather Service, Scott Air Force Base, Illinois, xxxvii, 392, 5 appendices.

Ramesh Kumar, M. R., and T. G. Prasad, 1995: *An Atlas of Precipitation over the Tropical Indian Ocean Using Satellite Data*. National Institute of Oceanography, Dona-Paula, Goa, India, 20 pp, 38 figures.

Rao, M. S. V., W. V. I. I. I. Abbott and J. S. Theon, 1976: *Satellite-Derived Global Oceanic Rainfall Atlas (1973 and 1974)*. National Aeronautics and Space Administration, Washington, DC, 31 pp plus appendices.

Rasmusson, E. M., X. Wang and C. F. Ropelewski, 1990: The biennial component of ENSO variability. *J. Marine Systems*, **1**, 71-96.

Rex, D. F., and H. E. Landsberg, Eds., 1969: *World Survey of Climatology*. Elsevier, New York.

Spencer, R. W., 1993: Global oceanic precipitation from the MSU during 1979-91 and comparisons to other climatologies. *J. Climate*, **6**, 1301-1326.

Waliser, D. E., and C. Gautier, 1993: A satellite-derived climatology of the ITCZ. *J. Climate*, **6**, 2162-2174.

Waliser, D. E., N. E. Graham and C. Gautier, 1993: Comparison of the Highly Reflective Cloud and Outgoing Longwave Radiation datasets for use in estimating tropical deep convection. *J. Climate*, **6**, 331-353.

Wang, B., 1994: Climatic regimes of tropical convection and rainfall. *J. Climate*, **7**, 1109-1118.

Weickmann, K. M., G. R. Lussky and J. E. Kutzbach, 1985: Intraseasonal (30-60 day) fluctuations of outgoing longwave radiation and 250 mb streamfunction during northern winter. *Mon. Wea. Rev.*, **113**, 941-961.

Yasunari, T., 1991: The monsoon year—a new concept of the climatic year in the tropics. *Bull. Amer. Meteorol. Soc.*, **72**, 1331-1338.

APPENDIX A
TABLES, RELATIONS, AND ENVIRONMENTAL DATA
FOR CALCULATING RAIN RATES AND WEIGHTS

A.1 Rain Rates

In this Appendix, like Sec. 4, we are interested in the rain rates for a single realization of the data rather than monthly mean rain rates. Consequently, as noted in the table headings, rain rates are given in mm h^{-1}, rather than mm d^{-1} or mm mon^{-1}.

Table A.1 lists the values of the parameters introduced in (4.8), (4.9), and Sec. 4.3. The purpose of Table A.2 is to describe the useful ranges of rain rates and brightness temperatures for each channel when scattering is not important.

TABLE A.1. Basic state rain rate, R_{0i}, when scattering is not important.

Channel Index i	Channel frequency GHz	Channel polar- ization	T_{B0i} (K)	A_{0i} (K)	D_{0i} (mm h^{-1})	Square of the correlation[1]	Max. rate in regression (mm h^{-1})
1	6.6	H	89.198	134.664	26.662	> 0.999	64
2	6.6	V	160.825	94.577	38.513	> 0.998	64
3	10.7	H	99.515	122.498	8.736	> 0.999	64
4	10.7	V	169.445	73.807	8.6189	> 0.999	64
5	18	H	139.572	91.233	3.788	> 0.999	16
6	18	V	196.751	52.176	3.607	> 0.999	16
7	21	H	191.437	52.323	2.899	> 0.998	11.31
8	21	V	229.665	26.197	2.613	> 0.998	11.31
9	37	H	164.863	76.069	0.513	> 0.998	5.65
10	37	V	243.578	12.528	0.4781	> 0.999	2.83
11	37	V-H	34.997	-22.545	1.308	> 0.999	8

Updated 27 July, 1995

---

[1] This is a measure of how well the expressions of the form of (9) fit the model data whose original form was numerical values at a set of discrete rain rates.

TABLE A.2. $T_{Bi}^{(2)}$ and $T_{Bi}^{(3)}$ and corresponding rain rates $2D_0$ and $3D_0$.

Chan.	i	$T_i^{(2)}$ K	$2D_0$ mmh^{-1}	$T_i^{(3)}$ K	$3D_0$ mmh^{-1}
H66	1	221.159	75.260	234.171	112.890
V66	2	244.773	83.984	253.031	125.976
H10	3	205.435	17.472	215.914	26.208
V10	4	233.262	17.238	239.576	25.857
H18	5	218.458	7.576	226.263	11.364
V18	6	241.866	7.214	246.329	10.821
H21	7	236.679	5.798	241.155	8.697
V21	8	252.317	5.226	254.558	7.839
H37	9	230.637	1.026	237.145	1.539
V37	10	254.411	0.956	255.482	1.434
D37	11	15.503	2.616	13.574	3.924

TABLE A.3. Coefficients for calculating rain rate when scattering is important.

Channel	i	b_{0i}	b_{1i}	b_{2i}
H37	9	78.1500	-93.4857	23.9734
V37	10	15.1726	-11.2723	0.8333
D37	11	125.258	-131.8115	17.494

A.2 Partial Derivatives

The expressions which will be given below for the partial derivatives appearing in (1) make use of the T_{B0i} and the A_{0i} listed in Table A.1. In addition, it is convenient to have a scale factor for each individual derivative. Each derivative can thus be expressed as a simple polynomial having (for most of the channels and for rain rates up to about $2 \cdot D_{0i}$.) coefficients the order of 0.01 to 1 multiplying a scaled brightness temperature variable smaller than one in magnitude. These derivative scale factors, S_{ij} are listed in Table A.4 below.

Recall that for all the channels (indexed by i) the scaled brightness temperature variable, τ_i , was defined as:

$$\tau_i = \frac{T_{Bi} - T_{B0i}}{A_{0i}}$$

Under normal circumstances, τ_i does not exceed 1 by more than a small fraction. Increments above unity are due to noise and departures of actual environmental conditions from the reference state conditions. For simplicity, we will replace the mathematical partial derivatives of (4.1) with a more "numerical" notation, $d_{ij}(\tau_i)$. Specifically the list of replacements is:

$$\frac{\partial R_i}{\partial (SST)}, \frac{\partial R_i}{\partial (RH)}, \frac{\partial R_i}{\partial (Z_{fr})}, \frac{\partial R_i}{\partial (W)}, \frac{\partial^2 R_i}{\partial (W)^2} \rightarrow d_{i1}, d_{i2}, d_{i3}, d_{i4}, d_{i5}, \qquad (A.1)$$

This means the correspondence between the j-index and the variables is intended to match that used in Table A.2. For all ij pairs,

$$d_{ij}(\tau_i) = \begin{cases} -S_{ij} \cdot \left(c_{ij0} + c_{ij1} \cdot \tau_i + c_{ij2} \tau_i^2 \right) & \tau \geq 0 \\ -S_{ij} \cdot c_{ij0} & \tau < 0 \end{cases} \qquad (A.2)$$

The numerical values of these coefficients c_{ijk} ($k = 0, 1, 2$) are given in Table A.5. However, it turns out that $d_{i5}(\tau_i)$ is always equal to a constant m_i times $d_{i4}(\tau_i)$. That constant is in the scale factors of Table A.2, so the $j = 5$ rows of Table A.5a-c. are all equal to the $j = 4$ rows.

TABLE A.4. Derivative scale factors, S_{ij}

Channel.	SST (C) ($j = 1$)	RH (%) ($j = 2$)	Z_{fr} (km) ($j = 3$)	W (m·s⁻¹) ($j = 4$)	2nd W (m²·s⁻¹) ($j = 5$)
H66 ($i = 1$)	$+6.996 \cdot 10^{-2}$	$+4.410 \cdot 10^{-3}$	$+2.739 \cdot 10^{-1}$	$+1.598 \cdot 10^{-1}$	$+4.424 \cdot 10^{-2}$
V66 ($i = 2$)	$+3.046 \cdot 10^{-1}$	$+6.518 \cdot 10^{-3}$	$+4.671 \cdot 10^{-1}$	$+1.402 \cdot 10^{-1}$	$+5.607 \cdot 10^{-2}$
H10 ($i = 3$)	$+3.086 \cdot 10^{-2}$	$+4.978 \cdot 10^{-3}$	$+2.583 \cdot 10^{-1}$	$+9.110 \cdot 10^{-2}$	$+2.654 \cdot 10^{-2}$
V10 ($i = 4$)	$+8.263 \cdot 10^{-2}$	$+5.324 \cdot 10^{-3}$	$+3.400 \cdot 10^{-1}$	$+5.546 \cdot 10^{-2}$	$+2.190 \cdot 10^{-2}$
H18 ($i = 5$)	$+1.387 \cdot 10^{-2}$	$+1.715 \cdot 10^{-2}$	$+2.910 \cdot 10^{-1}$	$+7.542 \cdot 10^{-2}$	$+1.899 \cdot 10^{-2}$
V18 ($i = 6$)	$+4.344 \cdot 10^{-2}$	$+1.849 \cdot 10^{-2}$	$+4.576 \cdot 10^{-1}$	$+4.821 \cdot 10^{-2}$	$+1.913 \cdot 10^{-2}$
H21 ($i = 7$)	$+1.735 \cdot 10^{-2}$	$+5.581 \cdot 10^{-2}$	$+5.763 \cdot 10^{-1}$	$+8.442 \cdot 10^{-2}$	$+2.050 \cdot 10^{-2}$
V21 ($i = 8$)	$+5.127 \cdot 10^{-2}$	$+6.472 \cdot 10^{-2}$	$+6.006 \cdot 10^{-1}$	$+5.157 \cdot 10^{-2}$	$+1.914 \cdot 10^{-2}$
H37 ($i = 9$)	$+6.492 \cdot 10^{-3}$	$+2.068 \cdot 10^{-2}$	$+1.069$	$+1.027 \cdot 10^{-1}$	$+1.745 \cdot 10^{-2}$
V37 ($i = 10$)	$+9.010 \cdot 10^{-2}$	$+6.147 \cdot 10^{-2}$	$+2.742$	$+1.378 \cdot 10^{-1}$	$+4.606 \cdot 10^{-2}$
D37 ($i = 11$)	$+1.395 \cdot 10^{-2}$	$-1.058 \cdot 10^{-2}$	$-6.490 \cdot 10^{-1}$	$-9.372 \cdot 10^{-2}$	$-1.031 \cdot 10^{-2}$

TABLE A.5a. Values of c_{ijk} for calculating partial derivatives as functions of the scaled brightness temperatures τ_i for the frequencies below 37 GHz.

i	j	$k = 0$	1	2
1 (H6.6)	1 (*SST*)	.996838	.302019	1.808837
	2 (*RH*)	.998653	.23809	1.128755
	3 (*Z$_{fr}$*)	0	0	0
	4 (*W*)	.9972923	.267712	1.079087
	5 (2nd *W*)	.9972923	.267712	1.079087
2 (V6.6)	1	1.027	-.985114	2.429049
	2	1.031597	-1.186886	2.106368
	3	0	0	0
	4	1.031158	-1.167141	2.153662
	5	1.38659	-1.167141	2.153662
3 (H10)	1	1.028099	-.885217	2.799784
	2	1.024276	-.732805	2.249252
	3	0	6.33	0
	4	1.030325	-.808671	2.329464
	5	1.030325	-.808671	2.329464
4 (V10)	1	1.034749	-1.118432	3.548049
	2	1.036806	-.97305	2.768766
	3	0	5.32	0
	4	1.038884	-.96014	2.61028
	5	1.038884	-.96014	2.61028
5 (H18)	1	.961103	-.362943	1.675396
	2	.983456	-.318988	1.206018
	3	0	3.31	0
	4	.983742	-.323812	1.217774
	5	.983742	-.323812	1.217774
6 (V18)	1	.963611	-.444999	1.809928
	2	.984674	-.384224	1.335467
	3	0	1.79	0
	4	.987022	-.377103	1.281629
	5	.987022	-.377103	1.281629
7 (H21)	1	.976134	-.817486	2.341847
	2	1.000021	-.659168	1.689897
	3	0	1.69	0
	4	.998869	-.647343	1.670606
	5	.998869	-.646343	1.670606
8 (V21)	1	.925322	-.257299	1.383522
	2	.952626	-.221206	1.019098
	3	0	1.59	0
	4	.951387	-.216151	1.016555
	5	.951387	-.216151	1.016555

TABLE A.5b. Values of c_{ijk} for calculating partial derivatives as functions of the scaled brightness temperatures τ_i for the 37 GHz channels for lower rain rates (R3 and R4 $\leq 3D_{0i}$ for $i \geq 9$.).

i	j	$k = 0$	1	2
9 (H37)	1	.693817	-1.136579	2.041051
	2	.751703	-.873894	1.586464
	3	0	1.40	1.493946
	4	.754502	-.854604	1.554872
	5	.754502	-.854604	1.554872
10 (V37)	1	.75324	-1.56048	2.546064
	2	.779937	-1.40527	2.290871
	3	0	1.32	0
	4	.781611	-1.385876	2.260884
	5	.781611	-1.385876	2.260884
11 (D37)	1	.443043	-1.595394	5.113542
	2	.408665	-1.023013	4.183668
	3	0	1.37	0
	4	.404127	-.988116	4.134127
	5	.404127	-.988116	4.134127

TABLE A.5c. Values of c_{ijk} for calculating partial derivatives as functions of the scaled brightness temperatures τ_i for the 37 GHz channels for higher rain rates (R5 and R6 $\geq 3D_{0i}$ for $i \geq 9$)

i	j	$k = 0$	1	2
9 (H37)	1	-4.878802	7.813715	-5.924487
	2	-5.635366	7.258888	-4.685687
	3	-10.70407	15.84933	-6.668128
	4	-5.424598	7.366886	-4.797842
	5	-5.424598	7.366886	-4.797842
10 (V37)	1	-.757597	-.488206	-.175748
	2	-.798662	-.34645	-.144437
	3	-.375242	.046211	-.224719
	4	-.735034	-.36244	-.144885
	5	-.735034	-.36244	-.144885
11 (D37)	1	-76.81805	177.11535	-117.64442
	2	-78.05425	176.12899	-116.42166
	3	59.56443	-143.98972	66.02621
	4	-76.66038	172.59945	-113.34921
	5	-76.66038	172.59945	-113.34921

TABLE A.6. Leading term in relative weight calculation

Channel	wt_{0i}	Channel	wt_{0i}
1 (H6.6)	$\equiv 0$ (arbitrarily)[2]	2 (V6.6)	$\equiv 0$ (arbitrarily)[5]
3 (H10)	0.242	4 (V10)	0.7432
5 (H18)	0.414	6 (V18)	0.5936
7 (H21)	$\equiv 0$ (arbitrarily)	8 (V21)	$\equiv 0$ (arbitrarily)
9 (H37)	0.600	10 (V37)	$\equiv 0$ (arbitrarily)[5]
11 (D37)	0.3517	...	...

A.3 Weights

For the channels having only a single branch, the dominant term in the expression for error is $\partial R_i / \partial T_{Bi}$. Therefore, the weight for channel i ($i = 1,...,8$) may be written as

$$wt_i = \begin{cases} wt_{0i} & \text{for } R_{0i} \leq 0 \\ wt_{0i} \cdot \exp(-2 \cdot R_i / D_{0i}) & \text{for } R_{0i} > 0 \end{cases} \tag{A.3}$$

For channel 9 (*i.e.* H37) the expression found by artful curve fitting is

$$wt_9 = \begin{cases} wt_{09} & R_9 \leq 0 \\ [wt_{09} \cdot \exp(-2R_9 / D_{09})] & R_9 > 0, R_5 \leq 3D_{09} \text{ and } R_6 \leq 3D_{09} \\ [wt_{09} \cdot \exp(-2R_9 / D_{09}) & R_9 > 0, R_5 \geq 3D_{09} \text{ and } R_6 \geq 3D_{09} \\ +0.000175(1 - \exp(1 - 2 \cdot R_9 / 4.16))] \end{cases} \tag{A.4}$$

For channel 11 (*i.e.* D37)

$$wt_{11} = \begin{cases} wt_{011} & \text{for } R_3 \leq 0 \\ \{wt_{011} \cdot \exp(-2R_{11} / D_{011})\} & \text{for } R_3 < 3D_{011} \text{ or } R_4 < 3D_{011} \\ \{wt_{011} \cdot [1 - \exp(-2R_{11} / D_{011})] & \text{for } R_3 \geq 3D_{011} \text{ and } R_4 \geq 3D_{011} \\ +0.00016 \cdot [1 - \exp(-(R_{11} - 7.4157) / 11.802)]\} \end{cases} \tag{A.5}$$

---

[2] Due to the relatively poor spatial resolution of the 6.6 GHz channels and the redundancy of V37 with D37.

The wt_{0i} in (A.3)-(A.5) are listed in Table A.6.

These weights must be regarded as unnormalized. For each channel its own estimate of the rain rate is used to compute the weight. Consequently, they will only add to one if all the rain estimates are equal. Therefore, care must be take in using then to obtain the final estimate to divide by the sum of the weights. Thus,

$$\overline{R} = \left[\frac{\sum\limits_{i=1}^{i=11} wt_i \cdot R_i}{\sum\limits_{i=1}^{i=11} wt_i} \right] \tag{A.6}$$

A.4 Environmental Data

As discussed in Sec. 4, estimates of several environmental variables were used to make adjustments in the algorithm for converting SMMR brightness temperatures to rain rates. Required variables were: sea surface temperature (SST), relative humidity (RH), wind speed, and height of the freezing level (Z_{fr}). The mean monthly fields of the variables that were used are illustrated in four tables beginning on the following page. After these are two additional environmental variables which were *not* used, but which make-up part of a useful dataset for study of rainfall patterns. These are air temperature (T_a) and a representation of the surface wind vector components u and v from the Comprehensive Ocean-Atmosphere Data Set (COADS).[3] Finally divergence grids generated from u and v are given. To facilitate further study all the fields illustrated in this section have been placed in files mirroring the structure of the monthly rain rate files.

Even casual perusal of these figures reveals apparent artifacts, features that resemble patterns of ship tracks. These are especially clear in RH fields, perhaps because they are essentially a small difference between two grids of comparatively large numbers (air temperature and dew point temperature) collected by ships. The appearance of these features is enhanced by our choice of gray scale. Plots of these fields in the form usually presented —contours at ~5 levels— do not readily reveal these features. Similarly, although the u and v fields look relatively smooth, the differentiated forms (*e.g.* $\nabla \cdot \mathbf{v}$) show apparent random blotches and more linear features whose orientations suggest ship track related sampling fluctuations as well as more persistent and obvious documented features.

---

[3] We obtained these from the NASA World Climate Research Program's TOGA CD-ROM, Vol. 1., Jet Propulsion Laboratory, Distributed Active Archive Center, Pasadena CA., 1994.
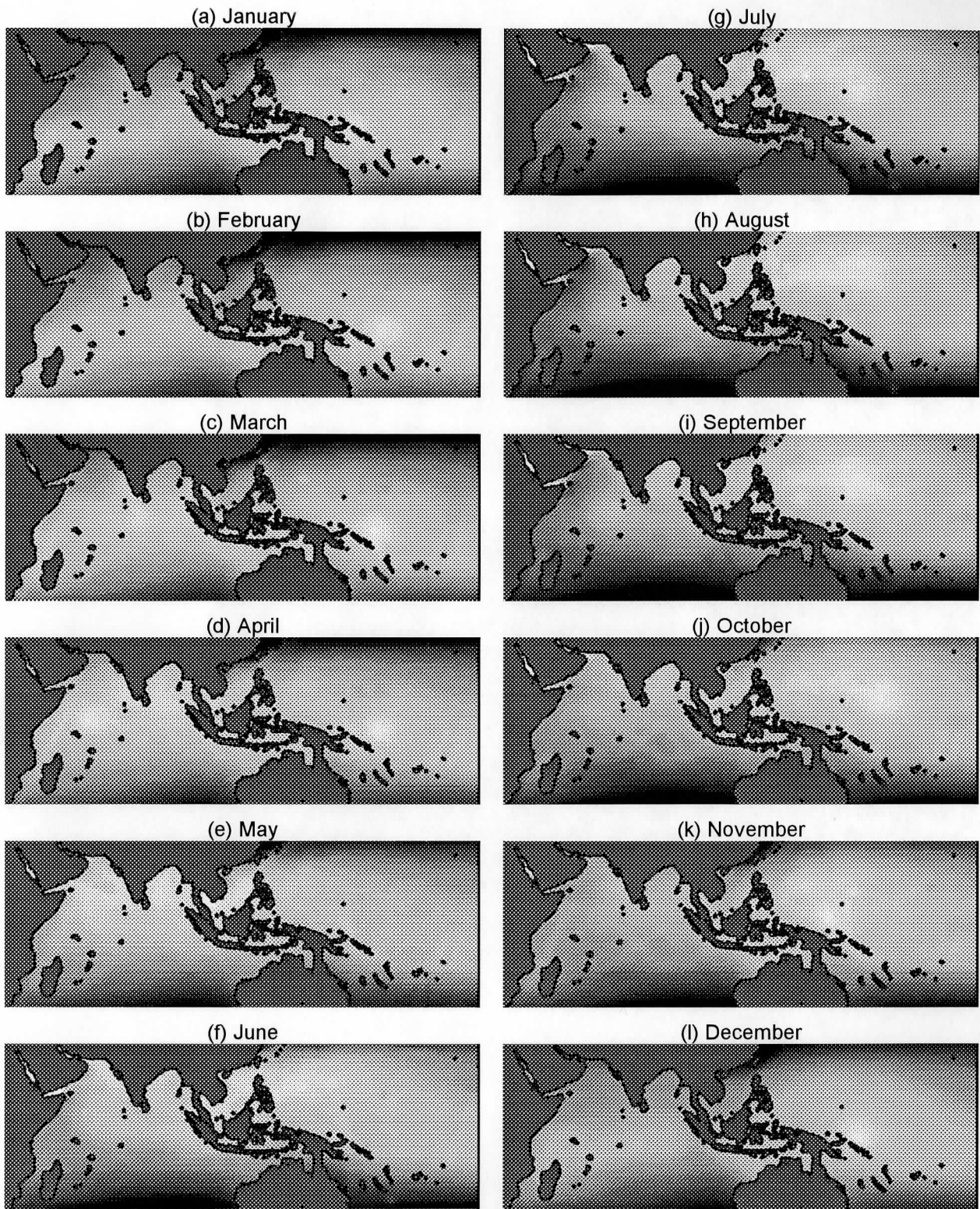
Fig. A.1. Sea surface temperature climatology used with SMMR rain algorithm to obtain rain fields. The gray scale is linear (black to white) over the range 20 to 30 C°. Values below this range are black. Above this range values are white.
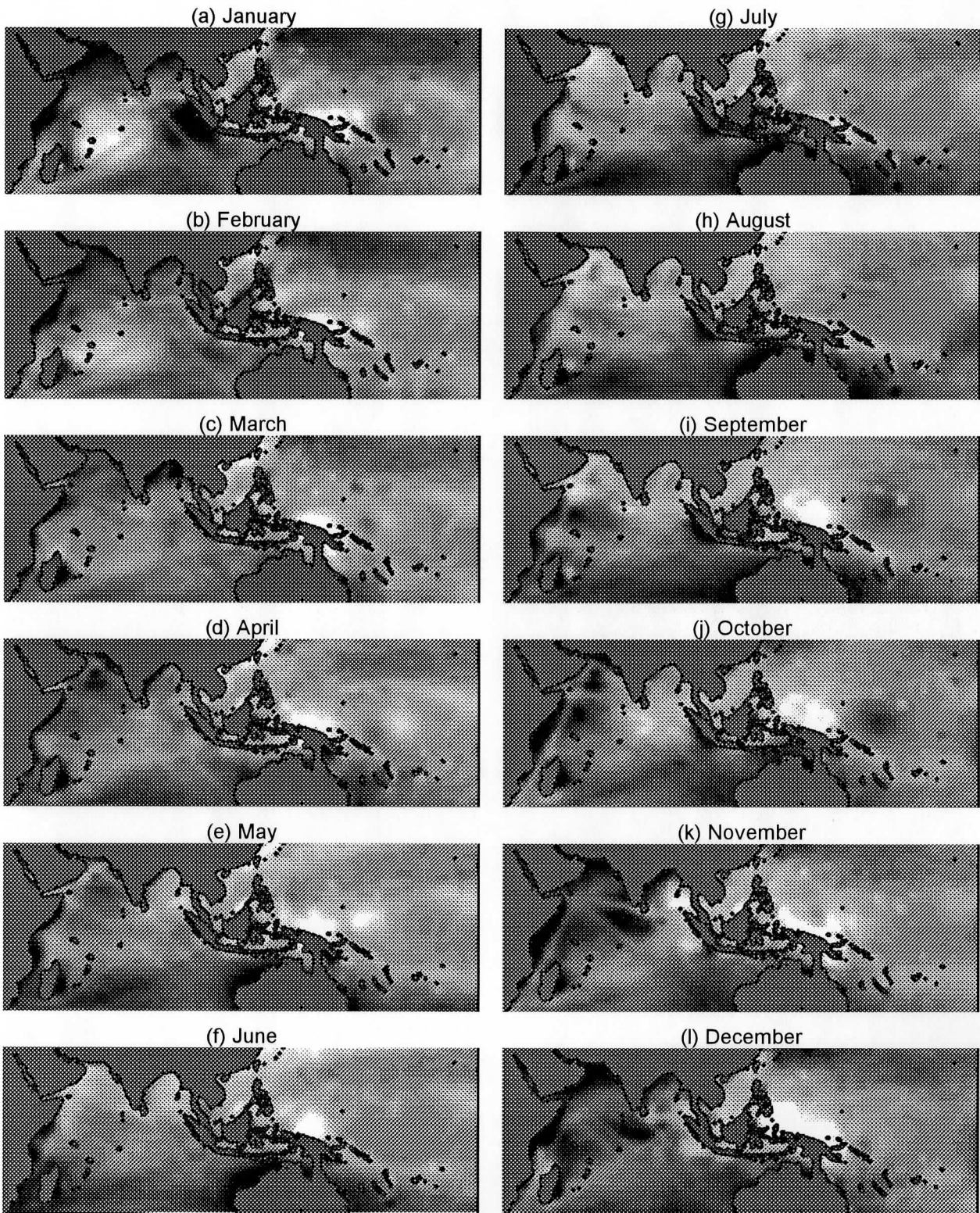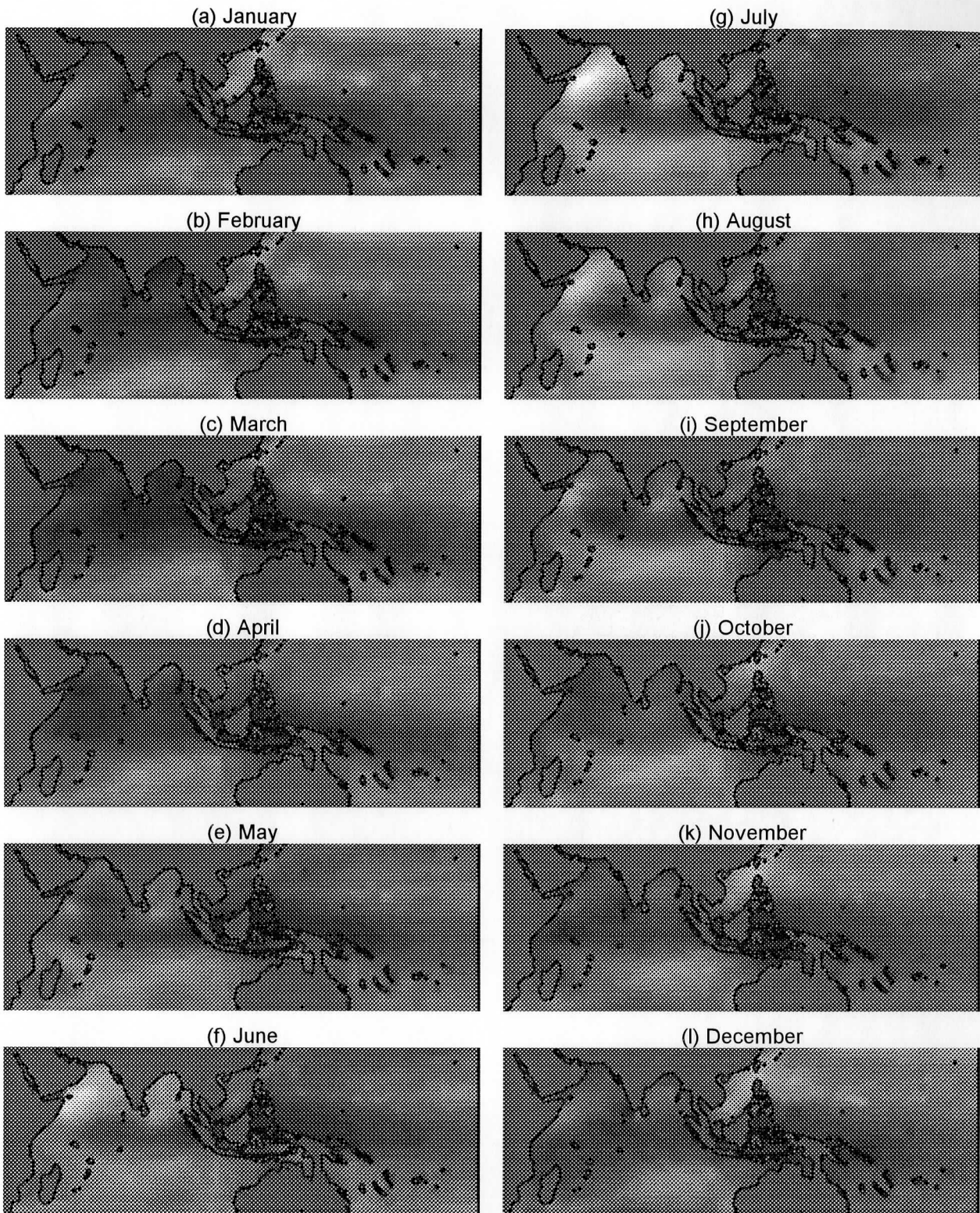
(a) January (g) July

(b) February (h) August

(c) March (i) September

(d) April (j) October

(e) May (k) November

(f) June (l) December

Fig. A.2. Relative humidity climatology used with SMMR rain algorithm to obtain rain fields.
The gray scale is linear in the range 67.5 to 87.5% (black to white). Values less
than 67.5 are black; values greater than 87.5% are white.

Fig. A.3. Surface wind speed climatology used with SMMR rain algorithm to obtain rain fields. The gray scale is linear (black to white) in the speed range 0 to 15 m/s. Speeds greater than 15 are white.
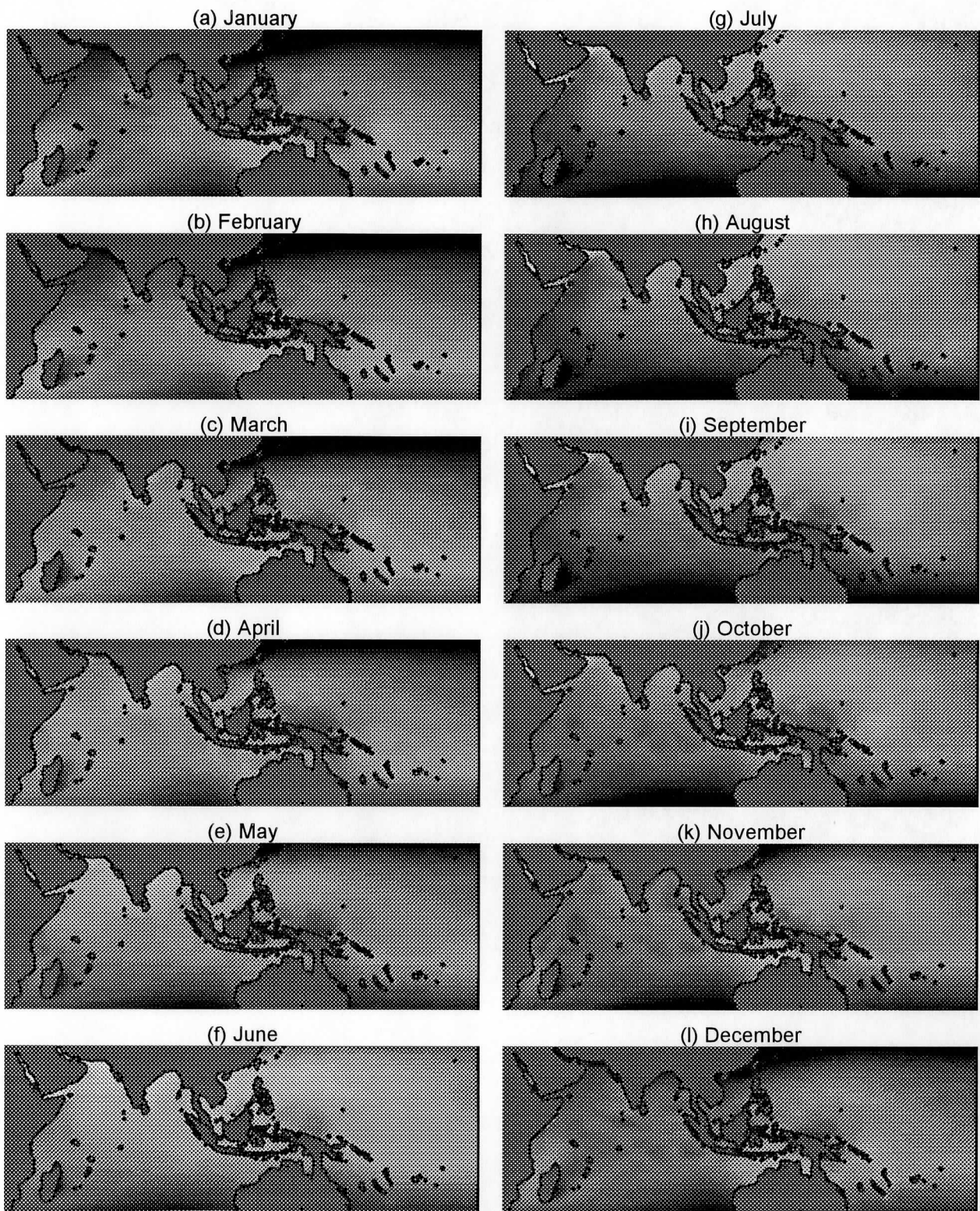
Fig. A.4. Freezing level climatology used with SMMR rain algorithm to obtain rain fields.
Freezing levels less than 3.0 km are black, those greater than 5.5 km are white.
Between 3.0 and 5.5 km the scale has linear gradation from black to white.

A-11

(a) January *u*

(b) January *v*

(c) February *u*

(d) February *v*

(e) March *u*

(f) March *v*

(g) April *u*

(h) April *v*

(i) May *u*

(j) May *v*

(k) June *u*

(l) June *v*
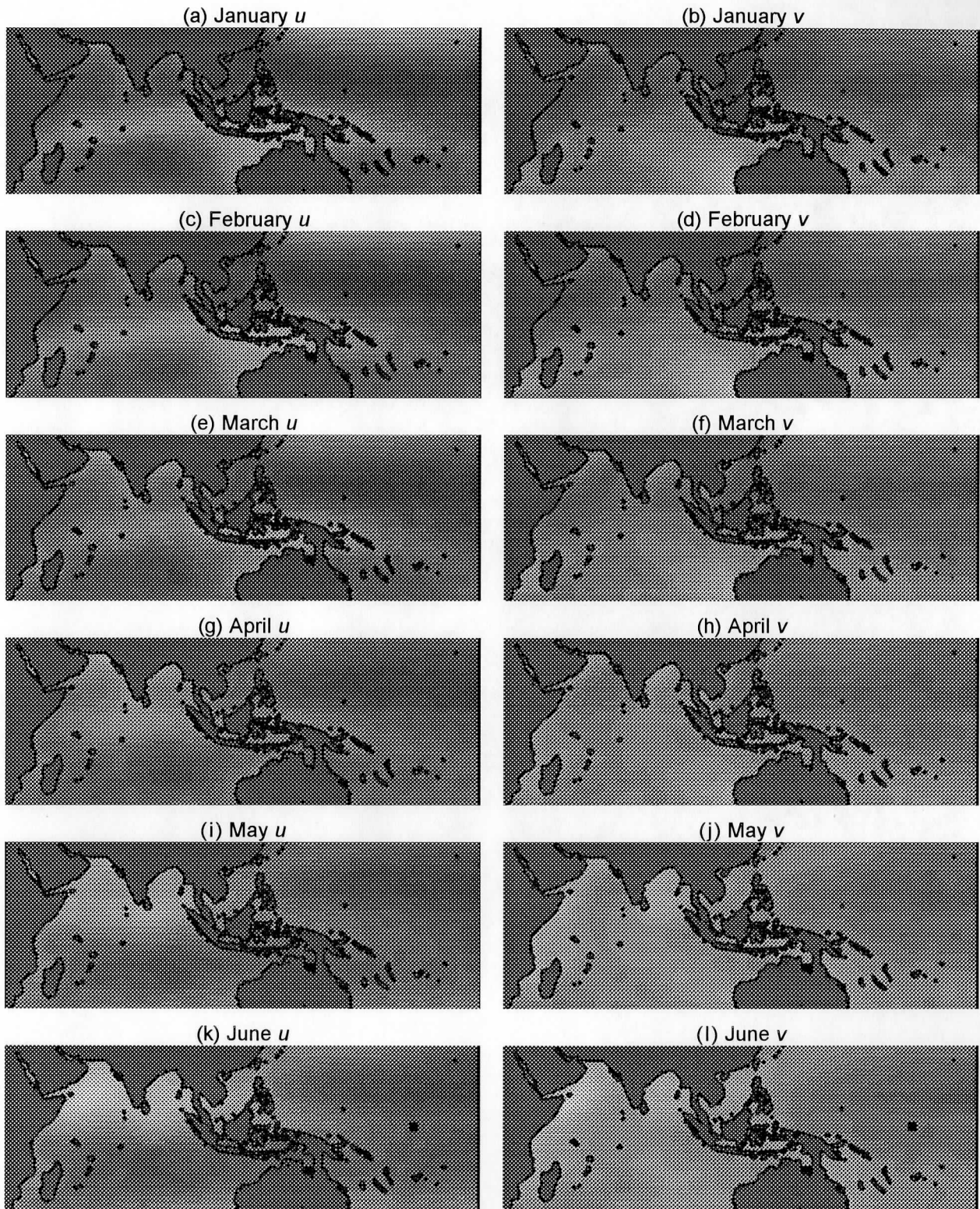
Fig. A.5. Monthly climatological westerly and southerly wind components *u* and *v* from the COADS data set (JPL, 1994) . The COADS data are provided on a 2° by 2°. These have been interpolated to our 1° by 1° grid The gray scale is linear for both components. Black: -15 m/s to white +15 m/s. The figure continues on the following page.

A-12

(m) July *u*   (n) July *v*

(o) August *u*   (p) August *v*

(q) September *u*   (r) September *v*

(s) October *u*   (t) October *v*

(u) November *u*   (v) November *v*

(w) December *u*   (x) December *v*
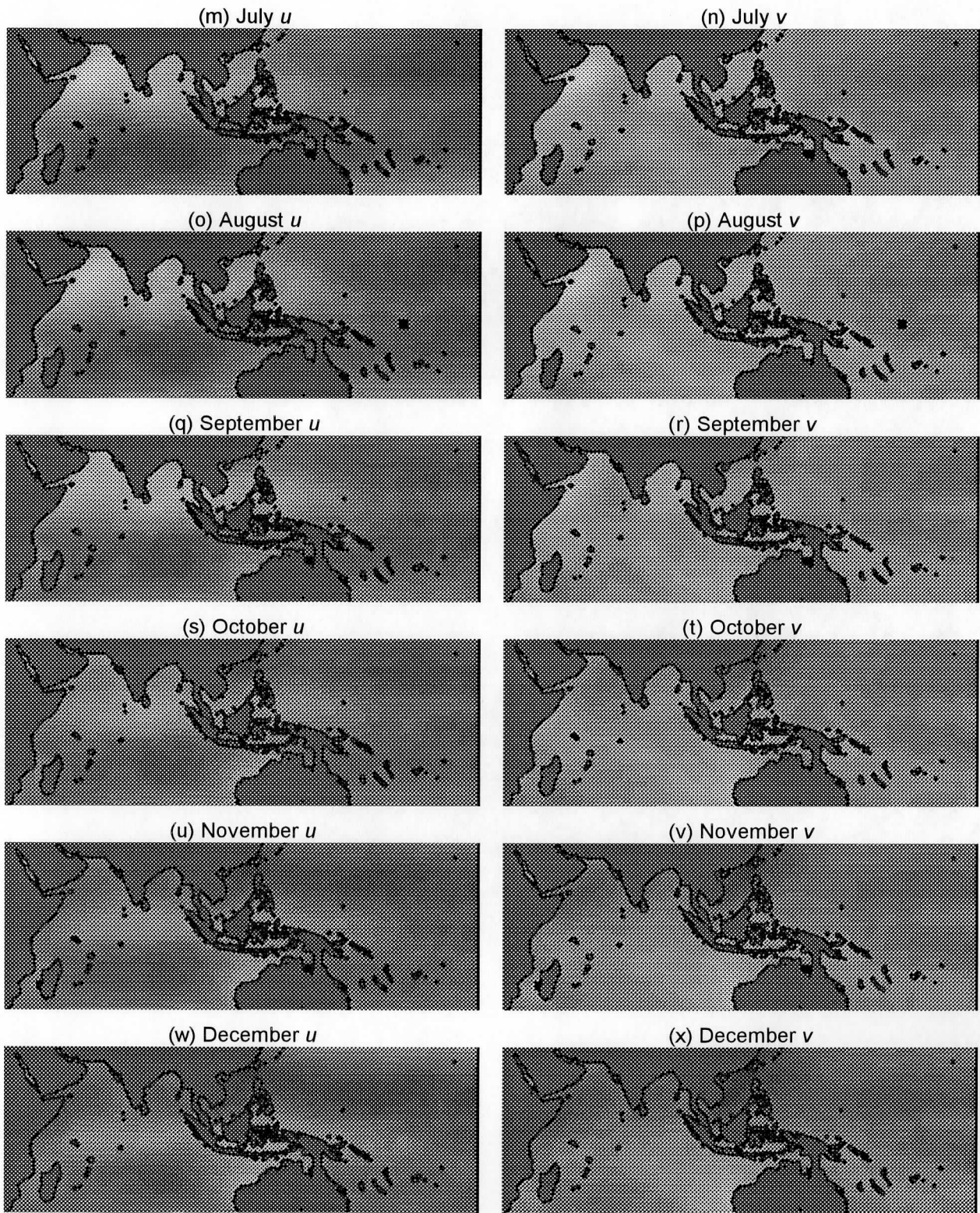
Fig. A.5. (continued) Monthly climatological westerly and southerly wind components *u* and *v*.
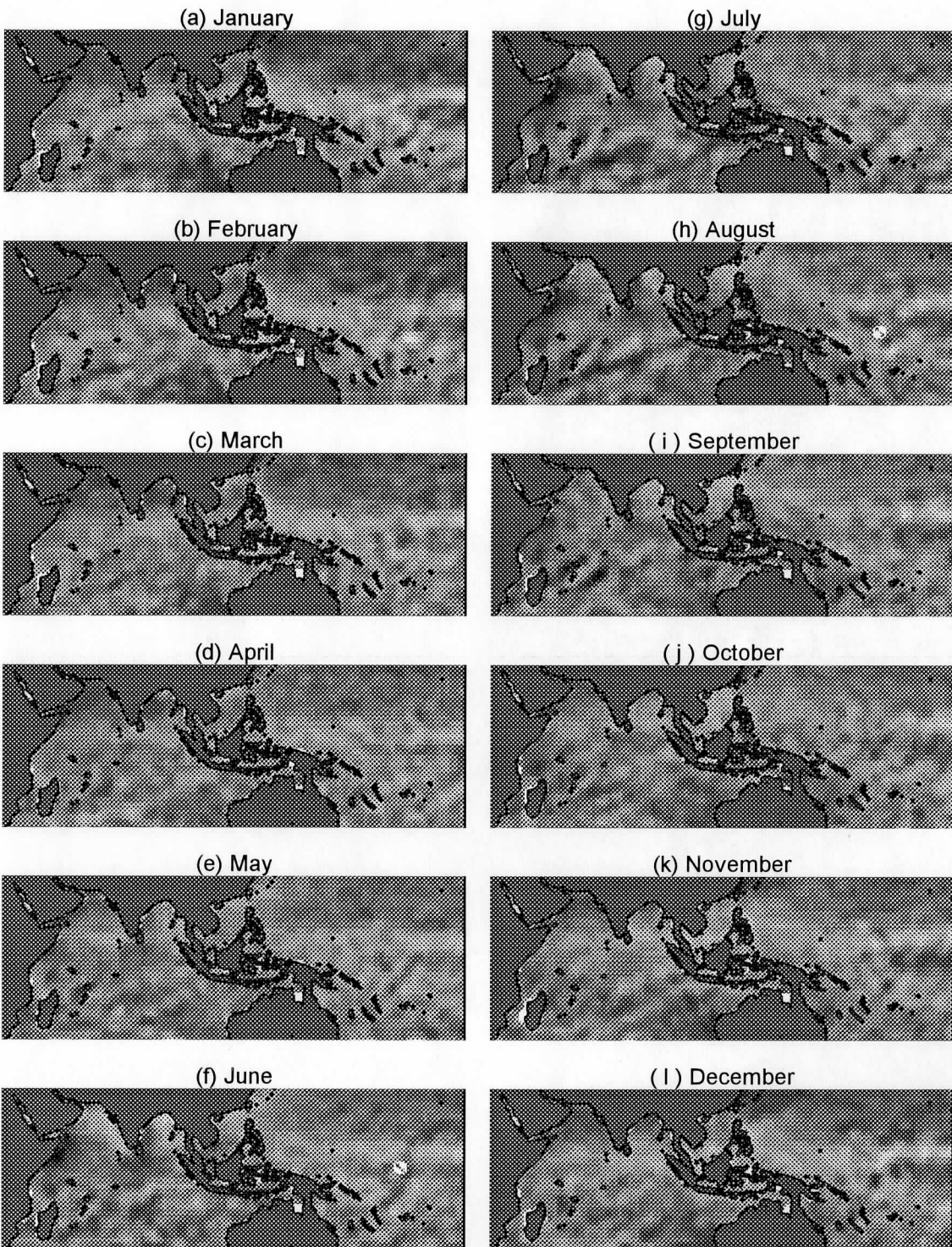
Fig. A.6. Convergence of the COADS monthly climatological wind fields. Note the obvious
artifacts along coastlines due to the coarser resolution of the original gird,
and occasional artifacts due to missing values in an isolated cell.

APPENDIX B
ADDITIONAL INFORMATION ON SEASONALITY

The set of 12 mean monthly rain maps can be expanded at each point as a series in the phase, $\varphi = 2\pi \cdot \text{Month}/12$. Specifically,

$$R = C_0 + \sum_{i=1}^{6} C_i \cos(\varphi - \varphi_i)$$

Since the terms of the sum are orthogonal, the relative "power" in each harmonic is C_i^2. As shown in the panels of the figure below, the power decreases rapidly up to $i = 2$, the semiannual variation. All panels are on a linear gray scale: black = 0 to white = 1. On this same scale, a panel showing $[C_3^2 + \ldots + C_6^2]/[C_0^2 + C_1^2 + \ldots + C_6^2]$ would essentially appear black. That is, the mean annual and semiannual variations account for almost all the power. Several other figures follow which consider the relative importance of the annual and semiannual variations.
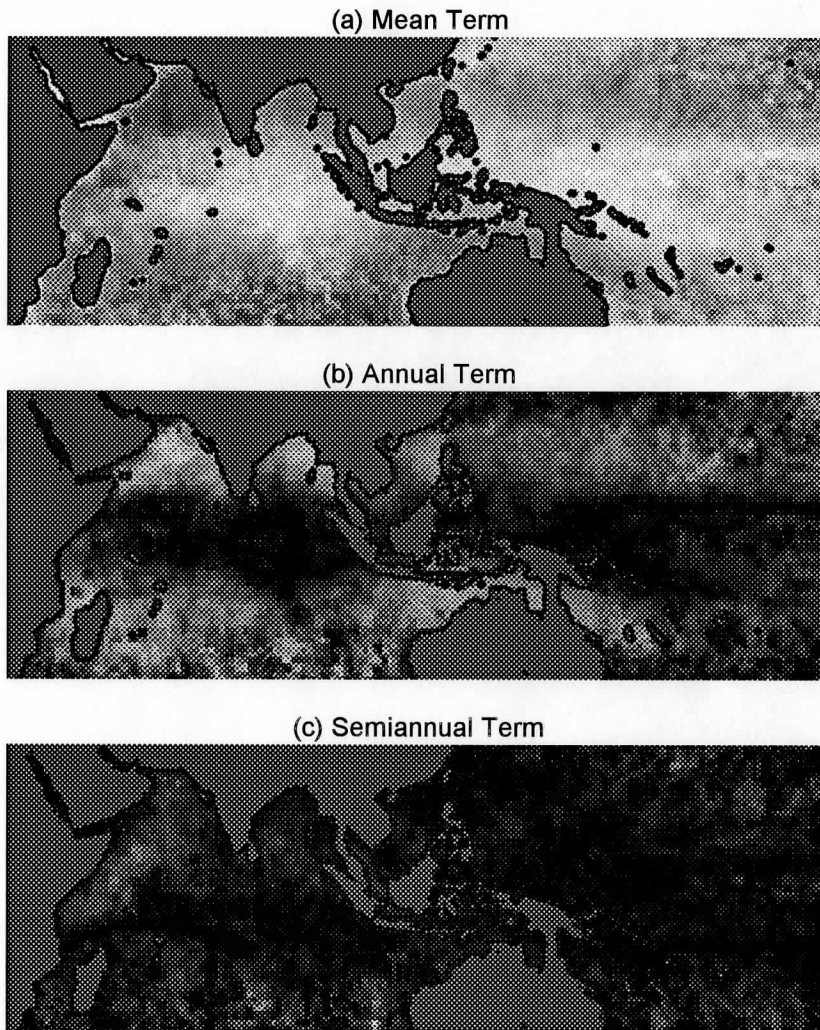
(a) Mean Term

(b) Annual Term

(c) Semiannual Term

Fig. B.1. Fractional power spectrum of rain. Panel (a) shows $C_0^2/[C_0^2+C_1^2+\ldots+C_6^2]$, panel (b) shows $C_1^2/[C_0^2+C_1^2+\ldots+C_6^2]$, and panel (c) shows $C_2^2/[C_0^2+C_1^2+\ldots+C_6^2]$.
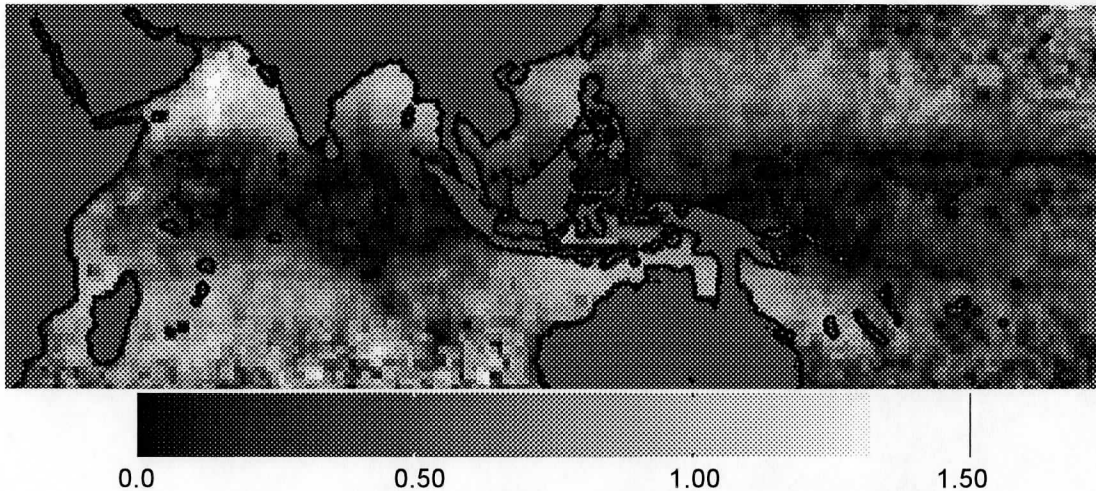
Fig. B.2. Primary seasonality —the ratio of the amplitude of first annual harmonic (C_1) of the rain rate to the annual mean of the rain rate (C_0).
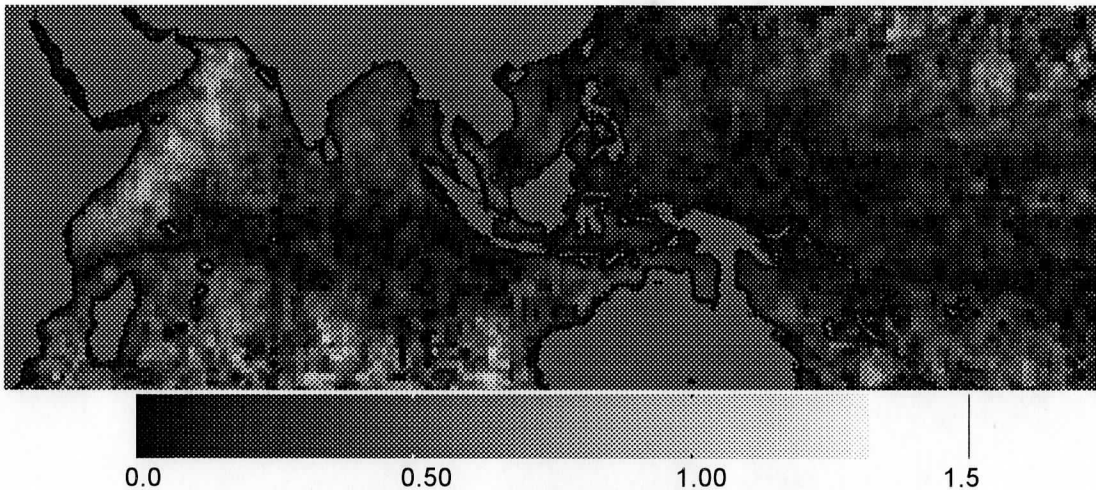

Fig. B.3. Secondary seasonality —the ratio of the amplitude of second annual harmonic (C_2) of the rain rate to the annual mean of the rain rate (C_0).

The three figures below isolate groups of phase vectors from the annual harmonic. They are useful for identifying distinct climatic regimes according to the season the annual component of rain maximizes.

Fig. B.4 allows us to clearly discriminate the *intense* monsoon region extending from the Arabian Sea to the South China Sea. We also see an Australian monsoon from the Coral Sea through the Gulf of Carpentaria and the Timor Sea along the Indonesian archipelago.

Fig. B.5 shows (as expected) that there are few locations with annual rain maximizing in the winter solstice sector of the calendar. Moreover these are likely "accidentals" as they occur where the annual rain component is weak relative to the annual mean. That is, C_1/C_0 as, shown by Fig. B.2, is small.

The last figure in this group, Fig. B.6, shows the regions where annual rain maximizes in the two post equinox months. The latitude structure suggests, as one would expect, that these are related to the passage of the sun overhead.
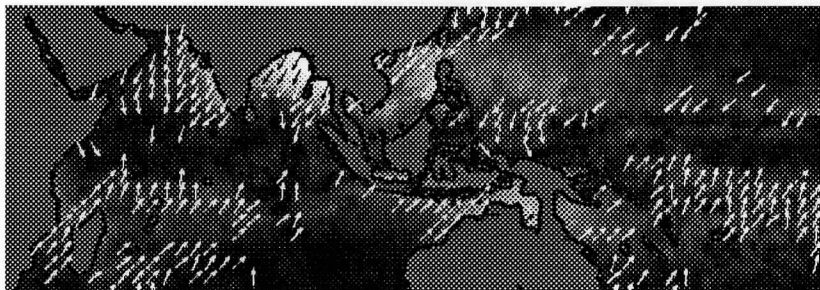

Fig. B.4. Regions with annual harmonic maximum between summer solstice (local to each hemisphere) and solstice plus two months. The amplitude of the annual harmonic is shown in the back-ground. Arrows are shown only for amplitudes greater than 50 mm d^{-1}.
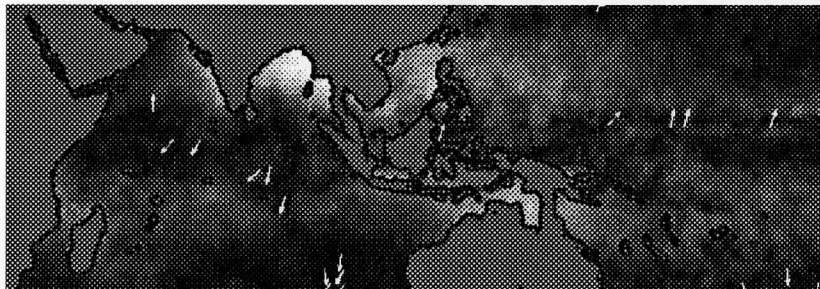

Fig. B.5. Regions with annual harmonic maximum between winter solstice (local to each hemisphere) and solstice plus two months. The amplitude of the annual harmonic is shown in the back-ground. Arrows are shown only for amplitudes greater than 25 mm d^{-1}. At a threshold of 50 mm d^{-1} (as used above for the summer solstice) no arrows would be plotted.
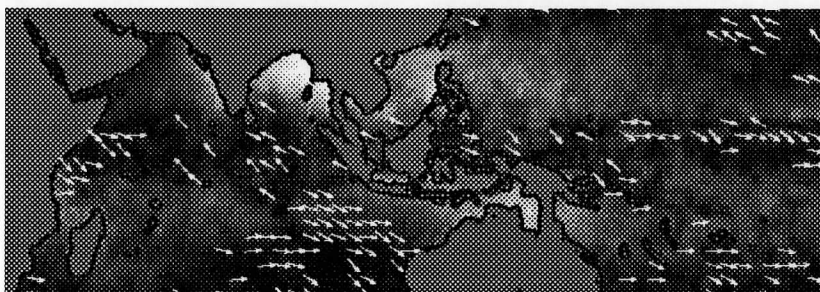

Fig. B.6 Locations whose annual harmonic maximum rain is between either equinox and equinox plus two months. The amplitude of the annual harmonic is shown in the background. Arrows are shown only for amplitudes greater than 25 mm d^{-1}. At a threshold of 50 mm d^{-1} (as used above for the summer solstice) no arrows would be plotted.